

Multivalent Pattern Recognition Through Engineering of Spatial Tolerance in DNA-Based Nanomaterials

Présentée le 30 mai 2022

Faculté des sciences et techniques de l'ingénieur
Laboratoire des biomatériaux programmables
Programme doctoral en science et génie des matériaux

pour l'obtention du grade de Docteur ès Sciences

par

Hale BILA

Acceptée sur proposition du jury

Prof. H. Frauenrath, président du jury
Prof. M. M. C. Bastings, directrice de thèse
Prof. B. Högberg, rapporteur
Prof. P. Dankers, rapporteuse
Prof. F. Stellacci, rapporteur

Acknowledgments

It has been five long years of hard work with a lot of laughter and tears. I am very excited and happy to see the end and I have to acknowledge that it would not be possible without the support I received. Hence, I would like to express my gratitude by sharing happiness with all of them.

First of all, I would like to express my sincere thanks to my thesis director, Prof. Maartje Bastings for giving me the opportunity to pursue my doctoral studies in her laboratory as her first PhD student, and for her motivation, advice that contributed to my studies. I need to thank her specifically for being very supportive during the most difficult times of my life.

I would like to thank my thesis committee members Prof. Holger Frauenrath, Prof. Francesco Stellacci, Prof. Björn Högberg, and Prof. Patricia Dankers for their time to read and correct my thesis.

I would like to give my warmest thanks to doctoral school's secretaries Chrystelle Demierre and Anne Kolly for always being supportive during my PhD and our lovely Eulalia Durussel for her endless administrative support. She was always helpful. We solved many problems with her amazing network.

A special thanks to Artem Kononenko and Vincenzo Caroprese for their contributions to my thesis, and Dr. Marianna Koga for always trying to keep me motivated and stay positive in the last months of my PhD. I would like to thank all members of PBL; Cem Tekin, Hugo Rodriguez, Alice Comberlato, Dr. Jorieke Weiden, Dr. Diana Sobota, Herbert Wong, Christine Lavancy, and also Giacomo Chizzola, Olivia Courbot, and Filippo Ceccon for being a great team. I had wonderful people around me.

My lovely colleagues and special friends Eva Kurisinkal and Kaltrina Paloja always had my back. I am very lucky to have met them during my PBL years. I thank you for scientific and emotional support whenever I need it. You were always there for me, and I know you will always be. You are the sisters from other mothers.

I would like to thank my friends from other EPFL labs, with whom I spent so much time: LMOM old members, Dr. Giuseppe Sforazzini and Augustina Jozeliunaite, SUNMIL old members, Dr. Elif Ertem, Dr. Ahmet Bekdemir and Dr. Özgün Kocabıyık, LCS old members, Dr. Ophélie Planes, Dr. Erica Giraldi, Dr. Mathieu Marmier, and Sébastien Mauries for all the hikes, barbeques, concerts, coffee breaks, grappa fun times.

I also would like to thank my Turkish friends I met in Lausanne, Dr. Cansu İçci, Berkay Köse, Özge Uysal Özdemir, Ömer Özdemir, Dr. Çağır Koçyiğit, and Özgür Yalçın for the amazing snowshoe and hike adventures, dinners, rakı nights and other fun activities.

I am extremely thankful to my dear best friends in my life Ezgi Vidinlioğlu and Öykü Ünal for your unwavering support for the last 11 years. Thank you for always being there for me, for reminding me to take breaks and not to overthink when I am stressed out. We laughed together, we cried together, we traveled together, we cursed to current system in Turkey together. I also would like to thank Alper Ünal for his invaluable friendship. I am looking forward to having more fun with these three amazing people.

I would like to give my special thanks to my whole family for supporting me in the best way they could. My greatest motivation during the last months was my mum, Şehirli Atılğan. Her endless love and support made me who I am today and brought me here. She always wanted to see me as a doctor, but she could not. No words can explain how much I love and miss her. I hope she can feel that her daughter is being a doctor soon, and I dedicate this thesis to my angel, my mum. I would like to thank my dad, Ahmet Atılğan for everything he has done for me and my brother. I am very lucky to have them as my parents and I am very proud to be their daughter. Special thanks to my brother Halil Atılğan and his wife Shaola Abagat Atılğan for always being supportive in the most difficult times. Thanks for everything that helped me to get this day. I also would like to thank my aunt Dilek Ünsal for always backing me up. She is a like a mum to me.

Last but not least, I want to express my gratitude to my lovely husband José Luis Bila. No words can explain how much I love him. He is my motivation, my love, my everything. Thank you for always being there to support me. I feel extremely lucky to be married with such an excellent person. I would not be able to be here without you and I dedicate this thesis to you.

Dedicated to my mum and husband

Abstract

Strength in numbers, combining many weak interactions into an overall strong connection, is the fundamental principle of multivalency. This concept has been exploited for the engineering of super-selective cell-targeting materials, which generally display high number of flexible ligands to enhance the systems' avidity. Many biological processes, however, function through a temporal spatial organization of receptors in patterns, matching with a controlled number of ligands to create a specific interaction. In this low-valency regime, the mechanics e.g. rigidity of the ligand-presenting architecture plays a critical role in the selectivity of the multivalent complex. Exploiting the precision in spatial design inherent to DNA nanotechnology, we engineered a library of scaffolds to explore how valency, affinity, and rigidity control the balance of super-selective multivalent binding. Depending on the affinity between the ligand and receptor, a pattern-dependent binding behavior was achieved when spatial tolerance of ligands matches the spatial organization of the target. We label this new form of mechanics-controlled multivalent binding "multivalent pattern recognition" (MPR). The main parameter controlling MPR is the rigidity of the ligand, which controls the over spatial tolerance of binding. Our findings contribute to the rational design of selective targeting with nanomaterials.

Keywords

Multivalency, pattern recognition, super-selectivity, DNA-based nanomaterials, spatial tolerance

Résumé

La force en nombre, qui consiste à combiner de nombreuses interactions faibles en une connexion globale forte, est le principe fondamental de la multivalence. Ce concept a été exploité pour la conception de matériaux super-sélectifs ciblant les cellules, qui présentent généralement un nombre élevé de ligands flexibles pour améliorer l'avidité des systèmes. Cependant, de nombreux processus biologiques fonctionnent par le biais d'une organisation spatiale temporelle des récepteurs en motifs, qui s'associent à un nombre contrôlé de ligands pour créer une interaction spécifique. Dans ce régime de faible valence, la mécanique, par exemple la rigidité de l'architecture de présentation du ligand, joue un rôle essentiel dans la sélectivité du complexe multivalent. En exploitant la précision de la conception spatiale inhérente à la nanotechnologie de l'ADN, nous avons créé une bibliothèque d'échafaudages pour explorer comment la valence, l'affinité et la rigidité contrôlent l'équilibre de la liaison multivalente super-sélective. En fonction de l'affinité entre le ligand et le récepteur, un comportement de liaison dépendant du motif a été obtenu lorsque la tolérance spatiale des ligands correspond à l'organisation spatiale de la cible. Nous appelons cette nouvelle forme de liaison multivalente contrôlée par la mécanique "reconnaissance de motifs multivalents" (RPM). Le principal paramètre contrôlant la RPM est la rigidité du ligand, qui contrôle la tolérance spatiale de la liaison. Nos résultats contribuent à la conception rationnelle du ciblage sélectif avec des nanomatériaux.

Mots-clés

Multivalence, reconnaissance de motifs, super-sélective, matériaux à base d'ADN, la tolérance spatiale

Contents

Acknowledgments	i
Abstract	i
Résumé	ii
List of Abbreviations	v
Chapter 1.....	Introduction 1
1.1 The Physics of Multivalent Interactions	3
1.2 Thermodynamics of Multivalent Interactions	4
1.2.1 Enthalpy of Multivalent Interactions.....	5
1.2.2 Entropy of Multivalent Interactions	5
1.3 Kinetics of Multivalent Interactions	7
1.4 Design Parameters for Multivalent Materials	8
1.5 Active Selective Targeting	9
1.6 Super-Selective Multivalent Binding	11
1.7 DNA Nanotechnology	13
1.8 Statement of the Thesis.....	14
Chapter 2.....	Design and Characterization of a Multivalent DNA Nanoparticle Library 17
2.1 Design, Self-Assembly, and Characterization of Bivalent Structures.....	17
2.1.1 Modeling of DNA Bivalent Structures	19
2.2 Design, Self-Assembly and Characterization of DNA-Origami Disks.....	21
2.3 Conclusion	24
Chapter 3.....	Multivalent Surface Preparation and Characterization 25
3.1 Streptavidin and Streptactin as Model Receptors.....	25

3.2	Characterization of Protein Coated Surfaces	26
3.2.1	Preparation and Quantification of Adsorbed Protein	27
3.3	Simulations and Calculations of the Surface Distribution	29
3.3.1	Surface Preparation.....	29
3.3.2	Determining Neighbors and Their Distances.....	30
3.4	Conclusion	35
Chapter 4.....	Multivalent Pattern Recognition in DNA Nanomaterials	37
4.1	Streptavidin Binding Peptides	38
4.2	Methods and Materials	40
4.3	Instruments	40
4.4	Buffers	41
4.5	Streptavidin – SLLAHPQ System	41
4.5.1	Peptide Synthesis	41
4.5.2	Synthesis of ssDNA – peptide conjugate.....	43
4.5.3	Self-Assembly of Peptide Functionalized DNA Bivalent Structures.....	45
4.5.4	Binding Studies using Surface Plasmon Resonance	45
4.5.5	Binding Studies using Solid Phase Binding Assay	49
4.5.6	SPR Measurement of SLLAHPQGGGC Functionalized DNA Hexavalent Scaffold	50
4.6	Streptactin – Streptag II System	51
4.6.1	Synthesis of StreptagII (WSHPQFEKGGGC) and DNA - Peptide Conjugate.....	51
4.6.2	Binding Studies using SPR	52
4.6.3	Binding Studies of Streptag II Bivalent Scaffolds by Solid-Phase Binding Assay.....	55
4.6.4	Binding Studies of Streptag II Functionalized DNA Hexavalent Scaffolds using SPR	57
4.6.5	Binding Studies of Streptag II DNA – Origami Disks using Solid Phase Binding Assay.....	59
4.6.6	Conclusion	62
Chapter 5.....	Conclusion and Outlook	65
Chapter 6.....	Appendix	70
Chapter 7.....	References	84
Curriculum Vitae		96

List of Abbreviations

1D	one-dimensional
2D	two-dimensional
3D	three-dimensional
°C	degree Celcius
Å	Ångström
ACE-2	angiotensin-converting enzyme 2
BBB	blood-brain barrier
BSA	bovine serum albumin
calc	calculated
CpG	cytosine-phosphate-guanosine
CTLA-4	cytotoxic T-lymphocyte-associated antigen-4
Cy5	cyanine 5
Da	dalton
DNA	deoxyribonucleic acid
dsDNA	double stranded deoxyribonucleic acid
EDC	ethylene dichloride
e.g	exempla gratia
EGFR	epidermal growth factor receptor
ELISA	enzyme-linked immunosorbent assay
EA	ethanolamine
ESI-MS	electrospray ionization mass spectrometry
<i>et al.</i>	<i>et alia</i>
h	hour
HER-2	human epidermal growth factor 2
L	ligand
<i>m/z</i>	mass:charge ratio
M	molar
min	minute
nm	nanometer
NHS	N-hydroxysuccinimide
Obsd	observed
PAGE	polyacrylamide gel electrophoresis
qPCR	quantitative polymerase chain reaction
R	receptor
RPM	revolutions per minute
RT	room temperature

RU	response unit
s	second
SA	streptavidin
SD	standard deviation
SEM	standard error of mean
ssDNA	single stranded deoxyribonucleic acid
SPR	surface plasmon resonance
ST	streptactin
T	temperature
TLR9	Toll-like receptor 9

Note: additional abbreviation for specific compounds is defined within the text

Chapter 1 Introduction

A key phenomenon found at the fundamentals of life is dynamic interactions that are strong and reversible. While strong and reversible might perhaps seem contradictory, well-known examples both in nature as well as daily life exist. Amongst many others, we here see a botanical example of the burdock and its man-made analog Velcro (Figure 1.1). The multiple hooks on its capsules (called burrs) can attach to the fur of animals or the clothes, as a result, a strong connection can be formed between two surfaces by having multiple of these hooks and loops interactions¹. Additionally, these two surfaces can be easily separated from each other by detaching the hooks and loops (reversibility) because all the individual interactions are very weak. This principle of strength in numbers is called ‘multivalency’ and this concept lays at the basis of strong – yet dynamic - interactions. If one were to translate this information to the molecular level, the hooks can be seen as binding units, ligands (L), and loops as binding pockets, receptors (R). The multiple copies of ligand and receptor molecules come together to form reversible and stronger interactions known as multivalent interactions.

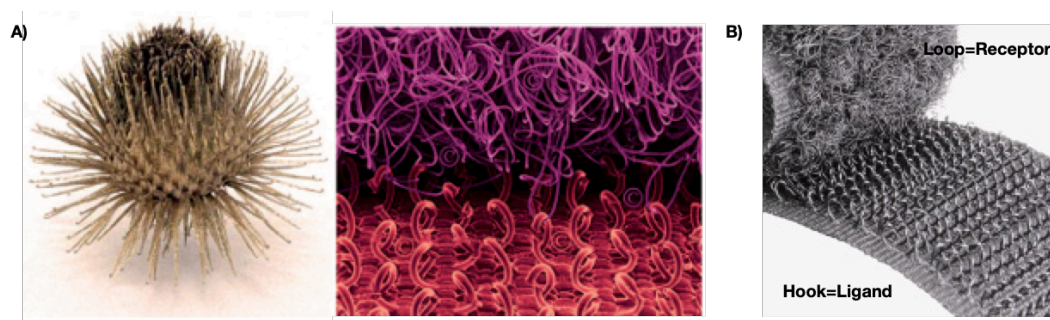


Figure 1.1. A) The burr sparked the idea to mimic the structure as a potential fastener (left) and nature-inspired, hook-loop fastener Velcro (right) Adapted with permission from John Wiley&Sons-Books¹. B) Man-made textile hook-and-loop fastener².

To understand multivalency and its mechanisms, nature often serves as a source of inspiration. Natural multivalent interactions are abundant and are of great interest since they are relevant to many biological phenomena such as the binding of virus particles and bacteria to the surface of cells, signal transduction, immune system recognition, cell-cell interactions among many others.^{3,1,4} For instance, the infection of the influenza virus starts with the attachment of the virus to the surface of the epithelial cell by the interaction between multiple trimers of the hemagglutinin and multiple moieties of sialic acid⁵. The SARS-CoV-2 uses spike proteins on its surface for binding to host cells by fitting to the shape of the receptor, ACE-2 proteins, on epithelial cell surfaces⁶. To inhibit the infection of viruses, antibodies which are the key proteins for the immune system have been used⁵ (Figure 1.2). Antibodies are large Y-shaped proteins, presenting multiple equivalents of binding sites: two (IgG, IgE, IgD), four (IgA), and ten (IgM). Each antibody recognizes a unique molecule of the pathogen, called an antigen and their interactions with antigens are based on multivalent interactions.

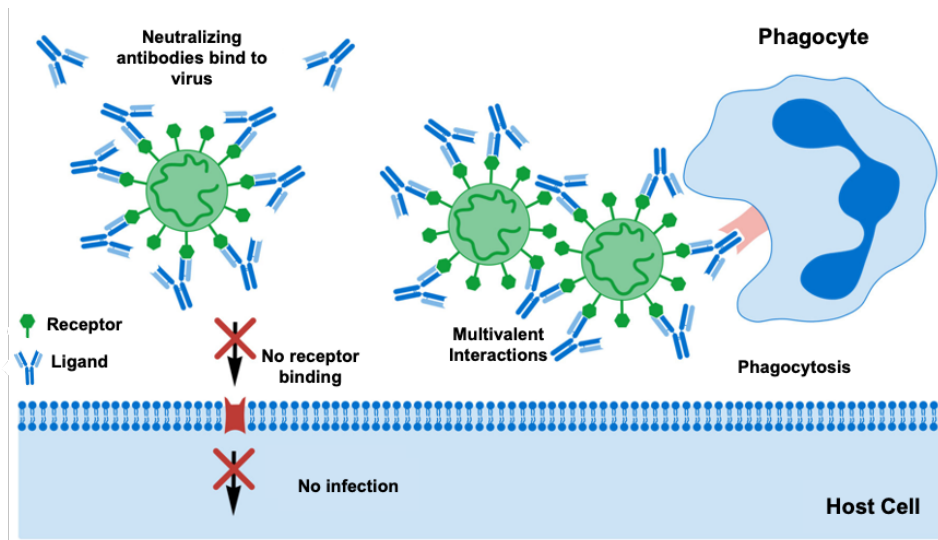


Figure 1.2. Antibodies bind to spike proteins on the surface of SARS-CoV-2 and prevent the virus to enter the host cell. Each antibody can bind to two spike proteins. Adapted with permission from Fluidic Analytics⁷.

Cells in their native environment are surrounded by different types of chemical and physical factors with different length scales ranging from nanometers to hundreds of microns, for example soluble proteins and extracellular matrix fibers. Ligands presented from this native environment in different geometrical arrangements with different spatial organizations and valences affect how a cell responds. For instance, integrin receptors are activated by binding of RGD and PHSRN sequences of fibronectin protein to its extracellular binding domains, and these two peptide sequences are separated by approximately 35 Å⁸. Toll-like receptors 9 (TLR9) present in immune cells recognize DNA containing unmethylated cytosine-phosphate-guanosine (CpG) motifs derived from bacteria and viruses and activate the immune system to remove them from the body⁹. From the crystal structure, the inter-ligand distance of two CpG motifs bound in the active form of TLR9 is 7 nm¹⁰, and using the exact spacing in ligand presenting nanomaterials has been proven to augment immune activation¹¹. Antibody-mediated homodimer of cytotoxic T-lymphocyte-associated antigen 4 (CTLA-4) blockade has been developed to inhibit T-cell signaling to increase the immune response against tumors¹² and these two costimulatory CTLA-4 receptors are separated by a 103 Å distance¹³.

In addition to the spatial arrangement of biomolecules, the number of independent binding sites on a molecule, a phenomenon known as valency plays an important role in cell responses¹⁴. For example, valency regulates the immune sensing and signaling, such as assembly of an immune signaling complex called the myddosome⁹. Certain cytokines, including IL-12 and IL-23, have a valency of more than one, which helps them to recruit co-receptors for signaling¹⁵. Additionally, antibodies produced by immune system in response to infection can switch between 1, 2, and 5 for IgG, IgA and IgM respectively¹⁶. These interactions are important for cells to communicate with other cells and respond to changes in their environment for survival. They rely on a controlled spatial organization and programmable design to be functional where the true advantage of multivalent interactions arises when valency and spacing of ligand and receptors are perfectly matched.

1.1 The Physics of Multivalent Interactions

Multivalent interactions consist of the association of molecules through simultaneous and multiple noncovalent interactions. First, a multivalent architecture is brought from the bulk solution to the proximity of the target. This step is highly dependent on the concentration of both molecules, ligand (L) and receptor (R), as well as the density of the receptor on the target surface. Following the first binding, the second ligand of a multivalent structure is spatially constrained and in close proximity to its target, which leads to an increase of the local concentration and avidity. The spatial proximity of the ligand to its receptor is very important since it determines the probability of the binding process. While the first binding process can be seen as an intermolecular interaction, with a binding affinity constant K_a often smaller than K_{mono} , the second and all the subsequent binding events are considered as an intramolecular process and they are faster because of the higher local concentration of the ligands and increased binding avidity¹⁷. In the case of dissociation of one ligand of the multivalent construct, which is governed the dissociation rate, k_{off} , the ligand still maintains the high local concentration and the probability of rebinding to the same or another target receptor in the proximity of the multivalent molecule will be very high. Therefore, the residence time of multivalent structures is generally high¹⁸.

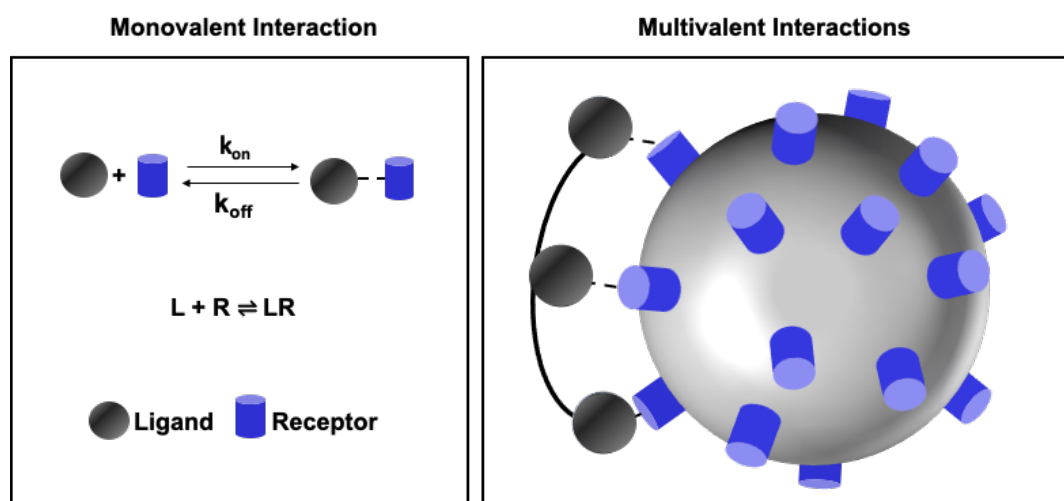


Figure 1.3. Comparison between monovalent vs multivalent interactions. Interaction between a monovalent ligand (L) and a receptor (R) is weak and ligand dissociates from the receptor very fast (left). However, interactions between L and R can be enhanced by having multiple copies of these species (right)

The strength of this molecular interaction between L and R is referred to as the affinity and it is quantified as the equilibrium constant, K_a , for the forward reaction $L + R \rightleftharpoons LR$ (Figure 1.3). More often, the equilibrium constant for the reverse reaction, the dissociation equilibrium constant K_d is used to describe the strength of binding¹⁸. The association rate constant, k_{on} , characterizes how quickly the ligand binds to its target and has units of $M^{-1}min^{-1}$, whereas the dissociation rate constant, k_{off} , characterizes how quickly the ligand dissociates from its target and has units of min^{-1} . The association and dissociation rates depend on the type of interaction and may span several orders of magnitude. k_{on} ranges from $10^9 M^{-1}min^{-1}$ for the fastest association such as an electrostatically assisted association of proteins¹⁹ to $10^4 M^{-1}min^{-1}$ for slow reactions that are often governed by large conformational changes of disordered proteins²⁰. k_{off} depends on how fast the intermolecular interactions stabilizing the LR complex are broken and typically ranges between

10^4 min^{-1} and 10^{-4} min^{-1} ¹⁸. Similar to rate constants the equilibrium constant, K_d may change over several orders of magnitudes from mM- μ M for low-affinity interactions such as protein-carbohydrate interactions to nM-fM for high-affinity interactions such as binding of metal ions¹⁸. By definition the forward and reverse rates of a reaction at equilibrium are equal and can be defined as the following:

$$\text{rate of binding} = k_{\text{on}} [L][R] = k_{\text{off}} [LR] = \text{rate of dissociation.} \quad \text{Equation 1.1}$$

By definition, equilibrium constant, K_{eq} is equal the ratio of forward and reverse rate constants or the ratio of the concentration of LR complex to the concentration of free reactants, L and R, at equilibrium. It has the units of M^{-1} and it is proportional to the affinity. The larger the K_{eq} , the stronger the interaction and the more completely the reactants, L and R, are converted to the product LR²¹.

$$K_{\text{eq}} = \frac{k_{\text{on}}}{k_{\text{off}}} = \frac{[LR]_{\text{eq}}}{[L]_{\text{eq}}[R]_{\text{eq}}} \quad \text{Equation 1.2}$$

The reciprocal of this expression describes the dissociation equilibrium constant, K_d and has units of M. The lower the K_d , the stronger the interaction.

$$K_d = \frac{1}{K_a} = \frac{k_{\text{off}}}{k_{\text{on}}} = \frac{[L][R]}{[LR]} \quad \text{Equation 1.3}$$

1.2 Thermodynamics of Multivalent Interactions

The affinity of a ligand to its target can be determined by the free energy of binding. The enthalpic and entropic components of free energy can be measured experimentally and can provide useful information for the multivalent interactions. While the enthalpy term is dominated by the nature and number of the interaction, the entropy term is influenced by geometry, as explained in the next sections. The relationship between these parameters is given by:

$$\Delta G = \Delta H - T\Delta S \quad \text{Equation 1.4}$$

where ΔG is the change in Gibbs free energy, ΔH is the change in enthalpy, T is the temperature, and ΔS is the change in entropy. A reaction is favorable if the process' Gibbs free energy is negative, $\Delta G < 0$. The binding affinity can be expressed in terms of the change in Gibbs free energy or in terms of equilibrium constant, K_{eq} :

$$\Delta G = -RT \times \ln K_{\text{eq}} \quad \text{Equation 1.5}$$

The above equations demonstrate that the binding affinity can be improved by decreasing the binding free energy which could be achieved by decreasing enthalpy and increasing entropy²².

1.2.1 Enthalpy of Multivalent Interactions

The enthalpy of a multivalent reaction is proportional to the enthalpy of a monovalent analog and the number of binding events, n :

$$\Delta H_{\text{multi}} = n \Delta H_{\text{mono}} \quad \text{Equation 1.6}$$

In some cases, the binding of one molecule to its target with a given enthalpy yields the second ligand to bind with a greater enthalpy, which will cause ΔH_{multi} to be more negative than ΔH_{mono} (more favorable). This process is defined as enthalpically enhanced binding, or cooperative binding⁵. For example, the binding of the first oxygen to hemoglobin enhances enthalpically the next oxygen binding. On the other side, some processes are enthalpically diminished. In the case of a bivalent structure shown in Figure 1.4, the enthalpy of bivalent interaction is double the amount of monovalent interaction. However, the enthalpy is influenced depending on how the ligands are connected. First of all, if the linker or spatial tolerance of ligands is matching directly the distance between the two receptors (case A), there will be no enthalpic contribution to present the ligands from the linker. However, if the linker is too long than the distance of the two receptors (case B), there will be a conformational enthalpic penalty for the second binding. In this case, a flexible linker would be more beneficial than a rigid one because a rigid linker would pay a larger conformational enthalpic penalty due to spatial mismatches, which will result in diminished enthalpy. If the linker is shorter than the ideal length (case C1), for the second binding to occur, the receptor has to change its orientation. This process will need extra energy and in return reduce the observed enthalpy for the second binding. On the other hand, in this case, the receptor will unlikely change its orientation and will not accept the second ligand from the same bivalent structure and will bind to the second dimeric ligand intermolecularly, hence, there will be no enthalpic penalty (C2)¹⁷.

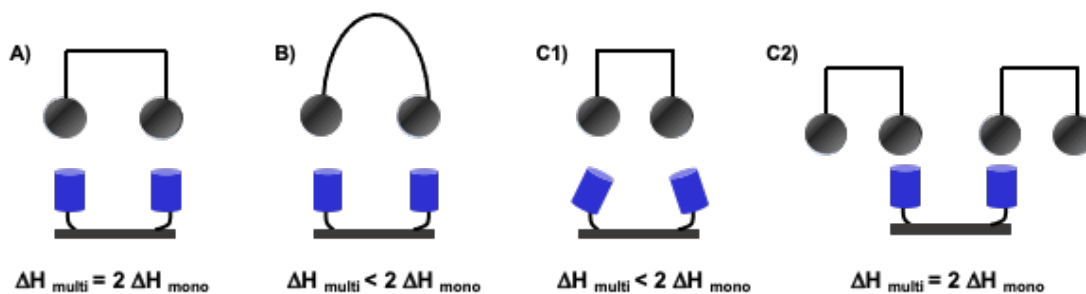


Figure 1.4. Bivalent interactions between ligand and receptor with different linker lengths, A) when linker is the ideal linker, B) when linker is too long, C) when the linker is short, C1) bivalent structure binds intramolecularly, if the receptors change their orientations, C2) receptor will accept only one ligand from bivalent structure, and second binding site will interact with a second bivalent structure intermolecularly.

1.2.2 Entropy of Multivalent Interactions

Understanding the entropy of multivalent interactions is essential to design multivalent architectures for enhanced targeting. The entropy of a multivalent system is the sum of translational and rotational entropies of the ligand, and conformational entropy due to flexibility of the linker, and a contribution from the changes in the entropy of surrounding water molecules due to entropy of hydrophobic interactions⁵.

$$\Delta S^{\text{multi}} = \Delta S_{\text{trans}} + \Delta S_{\text{rot}} + \Delta S_{\text{conf}} + \Delta S_{\text{water}} \quad \text{Equation 1.7}$$

A multivalent ligand is assumed to have the same rotational and translational entropy compared to its monovalent analog but larger conformational entropy due to its connecting linker⁵. Therefore, one can assume that multivalent binding is governed by the conformational entropy²³. When a ligand is tethered to a scaffold with a certain degree of conformational freedom, the Gibbs free energy released upon binding ($\Delta G_{\text{tethered}}$) to its target receptor is smaller than the free energy of the same group when they are in solution ($\Delta G_{\text{solution}}$). This difference is due to entropic cost emerged from the reduced conformational space²⁴:

$$\Delta G_{\text{tethered}} = \Delta G_{\text{solution}} - T\Delta S_{\text{conf}} \quad \text{Equation 1.8}$$

This conformational entropic cost depends on the length and flexibility of the linker, and their positions on the surfaces. For instance, for a bivalent system (Figure 1.5), when the linker is suitable in size and rigid, matching the distance of the two receptors, an intramolecular binding will occur (the second ligand will bind to the second receptor) with a greater change in free energy compared to first binding and the change in entropy for intramolecular binding will be zero (case A). However, when the linker is unsuitable in size and too flexible, the conformational entropic penalty would be very high (case B). If the conformational entropic penalty is greater than the entropic penalty of the monomeric binding, the bivalent structure would prefer to bind intermolecularly since intramolecular interaction is not entropically enhanced⁵.

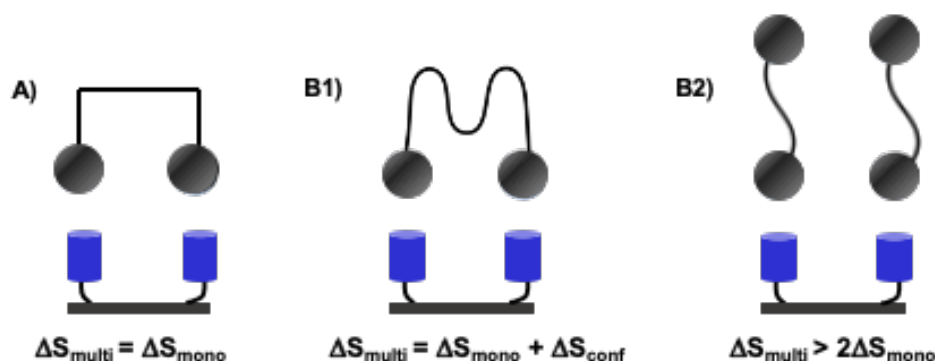


Figure 1.5. Change in entropy in multivalent interactions. A) when the linker is rigid and matches the receptor distance, B) when the linker is too long and flexible B1) bivalent structure binds intramolecularly with a high conformational entropic penalty, B2) bivalent structure prefers to form second intermolecular interaction as the intramolecular interaction would no longer be enhanced.

There is still an ongoing controversy in the literature about the extent to which conformational entropy loss of the flexible scaffold of multivalent structure affects the enhancement of binding. Temperature-dependent dimerization of DNA tile nanostructures was assessed to evaluate the role of entropy and enthalpy and investigate the effect of scaffold flexibility on the binding of a multivalent molecule²⁵. As expected, rigid DNA scaffolds have the lowest conformational entropy and highest thermal stability compared to flexible analogues. On the other hand, flexible designs have more favorable enthalpic gain that can partly compensate for the high conformational entropic penalty. In another study, the interaction between rigid and flexible cores of trivalent sialosides having oligoethylene glycol (OEG) spacers and spike proteins of influenza A virus was studied²⁶. Experimental and simulation studies showed that rigid core trivalent structure was the most potent inhibitor against the virus, whereas no binding was observed with the flexible core due to increased conformational entropy. However, rigid scaffolds cannot always be the best choice to enhance the multivalent binding if the geometry and distance between the binding units do not match. Aptamer functionalized DNA

nanostructures have been used to engineer multivalent binding cavities by controlling the orientation and flexibility of attachment parts for a target protein²⁷. It was shown that rigid linkers are the best choice when the distance between the binding units match and the scaffold does not need to stretch or bend to fit the binding site of the protein. On the other hand, if the geometry of the binding site does not match the optimal binding distances, flexible linkers are a better choice since they can stretch whereas rigid ones cannot, hence, cannot facilitate binding.

The final contribution to total entropy in multivalent interactions is the change in entropy of the surrounding water molecules, ΔS_{water} , which comes from the effect of the linker. The linker may affect the water molecules around the ligand during or after the association of ligand and receptor on a multivalent system. The water molecule around the ligand may be replaced by receptor binding site upon interaction. In addition, water molecules around the linker may be displaced by the receptor binding site, which is not the case for a monovalent interaction¹⁷.

As it is seen from a thermodynamic point of view, there are enthalpic and entropic contributions to the Gibbs free energy for multivalent interactions. Different factors should be taken into consideration to study the binding, and the nature of the linker or material that connects multiple ligands play an essential role. This platforms needs to be designed carefully with respect to receptor molecules in terms of geometry and flexibility. From a thermodynamic view, ligands presentation with a spatial arrangement and conformationally rigid structures might be preferred when designing a multivalent architecture in order to minimize the conformational entropic penalty. However, some degree of freedom can be also included to maximize the ligand fitting to receptor binding sites.

1.3 Kinetics of Multivalent Interactions

Compared to equilibrium experiments, kinetic experiments provide more information about binding reactions. In fact, they describe the rate and extent to which a complex can be produced relative to its reactants, and the extent of multivalent complex formation, LR, of a ligand binding to a receptor as in equation 1.2. After the first binding of a multivalent ligand, the second ligand is spatially in closed proximity to its receptor, which increases the local concentration and probability of rebinding event, therefore the the second and all subsequent bindings will proceed faster²⁸. On the other hand, the dissociation rate of a multivalent binding is slower compared to monovalent binding, and it depends on the bound ligand concentration²³. Generally, the dissociation rate constant is the main determinant of the affinity. For instance, for a low-affinity reaction, e.g., K_d of 1 μM , the dissociation rate constant will be on the order of 1 s^{-1} , whereas for a high-affinity reaction, e.g., K_d of 1 nM, the dissociation rate constant will be on the order of 0.001 s^{-1} ²¹.

Several factors should be considered to have an efficient multivalent binding. Such factors include nature of the linker, the spatial proximity of the ligands, the concentration of the ligand, affinity of monovalent interactions, the distance of the binding units, which affect the free energy, enthalpy, and entropy of the system at the end. In the next section, the factors to consider when designing a multivalent ligand-targeted therapeutic system will be discussed.

1.4 Design Parameters for Multivalent Materials

Nanoparticles decorated with targeting ligands to advocate selective delivery of therapeutics towards specific cell populations have been extensively studied. Multivalency in nanomedicine can be achieved by attaching multiple copies of ligands on the scaffolds in different architectures such as polymers, liposomes, dendrimers, etc. Parameters such as size, shape, charge, valency, density of ligands, linker flexibility and length are great of interest in the design of multivalent particles for enhanced targeting (Figure 1.6).

Size: is one of the most important parameters for the selection and binding of nanoparticles. The small size of the particle is ideal for drug delivery purposes due to ease of penetration and diffusion through tissue and they can accumulate in tumor tissues²⁹. However, it should be optimized to match the size of its target to maximize the binding. For instance, transferrin-coated gold nanoparticles with different sizes were synthesized to study the effect of nanoparticle size on tumor targeting³⁰ and it was found that 60 nm diameter range particles showed 5 times faster tumor accumulation, and no significant differences was observed between 15, 10, 100 nm diameter sized particles.

Shape: is another important parameter affecting particles' performance, e.g. its binding ability by changing the way in which ligands are presented on the particle surface and are accessible toward the target receptors. Studies have shown that endothelial targeting in the vasculature by using polymer-carriers can be modulated by particle geometry/shape. Disks had longer half-lives in circulation due to alignment of these particles with the flow and higher targeting specificity, whereas sphere particles accumulate nonspecifically in the vasculature likely due to mechanical entrapment of these particles in small capillaries³¹.

Surface Properties / Charge: The fate of nanoparticles inside the body can be determined by their interactions with the surroundings, which depend on their surface properties. For instance, nanoparticles sterically stabilized by polyethylene glycol (PEG) moieties are less prone to self-self interactions³². Moreover, there are many charged molecules inside the cell environment, which would repel negatively charged particles. Hence, one has to minimize the nonspecific interactions via steric stabilization and control the surface charge to prevent nanoparticle accumulation in off-target cell types.

Valency: In general, as the valency of the ligand increases, the binding avidity increases. However, the valency should be optimized, considering the distance and orientation between the binding sites of the target molecule. For instance, tumor-targeting multivalent antibodies generally have two or three valencies³³. Bispecific antibodies in particular, are considered attractive therapeutic agents due to their ability to target two distinct disease mediators, which increases its selective targeting³⁴.

Density of the ligand: The ligand density can be defined as the number of ligands relative to the number of side chains or functional groups on the scaffold of the structure. The high density of ligands can induce the probability of rebinding of dissociated ligands to their target receptors. However, there is also a limit of 'optimal density'. Studies have shown that the cellular binding of rod-shaped nanoparticles depends on the ligand density. As the ligand density increased, the fraction of bound particles to cell membrane increased only up to a point when ligand density increased, after which a decrease in binding was observed³⁵.

Linker flexibility: The major overcome for ligand-receptor binding is the entropic changes which will be covered in the next section in detail. When a multivalent ligand approaches a receptor, initially first binding occurs which later initiates the second ligand to bind to a closed proximity receptor. The better the ligand–ligand distance matches the distance of receptor sites at given scaffold flexibility of the multivalent structure, the stronger the binding enhancement. However, a conformational entropy penalty has to be paid when a flexible scaffold is used due to its arrangement to find the second receptor. Therefore, a rigid scaffold generally provides a higher binding enhancement by ensuring the ligands are oriented correctly in a pattern matching the target molecule.

Linker length: The distance between the ligand and multivalent scaffold is designed/optimized for each system to enhance the binding, avoid steric hindrance between the ligands, and provide spatial flexibility²⁸. However, a very long linker can lead to unfavorable conformations, which results in entropic penalties. Sufficiently long linkers can increase the cellular uptake of multivalent structures compared to their long analogs³⁶, increase the surface of multivalent structure and half-life of the drug encapsulated in the construct³⁷.

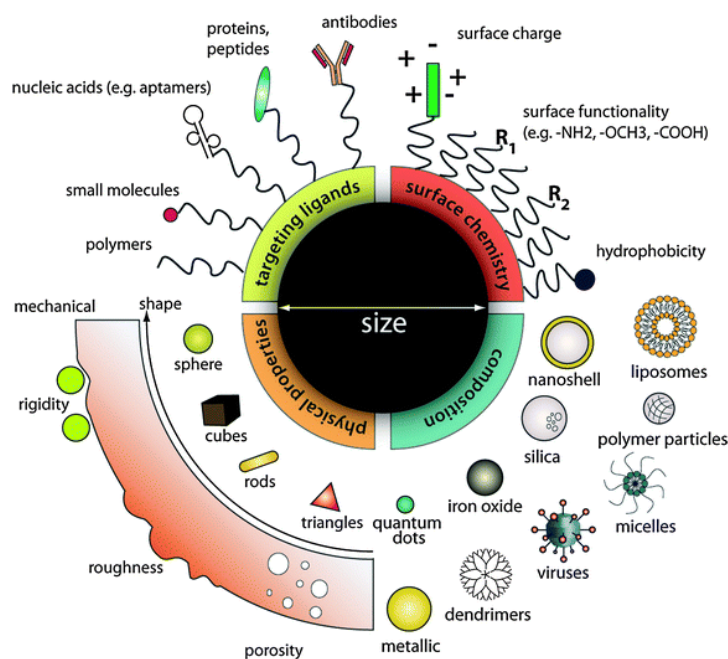


Figure 1.6. Design parameters of nanoparticles. Nanoparticles can be assembled from different materials with different sizes, shapes, surface chemistry and decorated with different ligands. Adapted with permission from Royal Society of Chemistry³⁸.

1.5 Active Selective Targeting

Nanomedicine uses nanotechnology to design and engineer drug delivery systems and its benefits were recognized by different fields such as oncology, vaccinology, and tissue engineering³⁹. However, off-target effects result in unwanted side effects to healthy cells, which is an important bottleneck in the development of new diagnostic and therapeutic tools. Active targeting has been proposed to prevent these off-target effects for undesired toxicities. In active targeting, nanoparticles are decorated with targeting ligands such as antibodies, peptides, aptamers, small molecules to selectively orient the nanoparticle to specific cell type/cell surface biomarker, accumulate at the desired target sites, reduce

side effects, and increase overall efficacy⁴⁰. Cells express different types of biomarkers and receptors on their surfaces which help them to communicate with other cells and their surroundings. The expression level of these receptors is different between cell types. For instance, some cancers highly express human epidermal growth factor receptors (EGFR) and (HER2)⁴¹, vascular cell adhesion molecule-1 is upregulated in kidney ischemia-reperfusion injury⁴², angiotensin II type I receptor is overexpressed in the myocardium during heart attack⁴³. Hence, this receptor density can be used to selectively recognize only the diseased cell by smartly engineered ligands.

In fact, active targeted nanoparticles have always been thought of as ‘magic bullets’ that perfectly target exclusively the diseased cells as seen in Figure 1.7⁴⁴, where nanoparticles are homogeneous in size and the number of targeting ligands and cell surface receptors are only expressed in diseased cells. However, reality is more complex. For instance, when nanoparticles are injected into the bloodstream, they interact with serum proteins, which may hinder their functional side, change their size and stability, resulting in a decrease in efficiency of their targeting to cell surface receptors (shown in Figure 1.7B). Additionally, the engineering of nanoparticles is not homogeneous, which result in the Gaussian distribution of size, charge, and number of ligands. This distribution causes a difference in how each nanoparticle behaves in the cellular environment and in the worst case, 100% of the effect could be caused by 5% of the outliers. Ideally, diseased cells would have a specific receptor which is absent in healthy cells. However, recent advances have shown that the common target receptors are also expressed in healthy cells. For example, epidermal growth factor and transferrin are not only expressed in cancers but also in healthy skin and liver⁴⁵. Therefore, a rational nanoparticle design is required to overcome these limitations to improve the targeting efficiency of particles. This requires a better knowledge of both receptor densities on the cell surface and nanoparticle ligand number. Theoretical models explained the importance of these parameters for selective targeting towards the cell population of interest, which will be explained in the next section.

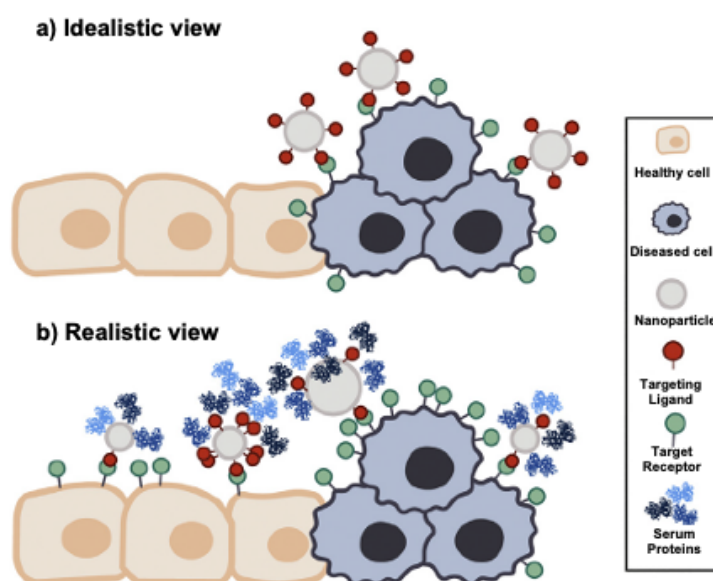


Figure 1.7. Idealistic vs realistic view of active targeting nanomedicines. A) In idealistic view, targeting cell receptors are only presented on diseased cell surface and ligands are presented on nanoparticles homogeneously. B) In realistic view, targeting cell receptors are overexpressed in diseased cell heterogeneously but also expressed in healthy cell which results in off-targeting. Nanoparticles are heterogeneous in size and number of targeting ligands. These ligands can be shielded by protein corona, which influence the targeting efficiency⁴⁴.

1.6 Super-Selective Multivalent Binding

Multivalent structures have more advantages than monovalent ligands by increasing the binding strength³, therefore, it has become recognized as one of the most powerful tools to study targeting⁴⁶. Multivalent architectures increase the ligand local concentration in close spatial proximity of the receptor, hence increasing the probability of ligands rebinding statistically as seen in Figure 1.8A. Multivalency is not only used to enhance binding affinity to cellular targets but can also bring selectivity in ligand-receptor interactions, which is urgently needed in nanomedicine due to off-target toxicity problems. One of the earliest experimental proofs of the selectivity concept was given by Carlson *et al.*⁴⁷ who showed that tumor cells with overexpressed receptors could be selectively recognized over healthy cells by using low affinity, multivalent interactions. In 2011, Martinez-Veracoechea and Frenkel⁴⁸ explained this behavior and presented simulations that show a regime, called ‘super selective’, where the number of bound particles increases nonlinearly with the receptor density on the surface in a multivalent system. This means that a multivalent particle can be very specific for a certain regime, and leaving the surfaces with low receptor densities unaffected, hence, preventing off-targeting and related side effects (Figure 1.8B, C).

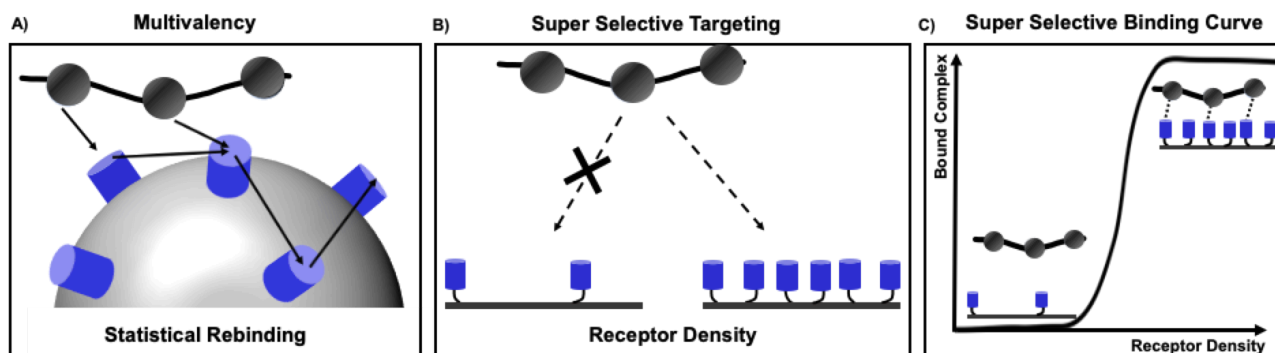


Figure 1.8. A) Statistical rebinding between multivalent ligand and receptor. B) Super selective targeting of a multivalent ligand with respect to different receptor densities. C) Typical binding curve for super-selective targeting.

Super selectivity is an entropic effect, which arises from the entropic gain due to binding combinations of ligands and receptors. For example, when ligands and receptors are in contact, they can bind differently depending on their nature and distances. If the receptors and ligands are more flexible and long, they can bind or unbind to multiple partners. On the other hand, when they are short and spaced far apart from each other, each of them can be bind or unbind to the closest partner. The entropy increase is larger and more favorable when there are more ligands and receptors, hence free binding energy becomes more negative, and the probability of binding increases very fast⁴⁴. Since the monovalent ligand cannot have this binding combination, they cannot be super selective and they show a standard binding mechanism. In Frenkel's studies, they also observed the relationship between the binding affinity and super selectivity: as the binding strength between the binding units becomes weaker, they become more super selective, which also determines the receptor density threshold. For instance, if individual strong binders are presented in a multivalent manner, the overall binding affinity will be very strong, and when they are in contact with cells, they will likely bind to cells with minimal receptor density, showing no selectivity. In other words, strong binders decrease the receptor density threshold, hence no selectivity, and weak binders increase the receptor density threshold, hence increasing the selectivity.

They also claimed that more flexible structures would be able to form more ligand-receptor pairs, which will enhance their selectivity. To confirm their claim, they designed a model system based on host/guest interactions to study interactions of hyaluronic acid-functionalized host molecules with surfaces of different densities of guest molecules⁴⁹. In the other model system, the same group studied the effects of binding affinity, valency, linker, and ligand concentration on polymer's super-selectivity⁵⁰. To sum up, they concluded that i) monovalent ligands show very low selectivity to their target receptors regardless of their binding strength, and their binding profile changes linearly with the receptor density: ii) multivalent systems show an on/off binding profile, super-selective behavior, their binding profile changes nonlinearly with the receptor density and the particles saturate the surfaces with a receptor density above a threshold value, iii) selectivity inversely increases with equilibrium association constant of individual ligand-receptor pair, iv) flexible scaffolds are needed to have a super-selective profile. Additionally, they claim to have flexible and high valency ligands for super-selective profile, in nature, however, the number of ligands and receptors are often low to moderate and their position is space quasi-controlled¹⁸. Flexible particles can also occupy and make a crowd around the target molecules, which will hinder other molecules' binding. On the other hand, in nature, rigid multivalent particles are exploited such as the activation of certain Toll-like receptors⁵¹.

In line with these observations, the effect of ligand valency and cell receptor density on the binding and cell uptake was studied. The nanoparticles with high ligand valency showed switched-on cellular uptake profile when threshold of receptor density was reached⁵². DNA-coated colloidal particles have been used to study super selectivity, where colloidal particles were coated with a different number of DNA sequences and their aggregation rate was measured. It was found that particles with fewer complementary bases (weaker interaction) showed a higher binding selectivity⁵³. Overeem *et al.* developed a biosensor, called the multivalent affinity profiling chip, to study the binding profile of influenza A virus with the glycocalyx of host cells on receptor density gradients to determine the threshold receptor density by imaging the colocalization of virus and the receptors, which then allowed direct visualization of super selectivity of the virus⁵⁴.

Recently the Battaglia and Angioletti-Uberti labs⁵⁵ have introduced a different type of selective targeting, which they call 'range selectivity', where the selectivity is caused by the repulsive forces. In other words, multivalent particles bind receptors where the receptor density is within a certain range, but not below or above. According to their system, this range of receptor density can be controlled by tuning attractive and repulsive forces such as binding strength between ligand and receptor, the volume of the receptors, the density of polymer brushes around the nanoparticle.

We hypothesize that selectivity can also be enhanced by spatially controlling the targeting ligands. Spatially pre-formed ligands for their target could provide an effective engagement based on recognition of the nano geometry carried in the system. Control over geometry and spatial tolerance in nanomaterials is uniquely achieved if all the interactions of the molecules can be designed. DNA nanotechnology promises to be the ideal platform to explore this challenge. Designing spatially controlled multivalent particles which will be explained in the next section has many benefits for particles' selectivity and function⁵⁶.

1.7 DNA Nanotechnology

Deoxyribose nucleic acid (DNA) is a polymer composed of four nucleotides: adenine (A), thymine (T), guanine (G), and cytosine (C), which is more than a genetic information carrier. It has been widely used as a building block for different nanomaterials due to its excellent sequence programmability⁵⁷. In 1953, James Watson and Francis Crick, with insight from X-ray diffraction studies by Rosalind Franklin and Maurice Wilkins, proposed the first three-dimensional model of DNA⁵⁸, where two single stranded DNA (ssDNA), turn around the same axis in a right-hand helix. The strands are anti-parallel and complementary to each other and structurally well defined on the nanometer scale, presenting a persistent length of ~50 nm under conventional conditions. The diameter of the DNA double helix is between 2-2.5 nm and one turn of a helix (10.5 base pairs/turn) is 3.4-3.6 nm (Figure 1.9A)⁵⁹. These nanoscale dimensions of DNA make it a programmable platform for the controlled construction of nanoscale features. Since the pioneering work by Ned Seeman to use DNA as a physical material to assembly of nanoscale architectures in 1982 (Figure 1.9B)⁶⁰, the structural DNA nanotechnology has been growing exponentially. Different assembly techniques e.g., tile and brick assembly were successfully used to create various lattices wireframe DNA nanostructures (Figure 1.9C)^{61,62,63,64}.

The turning point for DNA nanotechnology came by the invention of DNA origami by Paul Rothemund in 2006. DNA origami is a technique to self-assemble of DNA nanostructures by folding a long single-stranded (ss) DNA `scaffold` with hundreds of short synthetic ssDNA, called `staples` through Watson-Crick base pairing into customized shape, in which DNA double helices are bound together by double crossovers between neighboring DNA helices⁶⁵. DNA origami technique requires the presence of Mg^{2+} cations in the sample solution to overcome the repulsion between the negatively charged DNA backbones. The staple strands are added in excess since it does not require an exact stoichiometry. This technology was rapidly adopted and was used to generate 3D structures (Figure 1.9D,E)^{66,67}.

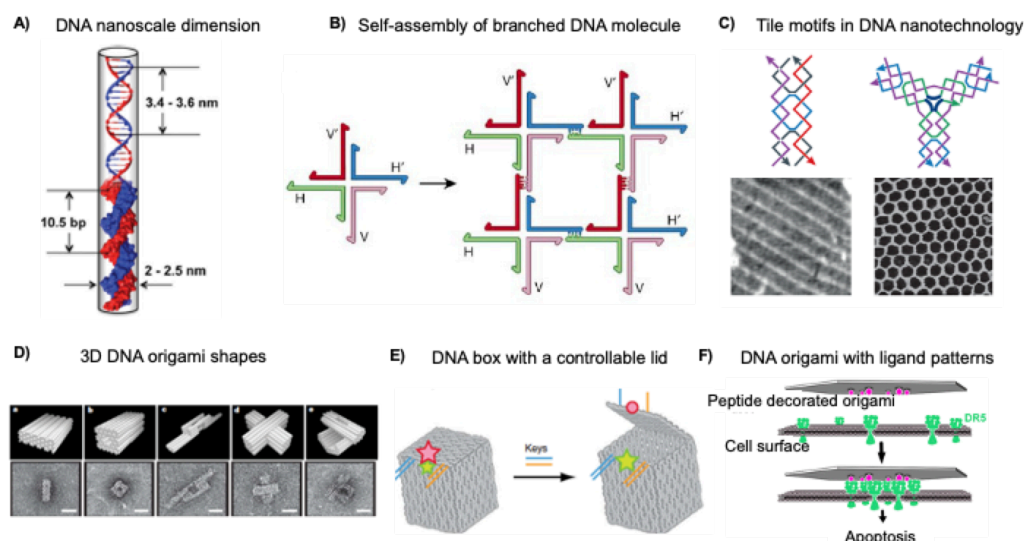


Figure 1.9. A) Schematic illustrating the structure of B-form DNA⁵⁹. B) Schematic illustration of four-arm junctions with single-stranded sticky ends, which allows larger structures assemblies⁶⁸. C) DNA nanotechnology motifs. The top panel shows tile motifs in DNA nanotechnology, the bottom panel shows the AFM images of their assemblies into lattices^{69,70}. D) 3D DNA origami shapes. The top panel shows perspective views of cylinder models, each cylinder representing a DNA double helix. The bottom panel shows the TEM images of the assembled particles⁶⁶. E) A megadalton-sized DNA box with a controllable lid⁶⁷. F) Schematic illustration of how apoptosis can be triggered by peptide patterns on DNA origami template⁷¹.

One of the mostly appealing application of DNA nanotechnology is in biomedicine, drug delivery, and targeted therapy⁷². The DNA nanostructures have been explored over the years for diverse biological and biomedical applications for several reasons: i) its inherent biocompatibility, ii) its precise spatial addressability at the nanometer scale, iii) modification of the strands such as with organic fluorophores and photoresponsive moieties chemically, if necessary, iv) high monodispersity, v) functionalization with targeting moieties such as a small molecule, protein, nucleic acid moieties⁷³. For example, Tian *et al.* modified framework tetrahedron DNA probe with peptides to enhance brain permeability and target brain tumors. These DNA nanoprobe successfully passed through the blood-brain barrier (BBB) and entered the cytoplasm of the tumor cells⁷⁴. Cremers *et al.* investigated tunable design parameters of antibody functionalized DNA structures binding to therapeutically relevant receptors including programmed cell death protein 1 (PD1), epidermal growth factor receptor (EGFR), and human epidermal growth factor receptor 2 (HER2) receptors. They found that receptor binding is mainly governed by nanostructure orientation and size, and DNA handles location. Their studies revealed that larger particles had a limited receptor binding because of steric hinderance⁷⁵. Ma *et al.* designed a anti-HER2 aptamers functionalized tetrahedral shape DNA robot, and observed the reduced amount of HER2 on the cell surface which induced apoptosis of the breast cancer cells. They also demonstrated the increased circulation time of aptamer functionalized DNA particles compared to bare aptamer injection in murine models⁷⁶. Recently, Wang *et al.* studied the effect of ligand spatial patterns to induce death receptor clustering and a resulting apoptosis⁷¹. They observed effective apoptosis with sub-10 nm inter-peptide distance in a hexagonal pattern. They also observed more efficient death receptor clustering and apoptosis when using the stiffer (more rigid) DNA-origami structures. This study clearly shows the importance of precise spatial pattern screening for exploring targets in biology (Figure 1.9F). The given examples clearly show that DNA nanotechnology is a very appealing technology for applications in nanomedicine to its ability to control the shape, scaffold size, and ligand presentation with nanometer-scale precision.

1.8 Statement of the Thesis

This thesis describes the use of DNA nanotechnology to engineer spatially-controlled multivalent materials that allow to study the effect of rigity and spacing on super-selective multivalent interactions. We aim to explore what happens in the scenario where the spatial tolerance of the ligand presenting architecture matches the spatial organization of the surface receptors. In this concept, we investigated the effect of rigidity, binding affinity, and ligand valency on the particles' binding behavior and their influence on super-selectivity.

Chapter 2 discusses the design and characterization of the DNA nanoparticle library, which is composed of DNA-bivalent and hexavalent scaffolds. Nanoparticle design parameters, self-assembly methods, and characterization techniques are explained. This chapter also includes the modeling of DNA bivalent structures and ends with the explanation of spatial tolerances of each nanoparticle designed.

Chapter 3 describes the surface characterization. Since super-selective multivalent binding is characterized by a strong density-dependent onset of ligand-receptor complexation, the density of the receptors on the surface needs to be controlled and characterized adequately. This chapter explains the model receptors used in the selectivity assays, the

quantification of adsorbed proteins on the surface with different techniques. Lastly, the mathematical model describing the spatial organization of receptor distribution on the surface at a given density is explained.

Chapter 4 demonstrates that a form of super-selective binding based on rigid patterns, which we call multivalent pattern recognition (MPR), can be achieved when the rigidity defines the onset of binding for super-selective binding. First, the chosen ligands and their binding affinity profiles towards the model receptors are explained. Then, the binding profiles of two different ligand-receptor systems are characterized using different analytical techniques to obtain both kinetic and static affinity data. The ideal conditions in terms of rigidity, valency, and affinity of the ligands to achieve MPR are proposed.

Chapter 5 summarizes the important conclusions of this thesis and proposes additional studies for the near future. Overall, this thesis demonstrates the significance of spatial tolerance in nanomaterials to obtain multivalent pattern recognition. The concepts demonstrated here could be the fundamental phenomenon behind many natural and chemical multivalent processes and an inspiration to explore targets in biology that follow this mechanism.

Chapter 2 Design and Characterization of a Multivalent DNA Nanoparticle Library

Using DNA as a scaffold for ligand functionalization for multivalent ligand display is appealing due to its ability to control the size, shape, valency and spacing with nanometer precision. DNA nanotechnology poses itself as the ideal engineering platform as self-assembly is directly linked to base-pairing and rigidity related to sequence length as well as single or double-stranded assemblies. Additionally, complexity ranges from extremely low (a single helix) to extremely high, in the case of DNA-origami^{65,66,77} where hundreds of strands self-assemble together into a hierarchical architecture. In this thesis, we explore the influence of ligand valency and spatial tolerance on super-selective multivalent binding. In this chapter, we describe the design of our particle library, consisting of an antibody inspired bivalent Y-shaped architectures with different spatial tolerances and rigidity. Additionally, in order to compare these bivalent structures with higher valency arrays, DNA-origami disks with a multivalent ligand display are designed and characterized. Modeling of DNA bivalent structures was performed by Vincenzo Caroprese.

Part of this chapter is in preparation for submission: “Multivalent Pattern Recognition Through Engineering of Spatial Tolerance in DNA-Based Nanomaterials”; Hale Bila, Kaltrina Paloja, Vincenzo Caroprese, Artem Kononenko, Maartje M.C. Bastings.

2.1 Design, Self-Assembly, and Characterization of Bivalent Structures

For the development of ligand-functionalized materials that allow for the engineering of spatial tolerance in their ligand presentation, we followed a modular design that can provide a minimal multivalent (bivalent) structure. Relying on the self-assembly guided by Watson-Crick base pairing, three single-strand DNA (ssDNA) molecules organize with high fidelity into branched Y-shaped nanostructures (tripods) (Figure 2.1). Two arms serve to connect a binding ligand to generate a bivalent structure, while the third arm allows to introduce a label for quantification of binding.

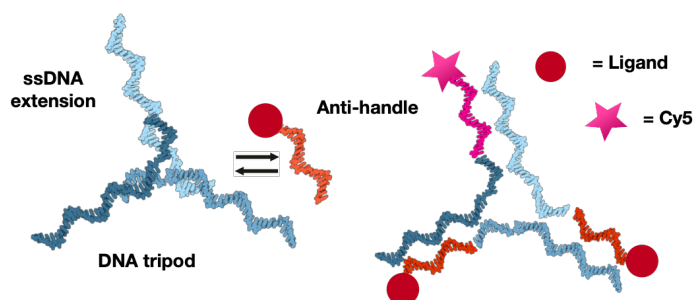


Figure 2.1. Schematic illustration of bivalent structure (tripod), showing how the ssDNA strands coordinate the self-assembly and ligand functionalization. Ligand in orange, dye for detection purposes in pink.

Rigidity/flexibility is an important factor affecting the binding affinity of multivalent ligands to their targets. There has been much debate about the effect of flexibility in multivalent systems. The more flexible the scaffold is, the better it can adapt to the geometry of the receptor, but on the other hand, the more pronounced the entropy penalty is, which affects the overall interaction strength. This simple argument shows that careful choice of ligand scaffold and its effect on binding affinity should be investigated. For instance, Netz's group studied the length and flexibility of the spacers and derived a general rule for the optimal ligand design. They showed that a divalent ligand binds more efficiently than a monovalent analog if the monovalent dissociation constant is lower than a critical value which depends on the ligand-spacer length, flexibility, and size of the receptor. They found that for rigid ligands, average end-to-end spacer length should be equal to or slightly smaller than the distance between the receptor binding pockets and end-to-end spacer length fluctuations should be in the same range as the size of the receptor-binding pocket. Whereas the average end-to-end spacer length of a flexible ligand should be smaller than the binding pocket distance⁷⁸.

To evaluate the rigidity parameter and variation in absolute spacing of the ligands, we designed three different structures, for the low spatial-tolerance long bivalent (LB) and short bivalent (SB) analyte, all nucleotides have binding partners, whereas, for the high spatial-tolerance flexible bivalent (FB) structure, we included non-base-paired oligo-T sections in the core of the architecture. The DNA sequences for the rigid LB were designed according to Mohri *et. al.*⁷⁹ but are extended by a novel ssDNA region to allow for functionalization. The SB was designed by removing bases from the strands of LB construct and we kept minimum of 10 bases per arm for stability. The flexible bivalent structure was designed by adding extra non-base-paired oligo-T nucleotides in the core of the SB. We used NUPACK, a software for the analysis and design of nucleic acid systems, to confirm their self-assembly (Figure 2.2) The sequences of each ssDNA are presented in Table 6.1 in appendix.

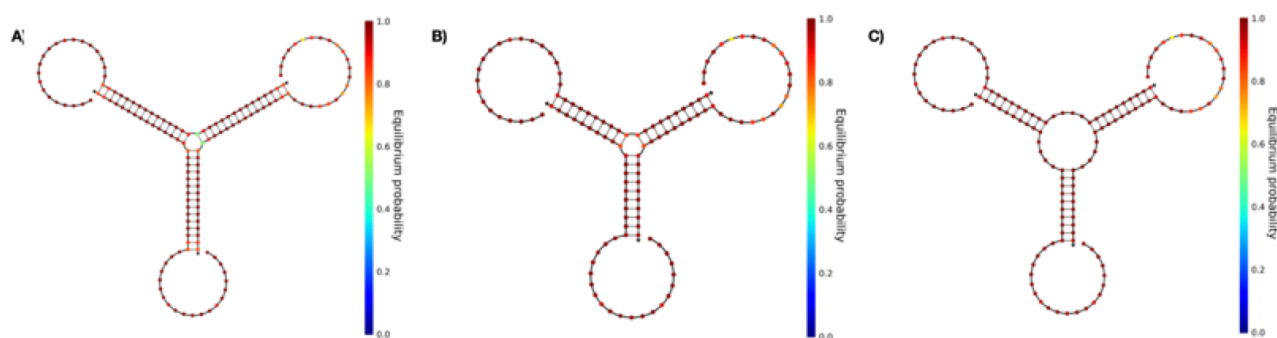


Figure 2.2. NUPACK pictures of A) long bivalent, B) short bivalent, and C) flexible bivalent structures. This analysis shows that all structures are formed in high fidelity and no secondary particles are assembled.

Each construct was prepared by mixing equimolar amounts of ssDNA. Each ssDNA was dissolved in annealing buffer (5 mM Tris, 1 mM EDTA, 150 mM NaCl and 10 mM MgCl₂). Self-assembly of the architectures were performed according to following protocol:⁸⁰ i) Denaturation at 95 °C for 2 min. ii) Cooling at 65 °C and incubation for 5 min. iii) Annealing at 60 °C for 2 min. iv) Further annealing at 60 °C for 0.5 min with a continuous temperature decrease at a rate of 1 °C per min. The annealing steps were repeated a total of 40 times. The final annealed assemblies were stored at 4 °C. Then, tripods were annealed with anti-handle ssDNA and peptide conjugates at 37 °C for 1 h. The final functionalized particles were characterized by 10% Tris-Glycine PAGE gels at 150 V, 1h (Figure 2.3).

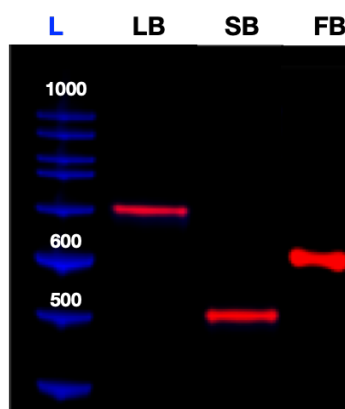


Figure 2.3. 10% Tris-Glycine PAGE gel electrophoresis of bivalent structures. L: DNA ladder, LB: long bivalent, SB: short bivalent, and FB: flexible bivalent constructs. The electrophoresis was run at 150 V for 1 h.

2.1.1 Modeling of DNA Bivalent Structures

Since we aim to explore the density-dependent super selective binding of our DNA particle library, it is important to know the end-to-end distance between ligands. Therefore, we performed molecular dynamics simulations from which we can determine the end-to-end distances of DNA bivalent assemblies (tripods). To do so, we used a divide and conquer approach, deciding to not simulate the particles as a whole, but as portions to study separately and then reconstruct. The first portion of interest that we defined is in the following referred as “core”. A core consists of a 3-way junction composed by arms of 10 nucleotides (Figure 2.4). For each design, a first de novo configuration was manually constructed by considering results from Nupack and examples with similar structures in literature⁸¹, using nanoengineer-1⁸², and a web tool provided by The Aksimentiev group⁸³ for files conversion. After a first round of simulations, we selected the last conformation observed as starting conformation for a second set. The second portion of interest is called “arm” and it is the segment that links the ligand functionalization to the junction. To prepare the initial conformations, crystal structures of dsDNA in B conformation were prepared through the Nucleic Acid Builder tool of ante-chamber⁸⁴ and manually edited to reproduce the nick between a core strand and the functionalization in antisense. Calculations were run using Gromacs 2019⁸⁵. The forcefield applied consisted in AMBER 14 SB⁸⁶ with the param bsc1 modifications for DNA⁸⁷, Chetam’s parameters for the ions⁸⁸ and SPC/E as solvent model⁸⁹. Salt concentration was set at 10 mM of MgCl₂. Aside for some small variations, settings for all the Molecular Dynamics simulation followed the examples reported in the papers of the Ascona B-DNA Consortium^{90,91,92}.

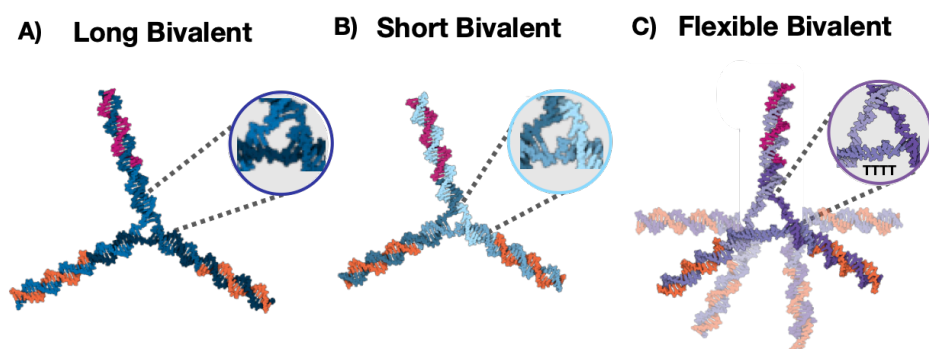


Figure 2.4. MD simulations of the bivalent structures with spatial tolerances. A) long bivalent, B) short bivalent, C) flexible bivalent structures.

We run the simulations in triclinic boxes, built in a way that the principal direction of the box follows the orientation of our particles and imposing at least a distance of 2 nm from the boundaries for all the atoms of the particles in what

would be the most extensive possible configuration. We set temperature and pressure at 300K and 1 bar respectively when restrained and 1 nm as cut-off for short ranged electrostatics and Lennard–Jones interactions. During the production run we used a Parrinello-Rahman barostat⁹³, and a Nosè-Hoover thermostat⁹⁴, while during equilibration phase Berendsen's thermostat and barostat were implemented⁹⁵, LINCS⁹⁶ was used to restrain covalent bonds of hydrogens. We performed production run for a total of 160 ns per starting conformations. The integration scheme was a classical leap-frog algorithm with a 2fs time step. A classical buffered Verlet list was set to report neighbours within a minimum volume of radius of 1.2 nm. The precise value and other settings not listed were optimized by default by the GROMACS mdrun algorithm for GPU accelerations.

The sequence for equilibration was inspired from the one adopted by the Ascona Consortium. While restraining the heavy atom in the DNA, we performed a sequence of energy minimizations followed by equilibration runs. At each cycle we slowly release the restraints from the DNA passing in order through 1046, 210, 168, 126, 84, 42, 21 kJ/mol/nm. The first equilibration run was performed for 100 ps at NVT while the others consisted in 50 ps of restrained NPT. After this cycle we performed a last equilibrium run of 20 ns at the same conditions of the subsequent production run. The analysis of the resulting trajectories uses frames collected every 2 ps from the last 140 ns.

For the molecular dynamics of arms and reconstruction, the software and simulation pipeline were used in a similar fashion except the total simulation time was 40 ns for each initialized structure. Average arm length was evaluated by measuring the end-to-end distances. The conformation closer to the average distance was then extracted and rigidly superimposed on the correspondent core using GROMACS tools. In particular we used the common bases between core and arms to reconstruct the whole particles as references for a least square fit of the positions. The distances between the COM of the last base pairs of each of the fitted arms were measured with the software VMD96. The reconstructed particles were then sampled to obtain the mean arm-arm distances and end-to-end variability that defines the spatial tolerance is presented in the form of probability distribution (Figure 2.5). The end-to-end distances are 16 ± 1 nm, 13 ± 2 nm, and 12 ± 6 nm for LB, SB, and FB respectively. It is worth noting that flexible design can be found in three different conformations (Figure 2.6), hence, spacing and span a range of 6 -18 nm in spacing, which is relatively higher compared to rigid long and short structures, given its flexibility.

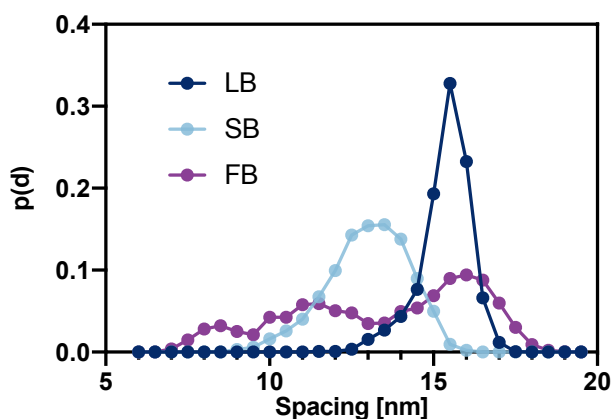


Figure 2.5. Probability distribution ($p(d)$) of end-to-end distances of each bivalent structure. Long bivalent (LB), and short bivalent (SB) have one conformation whereas three conformations for flexible bivalent (FB) design exist.

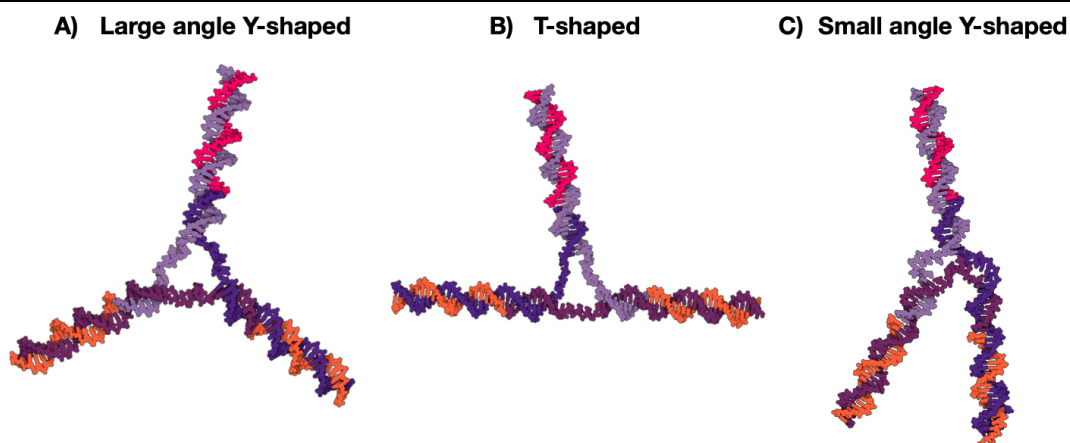


Figure 2.6. Three conformations of flexible bivalent obtained from snapshots of the MD simulations. These clearly show the variation of end-to-end distances present in this flexible structure. A) Large angle Y-shaped, 11 ± 2 nm, T-shaped, 16 ± 2 nm, C) Small angle Y-shaped, 8 ± 2 nm.

2.2 Design, Self-Assembly and Characterization of DNA-Origami Disks

To access a higher valency and explore spatial tolerance in more complex system multivalent ligand patterns, DNA-origami disks were used as scaffolds. Previously, in our laboratory, the self-assembly and characterization of ligand patterns on a 60 nm diameter disk with a six-helix bundle cross-section, which yields rigidity, was designed using the DNA origami technique (Figure 2.7A)⁹⁷. These DNA-origami disks display 2×36 , 7 nm-regularly spaced attachment points on both faces of the structure were designed. At these attachment points, DNA can be prolonged with single stranded extensions, called 'handles' to hybridize with their complementary sequences, 'anti-handles'. Position specific staples with corresponding staple handle can be substituted during annealing to have different patterns on the disk surface, which enables the presentation of prescribed number of ligands with predetermined spacing with nanoscale precision⁹⁷. To access a higher valency as well as explore the spatial tolerance in multivalent patterns, we decided to use an equally spaced hexagonal pattern as this is a multivalent pattern often used in nature⁹⁸. The spacings of the ligands in the hexagonal array was controlled through selection of different functional sites in the disk, resulting in a large hexagon (LH), and small hexagon (SH) pattern. The spatial tolerance of the SH was modified via the inclusion of unpaired, single-stranded sections in the functional handles on the disk (flexible hexagon, FH) (Figure 2.7C).

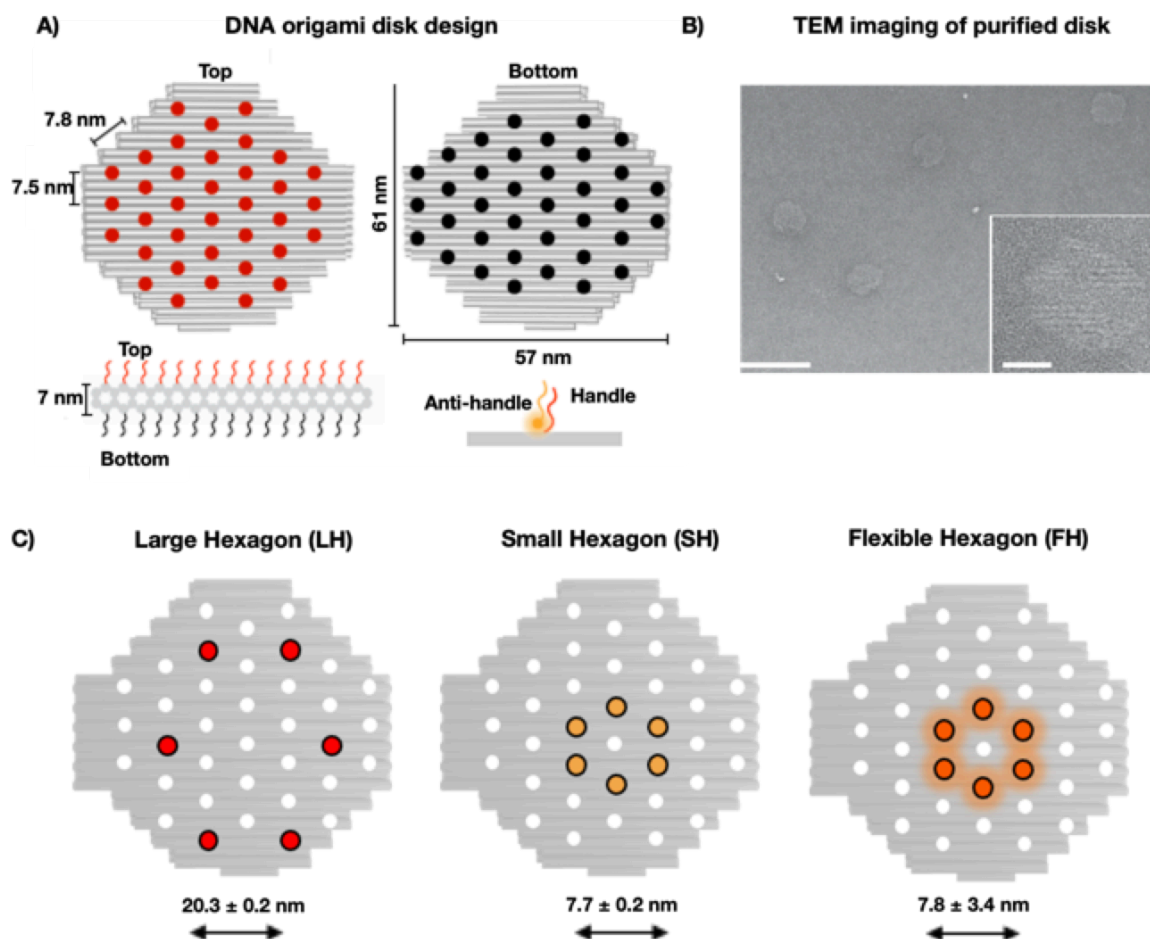


Figure 2.7. A) DNA Origami disk design of both faces, top and bottom, and introduction of 2 x 36 attachment points. Side view, showing the six-helix bundle with a thickness of 7 nm (bottom left). Functionalized anti-handle handle representation (bottom right). Adapted with permission from ACS NANO⁹⁷. B) TEM images of a purified disk and zoom-in of a selected disk (bottom right). C) Schematic representations of different pattern designs of DNA-origami disks: Large Hexagon (LH), Small Hexagon (SH), and Flexible Hexagon (FH) with the distances measured by DNA-PAINT for LH and SH and calculated for FH.

DNA origami disks (hexavalent scaffolds) were self-assembled as previously described⁹⁹, at 20 nM final concentration in a final volume of 50 μ L, containing 20 nM p7560 scaffold (sequence Table 6.2), 140 nM staples (7x in excess) in 1x folding buffer containing 5 mM Tris, 1 mM EDTA, 5 mM NaCl, 18 mM MgCl₂. The annealing mixture was transferred in PCR tubes and subjected to a thermal annealing ramp. The samples were heated to 80°C for 5 minutes, held at 60°C for 1 hour and cooled at a rate of 1°C/hour from 60°C to 20°C. The samples were stored at 4°C. The buffer was filtered with 0.22 μ m PES syringe filters. Excess staples were purified with Amicon 100 K filter tubes. The process includes 6 times washings with the folding buffer (buffer B) at 5000 g for 2 min. After purifying the DNA-origami disks, the concentration was measured by absorbance at 260 nm on the nanodrop. The purified samples were kept at -20 °C. The purified DNA origami disks were imaged by TEM (Figure 2.7B) and characterized by 1% agarose gel electrophoresis (Figure 2.8). The gel was cast in 0.5x TBE buffer supplemented with 8 mM MgCl₂ and 7 μ L SYBR Safe. 10 μ L of samples were mixed with 2 μ L of 6x loading dye and run in a 0.5x TBE buffer supplemented with 8 mM MgCl₂ at 60 V in an ice-water bath.

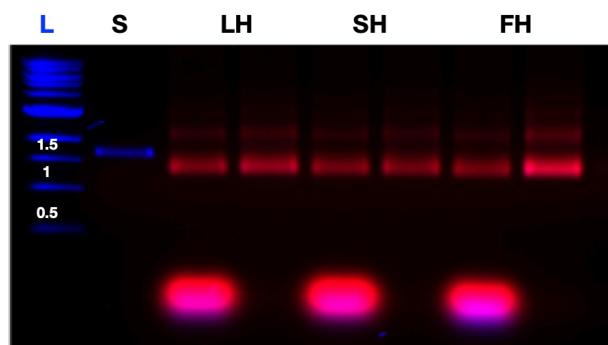


Figure 2.8. 1% agarose gel electrophoresis analysis of 1 kb ladder (L), scaffold (S), and disks (LH, SH, FH) before and after the purification. It was run at 60 V for 2 h in an ice-water bath. (Scan for SYBR Safe in blue, and Cy5 in red).

Distances of functionalization points of LH and SH patterned DNA-origami disks were measured previously by DNA-PAINT and found to be 20.4 nm for LH and 7.8 nm for SH matching the simulated distances⁹⁷. The added flexible extensions introduce an estimated spatial uncertainty of 7.8 ± 3.4 nm (Figure 2.9).

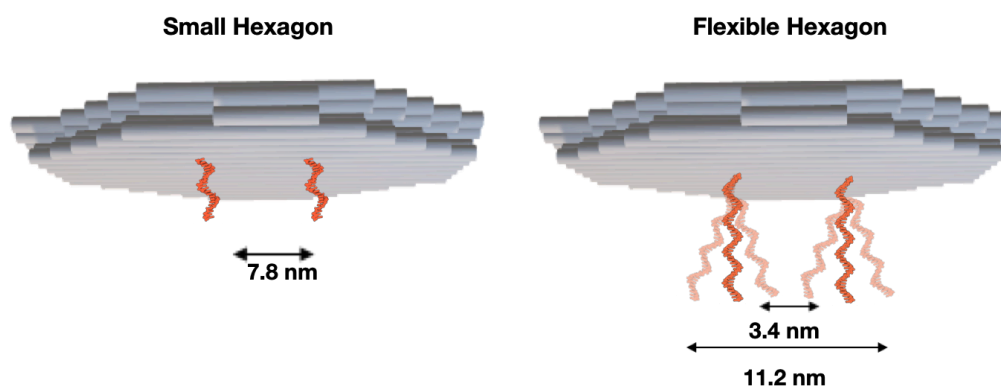


Figure 2.9. Schematic representation of the flexible hexagon with spatial tolerance compared to the rigid small hexagon.

Since all position on the DNA origami disk can be individually addressed, control architectures with different valencies can be easily engineered. We designed a monovalent functionalized disk (1x handle) as a control in order to evaluate multivalency effect to compare it to hexavalent functionalized disks (LH, SH, FH). Characterization is presented in the form of gel electrophoresis in Figure 2.10.

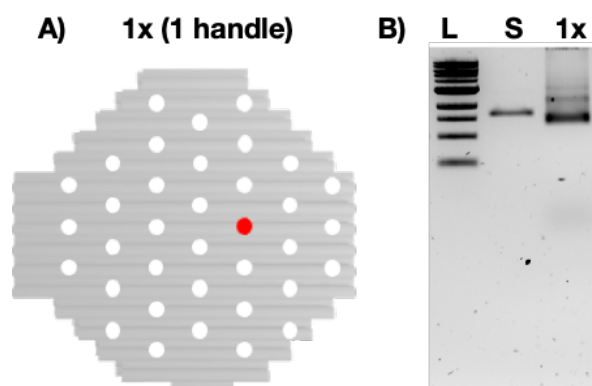


Figure 2.10. A) 1x (1 handle) DNA-origami disk design, B) 1% agarose gel electrophoresis analysis of 1kb ladder (L), scaffold (S), and 1x (1 handle) disk design. It was run at 60 V for 90 min in an ice-water bath.

2.3 Conclusion

In this chapter, we focused on the design and characterization of bivalent and hexavalent scaffolds for use as multivalent probes in following super selectivity binding assays. We showed that DNA bivalent (tripods) and hexavalent (disks) were successfully self-assembled with almost 100% yield and characterized with PAGE and agarose gel electrophoresis respectively. Bivalent particles' stability and fidelity were confirmed with NUPACK analysis. Molecular dynamics simulations were performed to calculate the spatial tolerances of the DNA bivalent structures, showing that rigid LB and SB have low spatial tolerances 16 ± 1 nm and 13 ± 2 nm respectively, whereas FB has three different confirmations with high spatial tolerance, 12 ± 6 . Distances of the functionalization points of large and small hexagon patterned DNA-origami disks were measured previously⁹⁷ and 20.4 and 7.8 nm respectively. In this thesis, the spatial tolerance of the flexible hexagon pattern was calculated and found to be 7.8 ± 3.4 nm. With the library of DNA based nanomaterials complete, we need to shift focus to design target surfaces that can display a variable receptor density. As super-selective binding is characterized by a sharp onset at a specific density, we expect this to be even more pronounced in pattern-based multivalency. A proper control over surface assembly is thus crucial, on which we will focus in the next chapter.

Chapter 3 Multivalent Surface Preparation and Characterization

As in the case of super-selective multivalent binding (section 1.6), we expect the density of surface receptors to be of critical importance in pattern-based multivalency. Therefore, in this chapter we focus on the preparation and characterization of proteins used as receptor, their immobilization on a surface, and the quantification of adsorbed proteins and density gradients. Simulations and mathematical analysis to obtain the experimental preparation guidelines for the surface densities were performed by Vincenzo Caroprese, and the qPCR experiments were designed and performed by Artem Kononenko.

Part of this chapter is in preparation for submission: “Multivalent Pattern Recognition Through Engineering of Spatial Tolerance in DNA-Based Nanomaterials”; Hale Bila, Kaltrina Paloja, Vincenzo Caroprese, Artem Kononenko, Maartje M.C. Bastings.

3.1 Streptavidin and Streptactin as Model Receptors

Streptavidin (SA) is a tetrameric protein of approximately 60 kDa in size and secreted by the bacterium *Streptomyces avidinii*. Each subunit is hydrogen-bonded to each other and forms a symmetric dimer. SA binds tightly to a small growth factor, biotin. Each subunit of SA can bind one molecule of biotin (Figure 3.1A), with a high-affinity $K_D = \sim 10^{-14}$ M, known as the strongest non-covalent interaction in nature¹⁰⁰. The streptavidin-biotin couple has been widely used in several biotechnological applications, as via the strong interaction between them, different biomolecules can be coupled to one another or onto a solid support. Harsh conditions are required to break this interaction such as incubation in water above 70°C. Streptavidin can be coated directly to the solid substrate (such as a common polystyrene well plate) or through an interface layer that consists of a carrier molecule. Adhesion could be based on physisorption or other interactions such as covalent coupling¹⁰¹. As such, it has been used in previous multivalent binding assays, which focused on the effect on flexible ligand valency and surface density to overall interaction avidity.

Similar to SA, streptactin (ST) is an engineered form of tetrameric streptavidin with four identical subunits, each with a high affinity biotin ($K_D \sim$ low pM range) binding site¹⁰². It specifically binds to the genetically encodable peptide Streptag II (Trp-Ser-His-Pro-Gln-Phe-Glu-Lys). Strep-tag II peptide binds the same binding pocket in SA and ST proteins as biotin would¹⁰³. According to crystal data both the Streptag II N and C terminus are accessible when bound to ST (Figure 3.1B)¹⁰⁴. Streptactin-Strep-tag II interaction is generally used in protein purification¹⁰⁵, affinity imaging, and various *in vivo* applications¹⁰⁶. In this thesis, we coated the well plate with streptavidin and streptactin through adsorption. They adsorb spontaneously to the polystyrene surface, which is a hydrophobic surface facilitating protein adsorption.

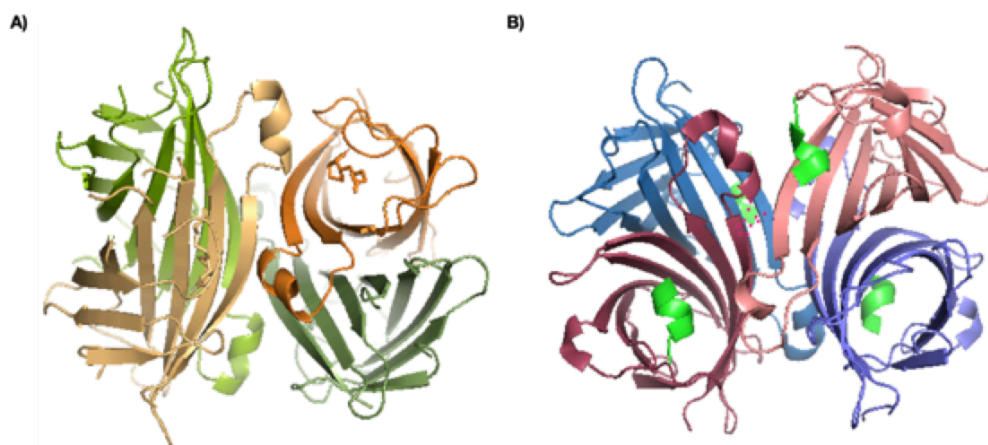


Figure 3.1. A) Three-dimensional structure of streptavidin. The ribbon diagram shows the intercalation of biotin molecules in the binding pockets. The image was obtained by the Protein Data Bank entry 1SWE¹⁰⁷. B) Three-dimensional structure of Streptactin (ST). The ribbon diagram shows the intercalation of streptag II peptide in the binding pockets. The image was obtained by the Protein Data Bank entry 1KL3¹⁰⁴.

3.2 Characterization of Protein Coated Surfaces

Streptavidin was purchased from Apollo Scientific and delivered as lyophilized powder, then dissolved in TBS buffer to make the stock solution of 20 μM and stored in aliquots at -80°C . Streptactin was purchased from IBA and delivered as lyophilized powders. It was dissolved in a PBS buffer to make the stock solution of 20 μM and stored in aliquots at -80°C . The concentration of the stock solution of the proteins was confirmed by Micro-BCA protein assay according to the manufacturer's protocol. This method uses bicinchoninic acid (BCA) as the detection agent for Cu^{+1} , which is formed when Cu^{+2} is reduced by protein in an alkaline environment. A purple-colored reaction product exhibits a strong absorbance at 562 nm, which is linear with increasing protein concentrations. The absorbance was read on a BioTek™ Cytation 5™ at 562 nm wavelength.

The purity of the proteins and their interactions with biotinylated DNA was characterized by PAGE gel electrophoresis analysis, which is a technique that is used to separate molecules according to electrophoretic mobility. Since DNA backbone is negatively charged, when the samples are subjected to electric field, the DNA molecules migrate to the positive pole. The DNA molecules must pass through a porous gel matrix, the smaller molecules pass through these pores easily than bigger molecules, meaning that smaller molecules move through the gel faster which results in separation of the molecules. After the electric field is removed, positions of the molecules are determined by a reference ladder (either protein or DNA ladder, with predetermined sizes) with the help of staining the gel. SA and ST were annealed with biotinylated-Cy5 functionalized ssDNA (in excess) at RT for 30 min. They were then loaded on a 4-20% Native Page gel and ran for 90 min at 120 V. The gel was scanned with Cy5 channel to see their interactions. Then, the gel was stained with Instant Blue for 30 min to visualize the proteins. Figure 3.2 shows the purity of SA and ST, and their interaction with biotinylated ssDNA. Because of negative charge of the DNA, it runs faster than the proteins alone. The gel confirms the purity of SA and ST proteins.

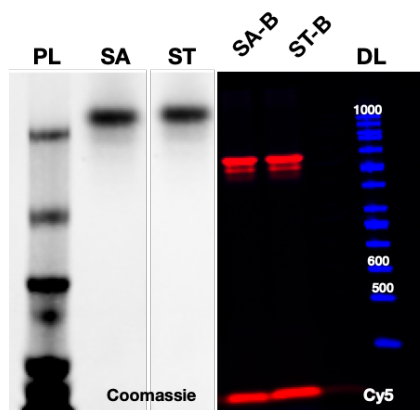


Figure 3.2. 4-20% Native-PAGE analysis of protein ladder (PL), streptavidin (SA), and streptactin (ST), SA-biotin and ST-biotin. The gel was run for 90 min at 120 V and scanned on Coomassie and Cy5 channels.

3.2.1 Preparation and Quantification of Adsorbed Protein

Adsorbed protein on the 96-well plate was quantified by quantitative Polymerase Chain Reaction (qPCR) and solid-phase fluorescence assays. A dilution series was prepared, and protein was incubated with a serial dilution range from 300 nM to 0 nM to understand the amount needed on the surface to form a monolayer surface in a high binding, half-area, 96-well plate, overnight at 4°C. After washing the unbound protein 3 times with 100 μ L buffer, 70 μ L blocking buffer per well was added (corresponding buffer with 2% BSA) in order to prevent nonspecific binding. The plate was incubated at RT for 1h. After washing 3 times with 100 μ L buffer, 35 μ L biotinylated-Cy5 functionalized ssDNA was incubated for 1 hour at RT. 35 μ L of Cy5 functionalized ssDNA as calibration curve dilutions were added in duplicates in respective wells. After washing 6 times with 100 μ L buffer, fluorescence intensity of Cy5 was monitored. This experiment was carried out in quintuplicate. The raw data was treated by subtracting the background from the maximum intensities of washing buffer control wells and scaling intensities of 50 nM Cy5 concentration (Figure 3.3). This assay confirms a full monolayer immobilization of proteins is occurring when using a stock solution of 50 nM of the protein.

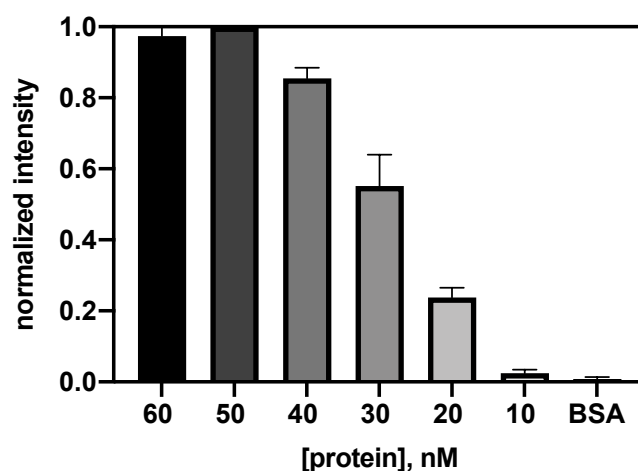


Figure 3.3. A) Solid phase binding assay of biotinylated ssDNA functionalized with dye (Cy5) on protein-coated surfaces with decreasing densities. Error bars represent \pm SD.

PCR is a widely used technique to amplify and detect DNA and RNA sequences. It takes only few hours and is highly sensitive. Specifically, qPCR is used to detect, characterize, and quantify the nucleic acids for different applications. In

qPCR, fluorescence is measured during each cycle and fluorescent signal increases proportionally to the amount of replicated DNA in the samples in real time. For the qPCR experiments, biotinylated ssDNA was annealed with the reporter strand (sequence: Table 6.10 in appendix) at 37 °C for 1h. In a half area, high binding, black, 96-well plate, 35 µL of model protein was incubated overnight at 4 °C. After incubation, wells were washed 3 times with 100 µL TBS and 70 µL blocking buffer per well was added (TBS with 2% BSA). The plate was incubated at RT for 1h. After washing 3 times with 100 µL TBS, 35 µL annealed product (biotinylated DNA with reporter strand) was added to each well and incubated for 1h at RT. After six washing steps, binding complexes of biotinylated ssDNA with streptavidin were denatured and reporter strands were eluted from the wells by adding 35 µL of restrictase-free (RF) water and incubating a 96-well plate at 90 °C for 5 min. Then, 20 µL of eluate have been immediately taken out from each well and transferred into 200 µL PCR tubes. qPCR reactions were prepared using SsoAdvanced Universal SYBR® Green Supermix (BioRAD) in 10 µL final reaction volume. Individual reactions contained: 1.5 µL of RF water, 5 µL of 2x SsoAdvanced Universal SYBR® Green Supermix, 0.5 µL of 10 µM primers' solution and 3 µL of reporter strand's solution recovered from the binding assay plate as described previously. All reactions were prepared on ice in Hard-Shell 96-well Low-Profile, Semi-Skirted PCR Plates (BioRAD). SYBR Green fluorescence intensity values were recorded as a function of qPCR cycle number using CFX96 Touch (BioRAD) real-time PCR detection system. The following thermocycler program has been used: Polymerase activation, initial DNA denaturation, i) 30 sec, 95°C; 35 cycles {Denaturation – 10sec, 95°C; Annealing, extension + plate read, ii) 20 sec, 61°C}; melt curve, iii) 65-95 °C, 0.5 °C increment, 2-5 sec/step. Retrieved Cq values (average of 3 measurements) were interpolated within the corresponding, previously constructed calibration curve to determine the amount of reporter strand retained in the well (Figure 3.4). The adsorbed protein on a 96-well plate surface using qPCR technique was consistent with the previous result obtained by fluorescence-based assay, which also shows that the full monolayer immobilization of proteins occurring at 50 nM of the protein (Figure 3.5). 50 nM protein concentration was taken as 100% coverage on the surface to be used for affinity assays (Chapter 4).

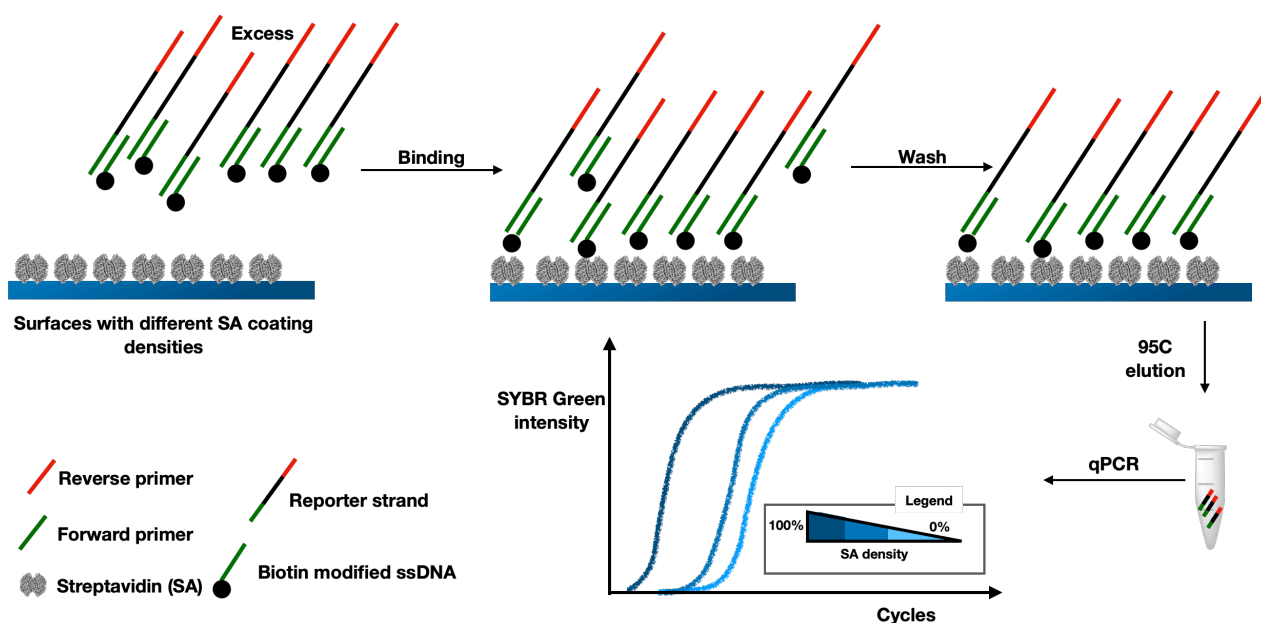


Figure 3.4. Schematic representation of the qPCR surface characterization experiment. Annealed complex (reporter strand and biotin modified ssDNA) was incubated on SA coated surfaces, washed, denatured, and eluted prior to qPCR.

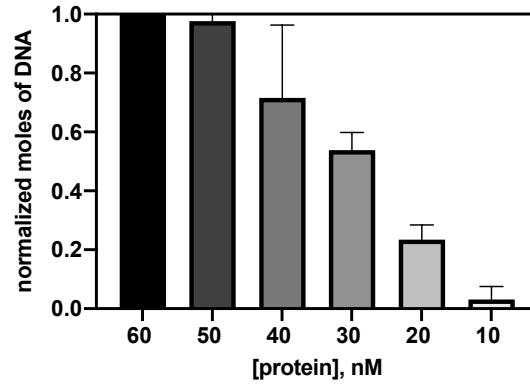


Figure 3.5. Quantification of adsorbed protein in the 96-well plate by qPCR measurements. Error bars represent \pm SD ($n=3$).

3.3 Simulations and Calculations of the Surface Distribution

Receptor surfaces in nature are inherently random as a result of the liquid-order state of the cellular membrane. However, significant changes in local densities of receptors are known to occur as part of disease processes¹⁰⁸ and signaling in for instance the immune synapse¹⁰⁹. Local high concentrations can temporarily be locked in place through changes in surrounding lipid dynamics¹¹⁰. As in the case for super-selective multivalent binding, we expect the density of surface receptors to be of critical importance in pattern-based multivalency. The density is inversely related to the distance between receptors: the higher the density, the smaller the inter-receptor distance. In the ideal multivalent pattern recognition (MPR) case, the “perfect” surface would be one where the spacing of the ligand (x) matches the distance between the receptors (y), and all receptors are placed on a lattice with integer spacing $x=y$. More realistically, however, receptors are distributed randomly and their distribution fluctuates around an average spacing value. To model the average distribution of the receptors, we developed a mathematical model, serving as an experimental preparation guideline which will be explained in the next section.

The deposition of streptavidin on solid surfaces was modeled following the rules of Random Sequential Adsorption of disks^{111,112}. All the following pseudo algorithms were implemented using MATLAB software.

3.3.1 Surface Preparation

It should be noted that the percentages reported do not refer directly to the amount of area covered but rather to the fraction of the maximum amount of area that can be covered. In our case the latter, called in the following jamming limit, should be around 54.7% of the area available¹¹³. 50 simulations for each coverage density ranging from 2% to 120% with an increase of 2% per simulation were performed. With simulation we mean deposition of 16000 receptors represented as disks of normalized diameter on a circular area having a radius that would ensure the desired coverage density once all particles are deposited:

$$R = \sqrt{\frac{N_p}{\rho \delta}} \quad \text{Equation 3.1}$$

Where R is the radius of the deposition area, N_p is the number of particles, δ is the jamming limit and p is the fraction of jamming limit attempted. The system of reference for the deposition was centered in the center of the area to cover and the positions of the receptors to deposit were generated randomly following a uniform circular distribution. The receptors were assigned an ID corresponding to the order of extraction and their positions stored in a list. If overlapping occurred, the involved receptor with the lowest ID number was kept. This cycle was repeated until the 16000th particle was deposited or the maximum number of attempts for insertion of a particle were reached. The maximum number of attempts was set to 10^6 , which was met only when we attempted the surface densities of 100-120%. At attempted densities we never reached precisely the 100% coverage with the disks successfully inserted (Figure 3.6).

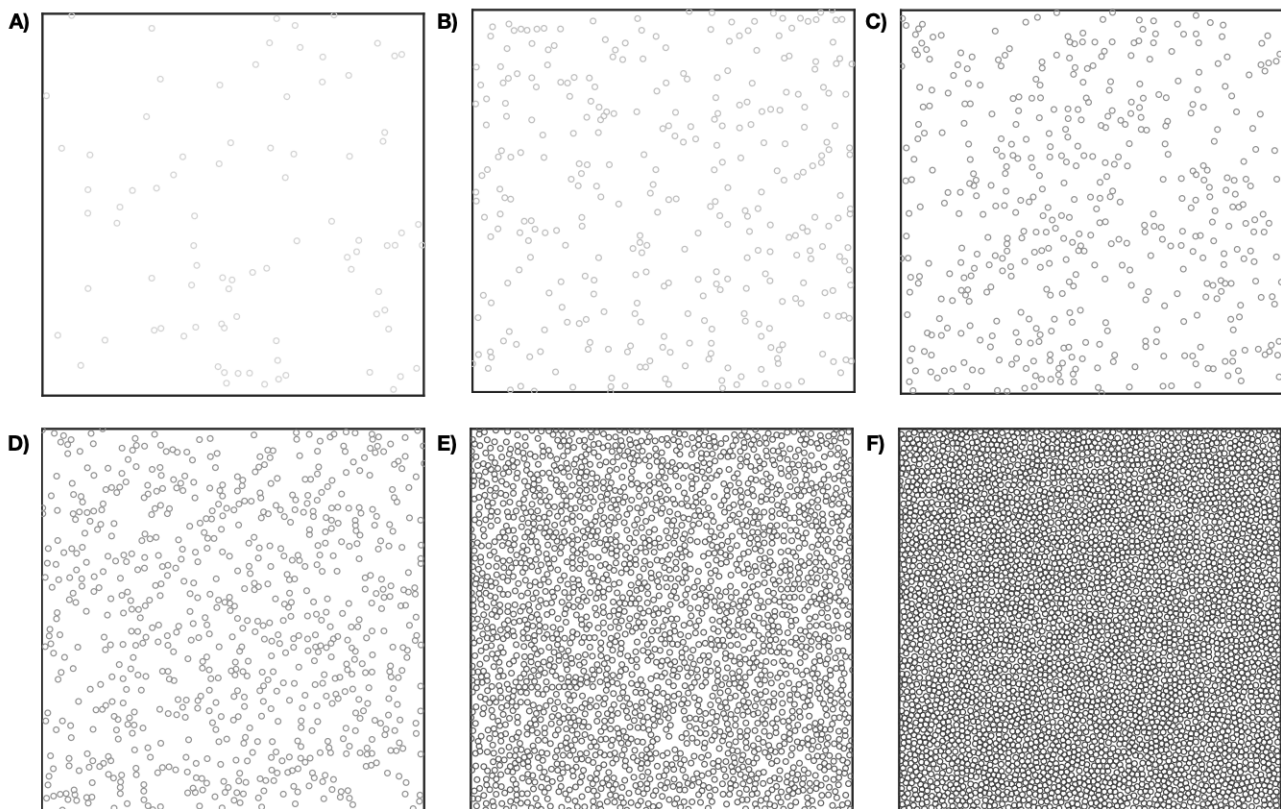


Figure 3.6. Matlab images of surfaces with different densities (in %) A) 2 %, B) 7 %, C) 11 %, D) 16 %, E) 56 %, F) 100 %. The squares are taken from the center of the whole surface for all images.

3.3.2 Determining Neighbors and Their Distances

In order to avoid the artifacts due to proximity of the boundaries of the simulated surfaces, we analyzed the particles contained in the circle of radius $0.875 R$, a list containing its neighbors was prepared. We looked for the neighbors of each particle in an iterative matter. For the i^{th} disk, we set a new system of reference centered at its absolute coordinates and all the other particles coordinates were transformed accordingly. We set a maximum possible distance M , in normalized units, that a neighbor could have to reduce the search space. Based on the void distributions¹¹¹ esteemed at low surfaces, we decide M to be equal to 30.

Using this reference value, we employed the following pseudo algorithm for the i^{th} particle:

1. If some particles proved already to have i^{th} has neighbor, store them in a list of "neighbors";
2. Check the receptors contained in the circle centered in the origin and radius M . If their ID is greater than i^{th} store them in a list of "possible neighbors".

3. For each element of “possible neighbors” verify that no other element of the same list is contained inside the circle having as diameter the distance between the element and the origin. If the statement is verified add them to “neighbors”.
4. If a neighbor is at a distance over the limit $M/2$, increase M of two folds and repeat from point 1 (condition met only for 7% and 2%).

After the lists of neighbors was completed, the relative cumulative distribution function (CDF) of neighbors encountered before a given distance χ was computed for every sampled surface and then averaged. We then fitted the obtained curves with Gamma distribution, collected the resulting modes and prepared a master curve, reporting what would be the most common distance between neighbors at given receptor density. The equation used for fitting of the master curve was:

$$r = d \left(\frac{2v^3 - 6v^2 - \sqrt{2v^2(1-v)(2-v)^3 + 4v}}{(2-v)^2} + c \right) \quad \text{Equation 3.2}$$

Where r is the most common distance, d is the diameter of streptavidin, set around 5.64 nm, v is the fraction of unoccupied area ($1 - \delta\rho$) and C is a fitted parameter, when $c = 1.139$ is, the resulting R^2 using only even surfaces coverages as reference is 0.9461.

New replicas were performed for the target surfaces, matching the spatial tolerance of the particles, we decided to apply in our experiments e.g., 2%, 7%, 11%, 16%, 56% and 100% (for justification, see next section). Via simulation of the receptor distribution on the surface at a given density, we obtained a master curve of the inter-receptor spacing (Figure 3.7) which serves as the experimental preparation guidelines to allow for multivalent pattern recognition. Figure 3.7 shows every bivalent structure and hexavalent DNA-origami disk has its own corresponding density to bind to: long rigid bivalent (LB): 11 %, short rigid bivalent (SB): 16 %, large hexagon (LH) pattern: 7 %, and short hexagon (SH) pattern: 56 %. The flexible structures are expected to interact with a range of densities, e.g. 6-18 nm for the bivalent and 4-11 nm for the hexavalent flexible analytes.

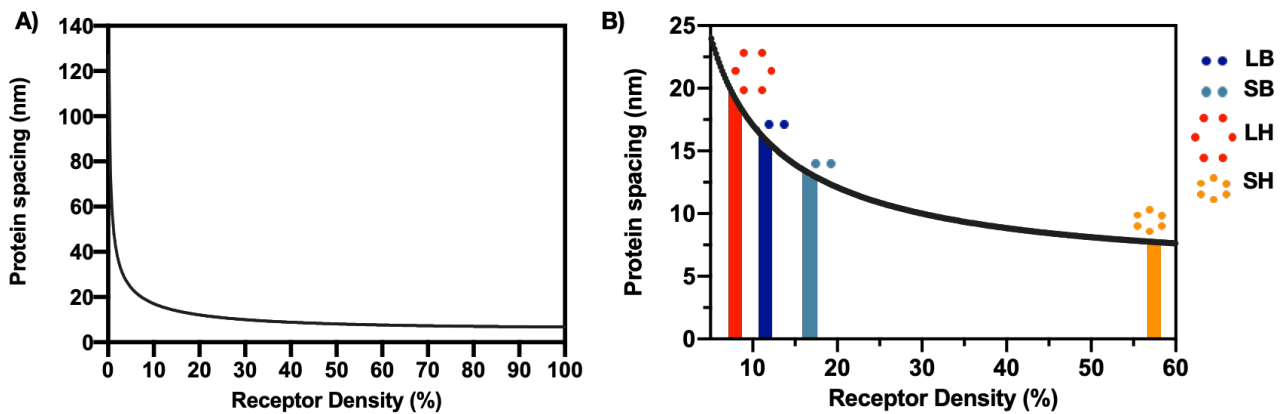


Figure 3.7. A) Theorized spacing between the receptors in function of receptor density in % of protein, revealing that each nanoparticle has its own hot spot to bind to. B) Zoom-in of plot A, showing the range between 0-60% receptor density.

Figure 3.8 shows that the probability distribution of the proteins on the surface in function of average spacing, (in nm) for different surface densities from full immobilization (100%) to very scarce surface (2%). As seen from the following plots, as the receptor density decreases, the calculated inter-receptor probability distributions widen. In other words, the probability of having the controlled average spacing of the proteins for denser surfaces is higher compared to lower surface densities. This will likely impact the onset accuracy of pattern-based multivalency.

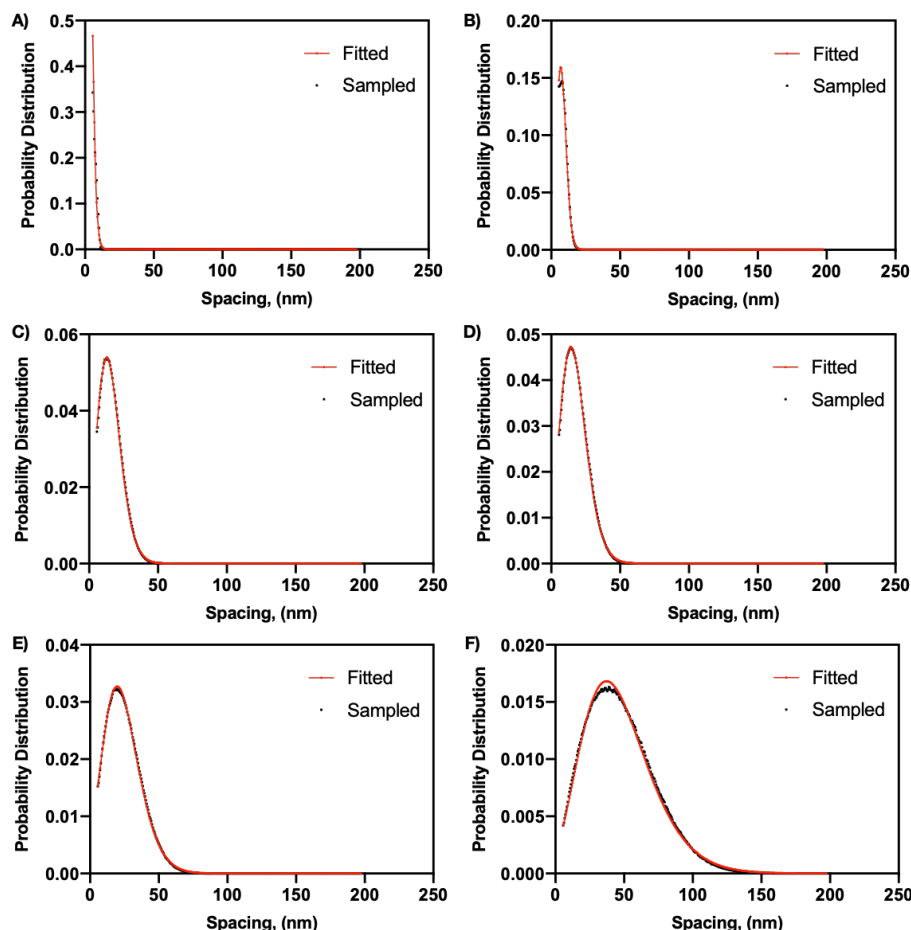


Figure 3.8. Probability distribution of proteins (receptor) in function of spacing for different surface densities (in %). A) 100%, B) 56%, C) 16%, D) 11%, E) 7%, F) 2%. As the density of receptors on the surface decreases, the probability function becomes wider. R^2 values are 0.996, 0.999, 0.999, 0.999, 0.999, 0.999 for 100%, 56%, 16%, 11%, 7%, and 2% respectively.

In Figure 3.9 we present how each bivalent particle may interact with the protein on the surface at different receptor densities (from left to right, LB, SB, FB). When the particles are exposed to the receptors on the surface, they can either bind monovalently or bivalently. If the end-to-end distance of the particles matches the spacing of the receptors on the surface, they will bind bivalently. For example, if the surface is relatively sparse (<11% receptor density), we expect all the particles to bind monovalently, however, on denser surfaces (e.g., 100% receptor density) they are expected to bind bivalently. For instance, SB can only bind monovalently on 11% surface coverage, because the end-to-end distance of the ligands is smaller than the spacing of the receptors. Whereas as we increase the receptor density, the end-to-end distance of the particle has higher probability to match the receptor spacing and more likely to bind bivalently as seen on denser surfaces (e.g., 16% or 100% surface coverages). Compared to the SB, LB can bind bivalently at 11% receptor density, given that its probability of matching the end-to-end distance to the receptor spacing is higher. On the other hand, since the flexible design can be found in three different conformations, its end-to-end distance is changing; therefore, we expect it to bind bivalently on all three receptor densities (11 %, 16 %, and 100 %).

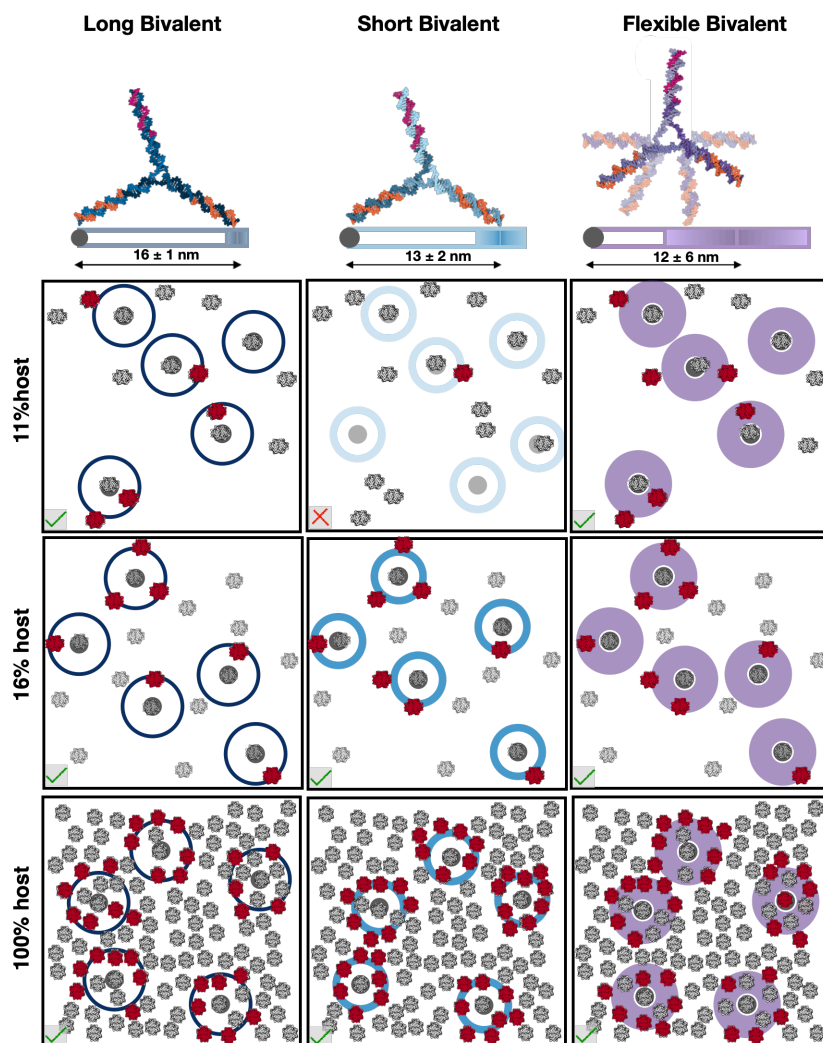


Figure 3.9. Schematic representations of possible interactions between bivalent structures and increasing surface receptor densities (in %). When the end-to-end distances of the particles matches the target receptor's spacing, bivalent binding occurs. In red are receptors that fall within binding range of the bivalent analyte (highlighted by a circle) after a first binding event has taken place (in centre of circle in grey). Red crosses and green checks are used when there is no binding and binding respectively. Pale tripods represent non-bound analytes.

In Figure 3.10 we present how each hexavalent particle interacts with the protein on the surface at different receptor densities (from left to right, LH, SH, FH). When the particles are exposed to the receptors on the surface, we expect the particles bind when their spatial tolerance of the ligands matches the target spacing. For example, when the surface is very sparse (e.g. 7%), we expect only large hexagon to bind since the target spacing is within its spatial tolerance. However, on denser surfaces (e.g. 56%), all the particles are expected to bind. The rigid small hexagon's ideal surface is 56%, corresponding to receptor spacing of 8 nm, which perfectly matches the spatial tolerance of the small rigid particle. Additionally, since flexible hexagon has an estimated spatial uncertainty of ~ 3.5 nm compared to its rigid analog (small hexagon), it is expected to bind at lower density (24%) compared to SH.

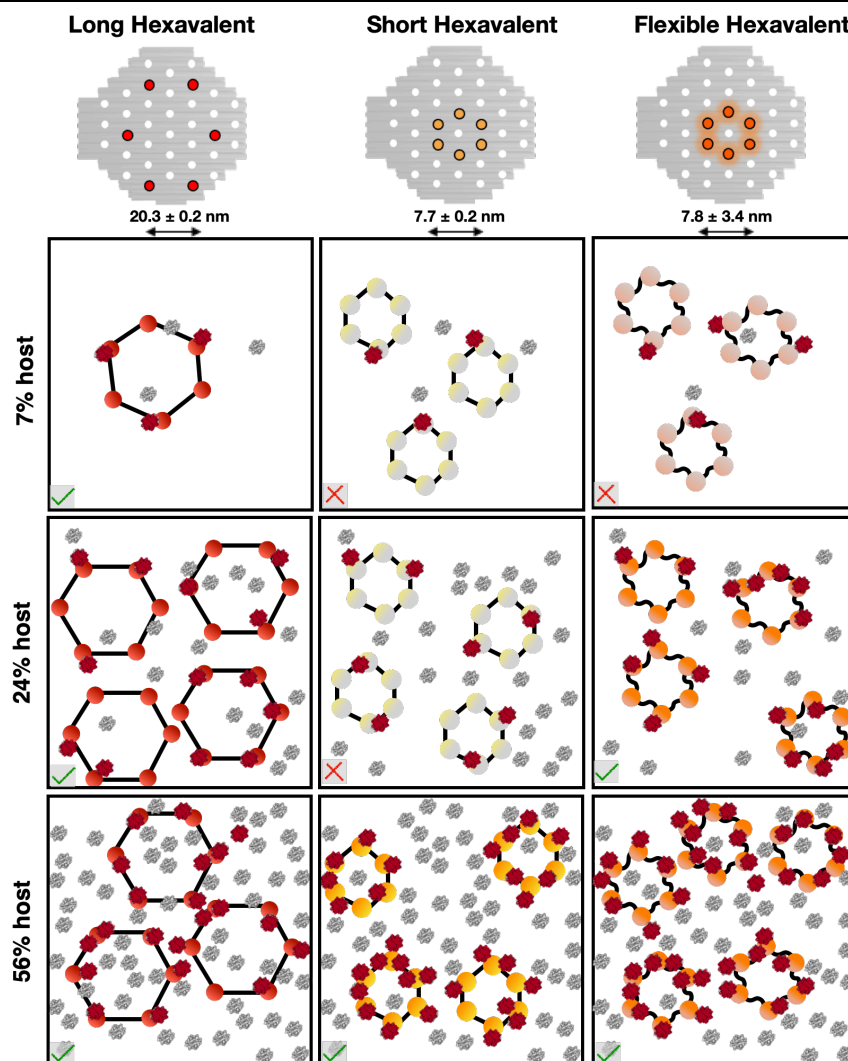


Figure 3.10. Schematic representations of possible interactions between hexavalent structures with increasing receptor densities (in %). When spatial tolerance of the particles matches the spatial organization of the receptors on the surface, particles bind to receptors on the surface. The receptors in red fall within the spatial tolerance of hexavalent analytes (highlighted by a hexagon). Red crosses and green checks are used when there is no binding and binding respectively. Pale hexagons represent non-bound analytes.

We next used the theoretical receptor densities to generate experimental test surfaces to analyze multivalent binding. A density series of protein surfaces between 2-100% (e.g. a receptor spacing of 38 and 7 nm respectively) was obtained using decreasing concentrations of protein in the immobilization protocol and confirmed by solid-phase binding assay (Figure 3.11). From these surface gradients, we selected the densities selective for our bivalent and hexavalent constructs and prepared a set of reference surfaces to use in our multivalent spatial tolerance assays.

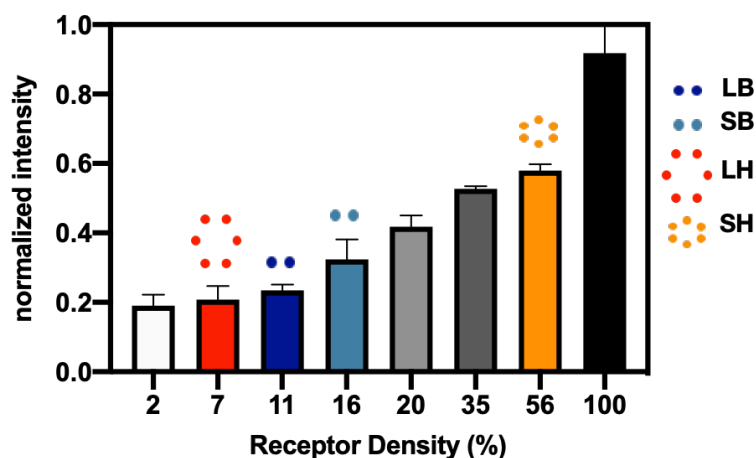


Figure 3.11. Solid-phase binding assay of biotinylated ssDNA-functionalized with dye (Cy5) on protein-coated polystyrene surfaces (from very scarce, 2 %, to very dense 100 %) with different densities. Error bars represent \pm SD (n=3).

3.4 Conclusion

In this chapter, we focused on the calculation, assembly, and characterization of protein-coated surfaces with increasing densities. First, the purity of both receptors, SA and ST, was shown with PAGE gel electrophoresis. Protein coated surfaces were characterized with two different techniques: solid-phase assay and qPCR surface analysis confirmed the concentration needed to form a monolayer protein receptor to be 50 nM within the experimental conditions used. Then, the deposition of streptavidin on solid surfaces was modeled to calculate the average distribution of receptors and inter-receptor probability distributions. It was shown that every rigid bivalent and hexavalent scaffolds has its own hotspot receptor density that matches the spatial tolerance of the scaffold: LB: 11%, SB: 16%, LH: 7%, and SH: 56%. With the design and characterization of target surfaces complete, we need to shift focus to select the ligand that is presented multivalently to study super-selectivity, and the impact of spatially controlled patterns on multivalent binding, which will be explained in the next chapter.

Chapter 4 Multivalent Pattern Recognition in DNA Nanomaterials

Multivalency, strength in numbers, is an omnipresent phenomenon to enhance a ligand-receptor interaction potential. Natural multivalent interactions allow for cellular communication and regulation of signaling pathways³ as discussed in chapter 1 and synthetic multivalent interactions have been studied in great depth and models of multivalent binding exist for both solution and surface-based interactions^{114,115,116,117}. However, these materials are built on one of two (or both) assumptions: i) either the ligand or receptor is present at high excess, and/or (2) the system is dynamic and allows for the reorganization of ligands or receptors in space to facilitate the interaction, which comes with an entropic penalty upon binding¹¹⁴. In nature, however, the numbers of ligands and receptors are often low to moderate and their position in space quasi-controlled¹⁸ e.g. interaction between antibodies and antigens¹⁶. Recent insights in spatial tolerance of various classes of antibodies show a distinct relation between flexibility and function^{118,119,120}. IgM engages dynamically with antigen patterns on pathogens that display a wide range of spatial organization, hence the spatial tolerance and flexibility of IgM are exceptional, ranging from 3-29 nm. Contrary, the more rigid IgG displays a low spatial tolerance and forces a match between ligand and receptor spacing, allowing for a stepwise binding behavior¹¹⁸. Ligand patterns that show spatial organization are typically found in foreign pathogens (viruses) or intracellularly in signaling and organization¹²¹ and our immune system is highly developed to recognize such patterns¹²². Cells are able to control their local density of receptors through various dynamic mechanisms¹¹⁰, hence seem to utilize a super-selective multivalent binding mechanism in the low-valency regime. Rigidity in this regime could thus be an interesting parameter to explore in the context of super-selectivity. Presentation of ligands in low spatial-tolerant patterns is possible when the material backbone is rigid and allows for precise control in space. Currently, no clear analysis exists on this middle regime, where we observe a limited spatial tolerance in both the ligand and receptor presentation. DNA-nanotechnology⁵⁷ poses itself as the ideal engineering platform as self-assembly is directly linked to base-pairing and rigidity related to sequence length as well as single or double-stranded assemblies as discussed in chapter 1. Using precise control of spatial tolerance in low-valency ligand-presenting DNA nanomaterials and combination with biophysical analysis of binding, we set out to explore the influence of valency and spatial tolerance in multivalent binding.

In this chapter, we show a form of super-selective binding, where the selectivity is controlled by the rigidity and ligand patterns. We call this multivalent-pattern recognition, MPR, this can be achieved when the difference in affinity between monomeric and multimeric interactions is sufficiently large and the spacing between ligands is homogeneous and tightly controlled in space. We describe the selection of ligands, their synthesis and assembly with the designed particles discussed in chapter 2. In order to study the super-selectivity profiles of the particles, affinity analysis by SPR and solid phase was performed first to measure the concentration range for spatial tolerance experiments, as these

should be above the K_D . Finally, spatial tolerance experiments were performed on a solid-phase assay. Fitting of the experiments were performed by Vincenzo Caroprese and SPR measurements were performed by Kaltrina Paloja.

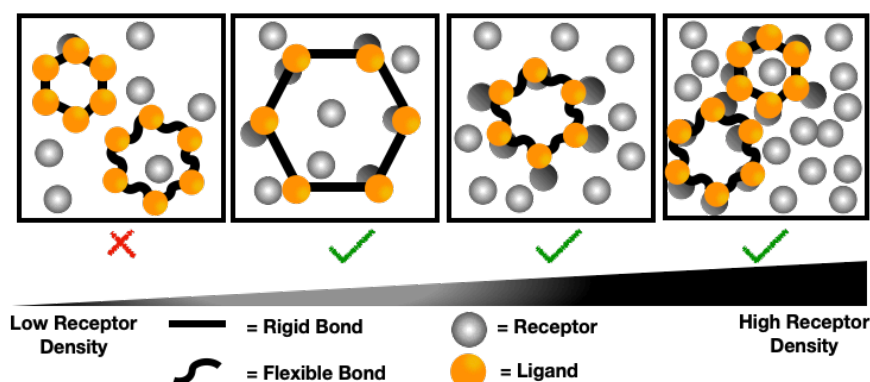


Figure 4.1. Schematic representation of the effect of rigidity and spacing on selective multivalent-pattern recognition (MPR). When spatial tolerance of particles does not match the spatial organization of the surface, binding does not occur (panel 1). Only large hexagon (LH) is expected to show an interaction onset at low receptor density (panel 2). As flexible hexagon (FH) shows higher spatial tolerance compared to rigid small hexagon (SH), FH is expected to bind at lower receptor density (panel 3) compared to SH (panel 4).

Part of this chapter is in preparation for submission: “Multivalent Pattern Recognition Through Engineering of Spatial Tolerance in DNA-Based Nanomaterials”; Hale Bila, Kaltrina Paloja, Vincenzo Caroprese, Artem Kononenko, Maartje M.C. Bastings.

4.1 Streptavidin Binding Peptides

For multivalent binding to be sensitive to valency and spatial patterns, the monovalent interaction between the ligand and receptor cannot be too strong, as this would forgo the need for multivalent presentation¹⁸. Additionally, the difference between monovalent, bivalent, and multivalent presentation should be significantly large, to allow for discrimination between the respective arrays. This scenario is present in the case of a moderately fast dissociation rate constant, as a fast dissociation favors multivalent presentation since monovalent interactions will not be stable. With these requirements, we started screening different streptavidin and streptactin binding peptide options in literature.

Different methods have been developed to screen peptide or protein libraries for specific binders such as phage display¹²³, cell surface display¹²⁴, plasmid display¹²⁵, ribosome display¹²⁶. In addition to biotin, various peptide motifs bind to streptavidin with lower affinity than biotin ($K_a=10^3-10^8 \text{ M}^{-1}$)^{127,128,129}. These streptavidin binding peptides have been used for different applications such as purification and detection of proteins¹³⁰. The well-defined peptides binding to streptavidin in biotechnology are Strep-tag (sequence: Ala-Trp-Arg-His-Pro-Gln-Phe-Gly-Gly)¹³¹ and Strep-tag II (sequence: Trp-Ser-His-Pro-Gln-Phe-Glu-Lys)¹⁰³, nine and eight amino acid long peptides including His-Pro-Gln (HPQ) sequence, which have different affinity constants depending on the sequence. They are bound at the same pocket as biotin. Strep-tag peptide has a limited interaction between streptavidin, with a $K_d = 37 \text{ } \mu\text{M}$ determined for the complex¹⁰³, however, Strep-tag II (STII) shows increased affinity to engineered recombinant streptavidin, Strep-tactin¹⁰². Thermodynamic analysis of binding isotherms results in $K_d \sim 1 \text{ } \mu\text{M}$, whereas Strep-tag II has a weak interaction with SA

($K_d = 72 \mu\text{M}$)¹⁰³. Advantages of Strep tag II is that it does not interfere with the biological activity of the target protein. Wide variety of streptavidin-derivatized materials (plates, beads, fluorophores etc) are commercially available and Strep-tag II peptide can be selectively eluted from SA by the addition of biotin.

Previously, Bastings *et. al.* presented phage peptides on a multivalent platform to restore the binding affinity partially¹³². They studied the effects of valency, linker choice, and receptor density in binding affinity of a multivalent structure by using SLLAHPQGGG peptide towards streptavidin. SPR measurements showed that they increased the binding affinity by two orders of magnitude with two peptides (K_d of $7 \mu\text{M}$) and five peptides (K_d of $1 \mu\text{M}$) over the monovalent species (K_d of $120 \mu\text{M}$). Many peptide ligands that contain the common motif HPQ in their sequence generally show low affinities. Giebel *et. al.* demonstrated that higher binding affinities can be achieved by using cyclic peptides. They increased the affinities up to 3 orders of magnitude compared to linear peptides and explained it by conformational freedom of linear peptides and having more ordered structured with cyclic peptides. SPR measurements resulted in $K_d = 660 \text{ nM}$ ¹²⁸.

Other SA-binding peptides, lacking the HPQ motif, have been isolated from ribosome display. 32% of the sequence clones containing DVEAW or DVXXW motif, in which DVEAWLDER sequence shows stronger binding activity and binding affinities of different variants of this specific sequence were measured by SPR (Figure 4.2), showing K_d values ranging from 3 nM to 600 nM¹³⁰. These variants of this peptide has been used as affinity tags for the purification and detection of recombinant proteins¹²⁹.

Peptide	Structure	K_d (nM)
Wt	DVEAWLDERVPLVET	3.6 ± 0.6
C-6	DVEAWLDER	240 ± 40
C-6 3Asp	DVDAWLDER	940 ± 140
C-6 3Gly	DVGAWLDER	570 ± 90
C-6 6Phe	DVEAWFDER	Not detectable
C-6 6Arg	DVEAWRDER	Not detectable
C-6 7Gly	DVEAWLGER	17 ± 4
C-6 8Ala	DVEAWLDAR	160 ± 30
C-6 7G8A	DVEAWLGAR	17 ± 4
wt 7Gly	DVEAWLGERVPLVET	4.2 ± 0.7
wt 7G8A	DVEAWLGARVPLVET	4.1 ± 0.6

Figure 4.2. The dissociation constants of different variants of DVEAWLDER peptide sequence¹³⁰.

SBP-tag is another SA binding peptide which has been used for the purification of proteins from complex mixtures by using small amounts of immobilized streptavidin. The analysis resulted in K_d of 2.5 nM for the interaction of the SBP-tag sequence with SA¹³³. Although this peptide has a very high affinity to SA, it is not an ideal tag because it is 38 amino acids long and consequently rather big for an affinity peptide. Other SA-binding peptides, lacking HPQ sequence, PWPWLG, GDWVFI motifs¹³⁴ and EPDW motifs¹³⁵ have been also identified and by phage display method.

Recently, Patel's group showed the combination of peptide array library design, parallel screening, and stepwise evolution to discover novel peptide hotspots to a protein target. They synthesized linear and cyclic peptides, and peptides composed of natural and non-natural amino acids. LAEYH, PAWAH, FDEWL were selected as representative clusters and SPR measurements showed that the EWVHPQFEQKAK peptide and Strep-tag II HPQ peptides (used as a control) showed fast on/off rates with K_d values of $5.7 \mu\text{M}$ and $49.8 \mu\text{M}$ respectively. The AFPDYLAEYHGG peptide showed the lowest K_d value, 43 nM among the other peptides with a slower off rate ($k_{\text{off}} = 1.3 \times 10^{-3} \text{ s}^{-1}$)¹³⁶.

After evaluating different peptide options, we decided to use SLLAHPQGGGC and its scrambled control, SALQLPHGGGC and Streptag II peptides as ligands, and compare selectivity profiles of functionalized DNA-nanomaterials with these peptides on different surface densities.

4.2 Methods and Materials

All the amino acids and rink amide resin were purchased from Lipopharm (Poland). o-benzotriazole-N,N,N'-tetra-methyluronium hexafluoro-phosphate (HBTU), N-methylpyrrolidone (NMP), glycine, sodium acetate, and diisopropylethylamine (DIPEA) were purchased from ABCR GmbH (Germany). Dichloromethane (DCM), triisopropylsilane (TIS), trifluoroacetic acid (TFA), diethyl ether, bovine serum albumin (BSA), piperidine and triethylamine (TEA), HPLC grade, dibenzocyclooctyne-maleimide (DBCO), CF488A-maleimide were purchased from Sigma-Aldrich (St. Louis, Missouri, USA). 1,2-Ethanedithiol (EDT) was purchased from Alfa Aesar, (Haverhill, Massachusetts, USA). Acetonitrile (ACN), HPLC grade, was purchased from Chemie Brunschwig AG (Switzerland). All the oligonucleotides (ODNs) were purchased from Integrated DNA Technologies (Coralville, Iowa, USA). Scaffold type p7560 was obtained from Tilibit (cat: M1-30). Ladder 1kB (N3232L) was purchased from Biolabs. Potassium chloride (cat: 6781.1) and agarose (cat: 3810.2) were purchased from Carl Roth. Gel loading dye (cat: B7024S) was purchased from New England Biolabs. Novex™ 10% Tris-Glycine gels, NuPAGE LDS buffer, DNA gel loading dye, DNA ladder (50 bp), Sybr Gold were purchased from Invitrogen (California, USA). Tris Borate EDTA buffer was purchased from Fisher Scientific (Waltham, Massachusetts, USA). Tris-hydrochloride was purchased from Apollo Scientific (United Kingdom). Tetramethylethylenediamine (TEMED) was purchased from AppliChem GmbH (Germany). Acetic acid (glacial) was purchased from Merck (Germany). Ammonium persulfate (APS) was purchased from VWR (Pennsylvania, USA). Acrylamide and bis-acrylamide solutions were purchased from Biorad (Hercules, California, USA). Anti-Streptavidin, DyLight 488 (VC-SP-4488-MC05) was purchased from Vector Laboratories. 10x PBS buffer (pH= 7.4) was purchased from Gibco. Zeba™ spin desalting columns, 7K MWCO, immobilized TCEP disulfide reducing gel, and Pierce™ spin cups-paper filter (cat:69700), Tris 1 M, pH 8.0 (cat: AM9855G), EDTA 0.5 M, pH 8.0 (cat: AM9260G), and SYBR Safe (cat: S33102), Pierce™ Quantitative Fluorometric Peptide Assay (cat: 23290), Micro BCA™ Protein Assay Kit (cat: 23235) were purchased from Thermo Fisher Scientific. Strep-tactin protein (cat: 2-1204-001) was purchased from IBA GmbH. CM3 chips were purchased from Cytiva Life Sciences. Amicon Ultra-0.5 mL centrifugal filters were purchased from MerckMillipore. Unless otherwise stated, all chemical and biological reagents were used as received.

4.3 Instruments

Electrospray ionization mass spectra (ESI-MS) were acquired on LTQ Orbitrap ELITE ETD (Thermo Fisher Scientific). Characterization of peptides and purification and characterization of DNA-peptide conjugates were performed by a Thermo Scientific Dionex Ultimate 3000 U-HPLC system equipped with Hypersil Gold™ C18, 150x4 mm column with a particle diameter of 3 µm. Purification of peptides was performed by a Thermo Scientific Dionex Ultimate 3000 U-HPLC system equipped with a standard pressure pump module, variable wavelength detector and automated fraction collector using 8 mL tubes. A C18 Hypersil Gold™, 250x21.2 mm column with a particle diameter of 5 µm. HERMLE Z366 HK centrifuge

was used for centrifugations. Polyacrylamide (PAGE) gel electrophoresis was performed in a Biometra eco-mini gel tank (Analytic Jena) and the images of the gels were taken by Bio-Rad ChemiDoc MP imaging system (Hercules, California, USA) using the appropriate background plates (blue or black). Cy5 fluorescence was imaged using the present Cy5 filters and sequentially SYBR gold was imaged to generate the dual-labeled images. Post imaging analysis was performed using the Bio-Rad ImageLab software (freeware). The fluorescence intensity of samples was measured with BioTek™ Cytation 5™ Fluorescence, Endpoint Read Mode Biotek Instruments, Inc. using Gen5 software, Version 3.03 (Winooski, Vermont, USA). Concentration analysis of ssDNA and dsDNA strands was performed using ssDNA and dsDNA set up on a Quawell Q9000 nanodrop spectrometer. Samples were annealed by using Biometra trio thermocycler (Analytical Jena). Surface Plasmon Resonance (SPR) experiments were performed on Biacore 8K, using CM3 Cytiva chips. qPCR experiments were performed on CFX96 Touch (BioRAD) real-time PCR detection system.

4.4 Buffers

The following buffers were used for the sample preparation. Buffer A: Tripods annealing buffer: 5 mM Tris, 1 mM EDTA, 150 mM NaCl and 10 mM MgCl₂. Buffer B: DNA-origami disk annealing buffer: (1×): 5 mM Tris, 1 mM EDTA, 5 mM NaCl, 18 mM MgCl₂, pH = 8.0. Buffer C: SPR immobilization of protein buffer: 10 mM HEPES, 150 mM NaCl. Buffer D: SPR regeneration buffer for DNA-origami disks: 10 mM HEPES, 50 mM NaCl. Buffer E: SPR regeneration buffer for antibody: 10 mM glycine pH = 1.5.

4.5 Streptavidin – SLLAHPQ System

Streptavidin binding motif, HPQ, in the monovalent form weakly binds to SA with a K_D of 50–150 μ M, depending on the the exact sequence¹³⁷. In this thesis, HPQ is presented on DNA nanoparticles bivalently and hexavalently to compare their binding affinities and selectivity profiles.

4.5.1 Peptide Synthesis

Peptides can be synthesized through solid state methods described by Merrifield, in which N-terminus protected amino acids are sequentially added on to a growing peptide chain whose C-terminus is covalently attached to a solid state support resin¹³⁸. Then, the deactivated N-terminal amino group of the peptide chain reacts with an excess of an activated ester of the next amino acid, which forms an amide bond between the amino group of the last amino acid on the resin and the carboxylic acid group of the subsequent amino acid. Each amino acid has their N-terminus protected by a labile group (either Fmoc- or Boc-) to prevent self-polymerization. After the last amino acid is added, free N terminus is deprotected. In the case of Fmoc- protecting groups, it is deprotected with mild basic conditions, 20% piperidine in dimethylformamide (DMF). Then, the resin is washed with solvent couple of times to remove excess reagents. After the desired sequence is synthesized, the peptide from the solid support resin is cleaved and the protecting groups of the side groups are removed under acidic conditions.

4.5.1.1 Synthesis of SLLAHPQGGGC peptide

The peptide was synthesized by manual solid phase 9-fluorenylmethoxycarbonyl (Fmoc) chemistry on a Rink-amide resin. Fmoc deprotection was performed by mixing the resin in a 20 vol% piperidine in N-methylpyrrolidone (NMP) solution for 5 minutes, followed by washing the resin with NMP (6 times). For all amino acid couplings, 4.0 eq. (relative to the resin loading) of Fmoc-protected amino acid, 4 eq of o-benzotriazole-N,N,N'-tetramethyluronium hexafluorophosphate (HBTU) in NMP and 16 eq of diisopropylethylamine (DIPEA) in NMP were added to the reaction vessel and mixed for 45 minutes at room temperature, followed by washing with NMP (6 times). After the last coupling, the resin was washed with NMP (6 times) and dichloromethane (DCM) (4 times) and allowed to dry under high vacuum. Peptide cleavage and removal of side chain protecting groups were performed using a cleavage cocktail consisting of 92.5% TFA, 2.5% H₂O, 2.5% TIS, and 2.5% EDT for 4 hours, shaking at room temperature, followed by precipitation of the product in cold di-ethyl ether for 15 minutes. After spinning the precipitate 15 minutes at 20k RPM and re-dissolving in MQ the products were purified by RP-HPLC with a gradient of 10-35% acetonitrile in water in 33 min ESI-MS. m/z Calcd.: 1037.51 Da Obsd. $[M+Na]^+$: 1060.49570 Da $[M+2H]^{2+}$: 519.76150 Da (Figure 4.3).

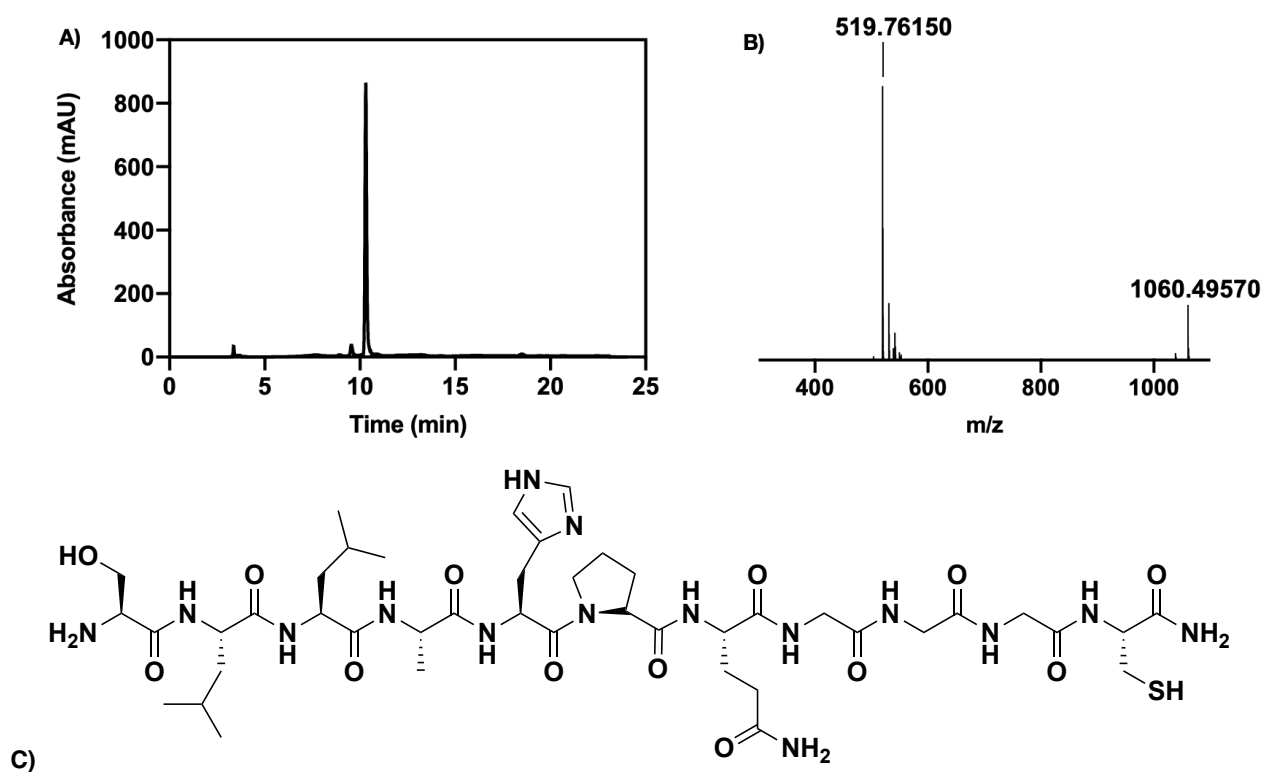


Figure 4.3. A) HPLC trace of pure SLLAHPQGGGC peptide. ESI/MS of SLLAHPQGGGC peptide m/z Calcd.: 1037.51 Da Obsd. $[M+Na]^+$: 1060.49570 Da $[M+2H]^{2+}$: 519.76150 Da. C) Chemical structure of SLLAHPQGGGC peptide.

4.5.1.2 Synthesis of Scrambled peptide - SALQLPHGGGC

Respectively, Fmoc-Cys(Trt)-OH, Fmoc-Gly-OH, Fmoc-His(Trt)-OH, Fmoc-Pro-OH, Fmoc-Leu-OH, Fmoc-Gln(Trt)-OH, Fmoc-Leu-OH, Fmoc-Ala-OH and Fmoc-Ser(tBu)-OH were coupled. The peptide was cleaved with the cleavage cocktail and was purified by RP-HPLC with a gradient of 10-35% acetonitrile in water in 33 min. m/z Calcd.: 1037.51 Da, Obsd. $[M+H]^+$: 1038.51140 Da $[M+2H]^{2+}$: 519.76320 Da (Figure 4.4).

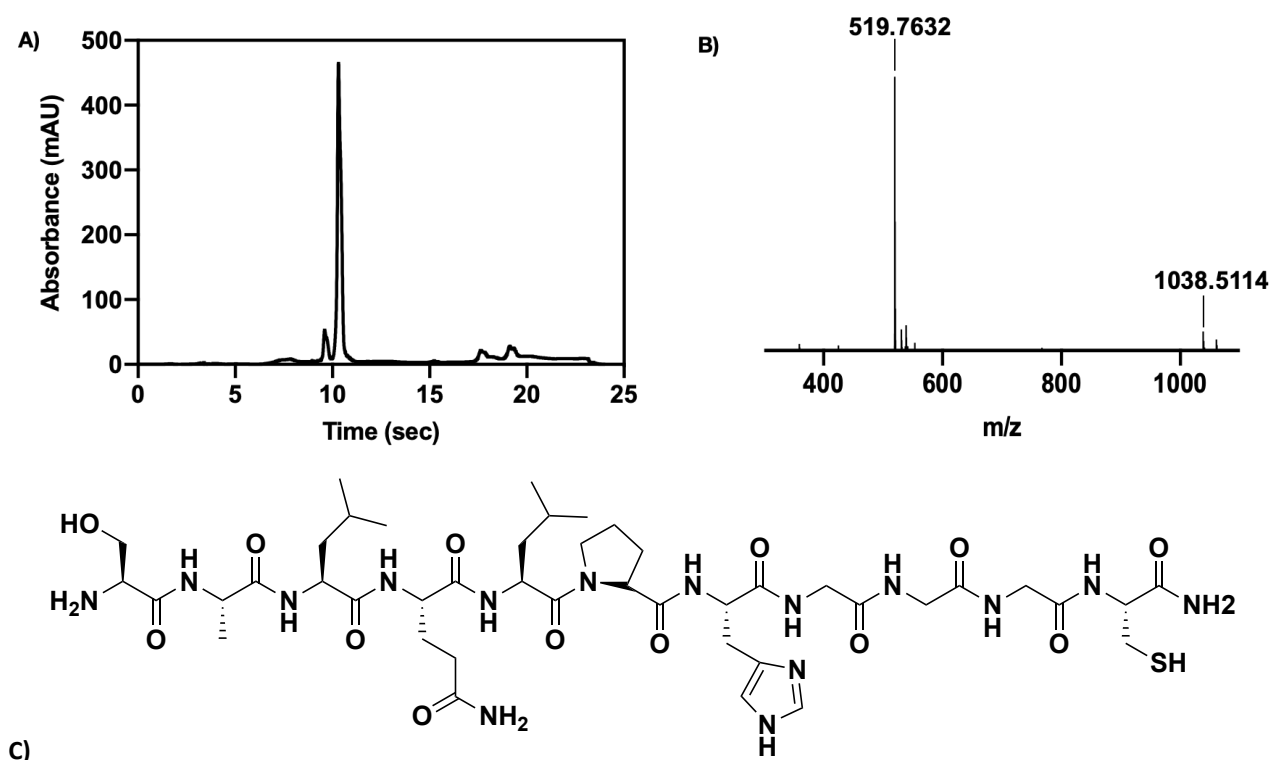
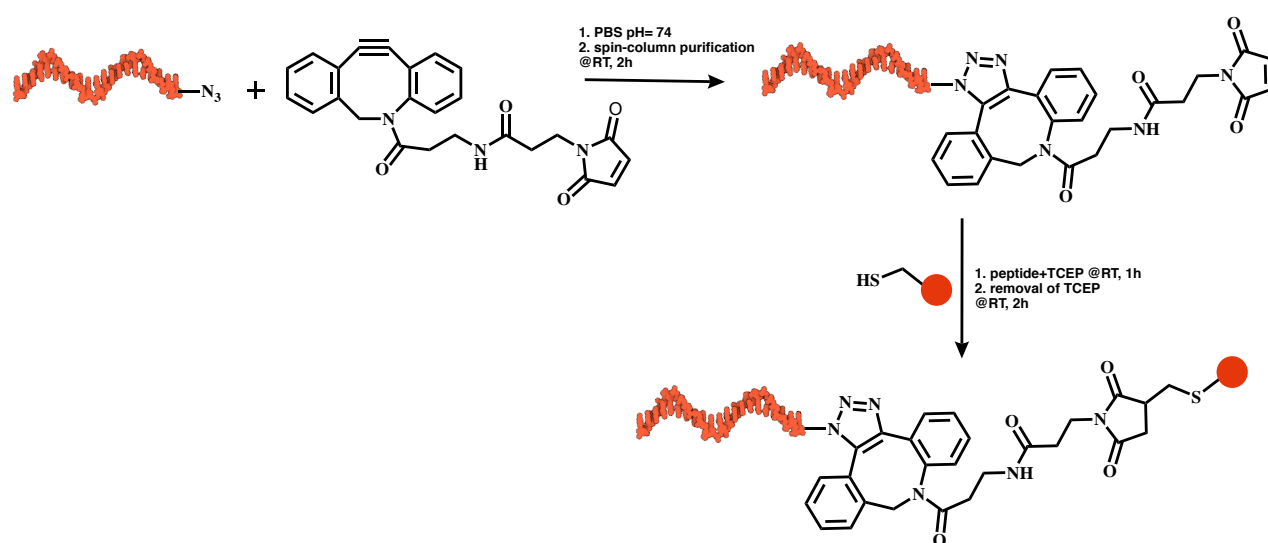


Figure 4.4. A) HPLC trace of SALQLPHGGGC peptide. B) ESI/MS of SALQLPHGGGC peptide. m/z Calcd.: 1037.51 Da Obsd. $[M+H]^+$: 1038.51140 Da $[M+2H]^{2+}$: 519.76320 Da. C) Chemical structure of the scrambled peptide.

4.5.2 Synthesis of ssDNA – peptide conjugate

Azide functionalized ssDNA (GTGATGTAGGTGGTAGAGGAA) was dissolved in PBS (pH=7.4) including 10 mM EDTA to make a stock of 500 μ M, verified by nanodrop analysis. A fresh DBCO-maleimide stock solution (25 mM) was prepared in DMSO and added in 4x excess to the ssDNA solution. The mixture was incubated on a rocking platform at room temperature for 2h. The excess DBCO-maleimide was removed using Zeba™ Spin Desalting Columns, 7K MWCO according to the manufacturer's protocol. Simultaneously, 1mg peptide was dissolved in 100 μ L of MQ to make a 10 mM stock solution. 100 μ L of TCEP reducing gel slurry was added into the peptide solution and the mixture was incubated at room temperature for 1h. The TCEP gel slurry was removed by Pierce™ Spin Cups-Paper Filters by centrifugation once for 1 min at 1500xg. The reduced peptides were added into desalted DBCO coupled ssDNA solution and incubated at room temperature for 2h (Scheme 1). The DNA-peptide conjugates were characterized on a 20% native PAGE gel electrophoresis (Figure 4.5) and with RP-HPLC using a gradient of 15% to 75% TEAA buffer (triethylamine and acetic acid buffer, 100 mM, pH=7): ACN gradient over 24 minutes (Figure 4.6).



Scheme 1. Synthesis scheme of ssDNA-peptide conjugates.

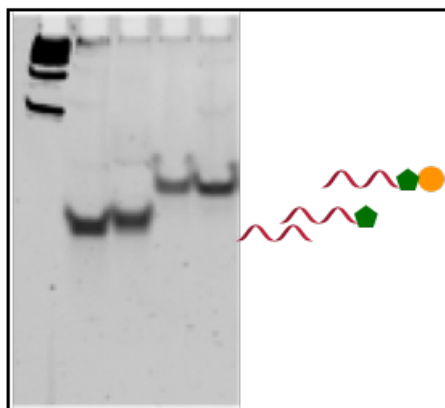


Figure 4.5. 20% PAGE gel electrophoresis analysis of anti-handle ssDNA-peptide conjugates. Each sample was run on a 20% Tris-Glycine gel at 150 V for 2 hours. Lane 1, 50 bp DNA ladder; lane 2, anti-handle ssDNA; lane 3, anti-handle ssDNA with DBCO linker; (green pentagon) lane 4, anti-handle ssDNA with HPQ and scrambled peptides (green pentagon+orange circle).

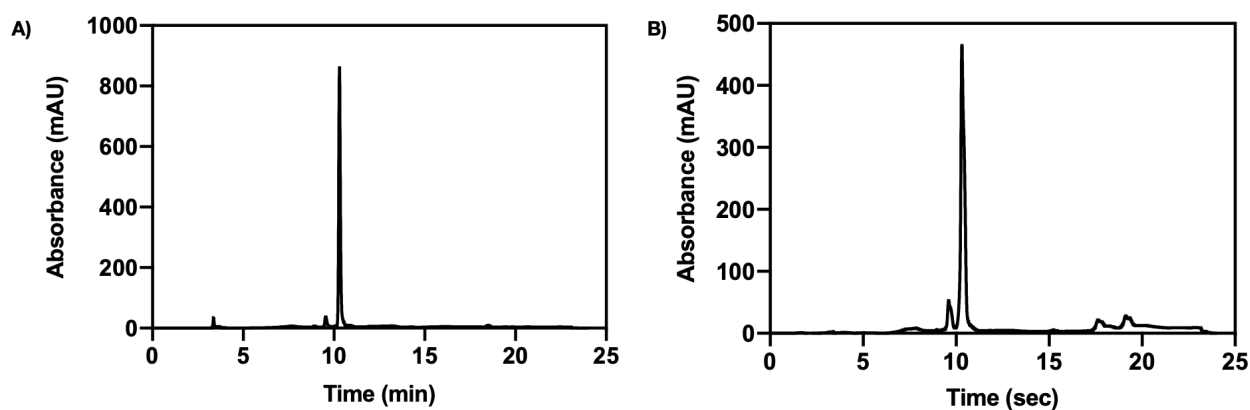


Figure 4.6. HPLC traces of A) ssDNA-SLLAHPQGGGC conjugate, B) ssDNA-SALQLPHGGGC conjugate. They were characterized with RP-HPLC using a gradient of 15% to 75% TEAA buffer (triethylamine and acetic acid buffer, 100 mM, pH=7) : ACN gradient over 24 minutes.

4.5.3 Self-Assembly of Peptide Functionalized DNA Bivalent Structures

DNA bivalent assemblies, explained in section 2.1, were annealed with anti-handle complementary ssDNA-peptide conjugates with a 1.2-fold excess per handle at 37 °C for 1 h, followed by keeping the system 4°C in the thermocycler. The final functionalized particles were characterized by 10% Tris-Glycine PAGE gels at 150 V, 1h (Figure 4.7). Excess DNA-peptide conjugates were removed by using Amicon 30K filter tubes. Amicon filters were incubated with 0.01% Tween 20 overnight at 4°C to prevent the DNA sticking to filters. The removal process included i) removing Tween 20, ii) 6x washing with MQ for 1 min at 14000xg, iii) adding tripod annealing buffer A, and spinning for 1 min at 14000xg, iv) adding conjugate and topping up buffer A to 500 µL and spinning for 2 min at 5000xg (5 repeats), v) placing the filter upside down and transferring to a new collection tube and spinning for 2 min at 1000xg. The DNA-peptide conjugates were stored at -20 °C.

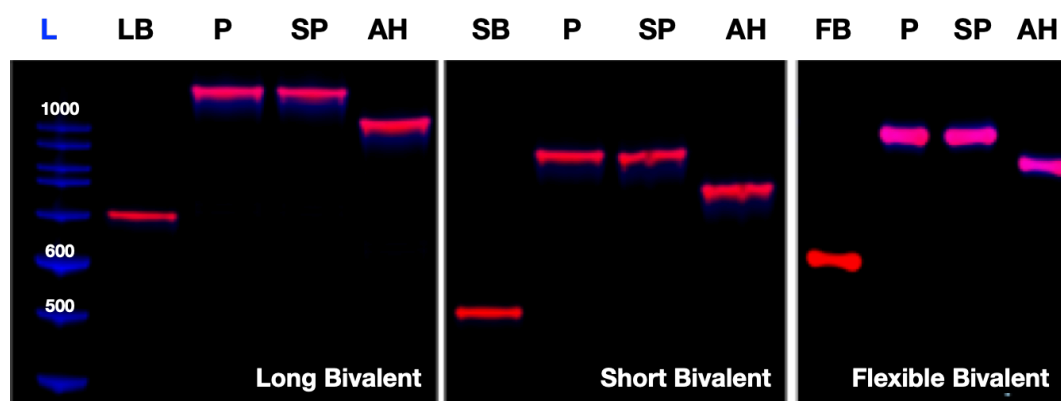


Figure 4.7. 10 % Tris-10% Tris-Glycine PAGE gel electrophoresis of ladder (L), P: peptide functionalized bivalent structures, SP: scrambled peptide functionalized bivalent scaffolds, AH: anti-handle annealed bivalent scaffolds. The gels were run at 150 V for 1 h and scanned on SYBR safe (blue) and Cy5 (red) channels.

4.5.4 Binding Studies using Surface Plasmon Resonance

Binding events are monitored in real time and a range of interaction characteristics such as kinetics, and specificity of an interaction can be determined by using surface plasmon resonance (SPR) which is a label free method to monitor the interaction of the molecules in real time¹³⁹. The approach involves attachment of target molecule to the surface of a sensor chip, and then passing the sample analyte in solution over the target ligand surface. Binding of the analyte to target surface generates a change in refractive index, which is proportional to the bound mass. The SPR technology allows detection of analytes interacting with the immobilized ligands on the chip surface (Figure 4.8). Thus, it can be used to study the interaction of biomolecules from oligonucleotides, proteins, lipids, oligosaccharides, to small molecules, viral particles etc¹⁴⁰. Quantitative data can be easily extracted by measuring the rate of peptide binding to streptavidin and dissociation, giving information about reaction kinetics (k_{on} , k_{off}), and equilibrium constants (K_d).

SPR measurements were performed on a Biacore 8K instrument equipped with a CM3 sensor chip (Cytiva). All buffers were degassed prior to use. Buffer A was used as running buffer at a flow rate 5 µL/min unless otherwise stated. Samples were measured in increasing concentration order. A multi-cycle kinetic program was used. All conditions were carried out in triplicates, whereas negative controls were carried out in duplicates.

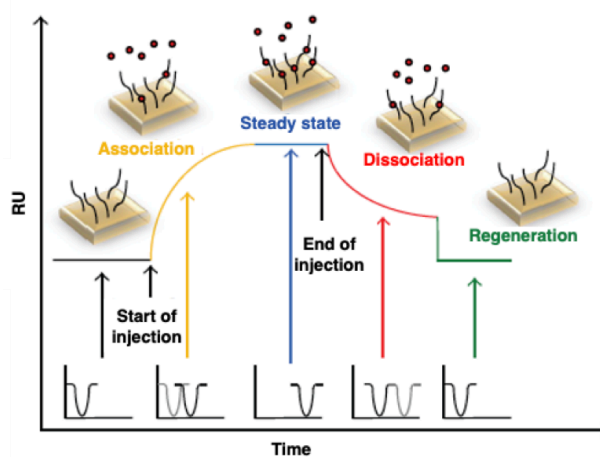


Figure 4.8. Typical shape of SPR-sensorgram which consists of four phases: association, steady-state, dissociation, and regeneration¹⁴⁰.

4.5.4.1 Immobilization of Streptavidin on CM3 Chip

The main goal of immobilization is the attachment of one of the interactants to the sensor chip surface. This immobilization is in the form of covalent bond, hence, permanent or transient by means of capturing. Generally amine coupling is the most applicable coupling chemistry, which includes activation of carboxyl groups on dextran based sensor chip with a mixture of N-hydroxysuccinimide, (NHS), and N-ethyl-N'-(dimethylaminopropyl) carbodiimide, (EDC), to create N-hydroxy-succinimide esters, ligand coupling, and deactivation of activated sites by ethanolamine (EA).

Streptavidin (10 $\mu\text{g}/\text{ml}$ in 10 mM NaOAc, pH=5) in buffer C was immobilized on a surface of a CM3 sensor chip by free amine coupling at a flow rate 5 $\mu\text{L}/\text{min}$ with 600 s contact time, followed by deactivation with ethanolamine following the manufacturer's protocol, which resulted in immobilization level of ~ 1000 final RU (Figure 4.9).

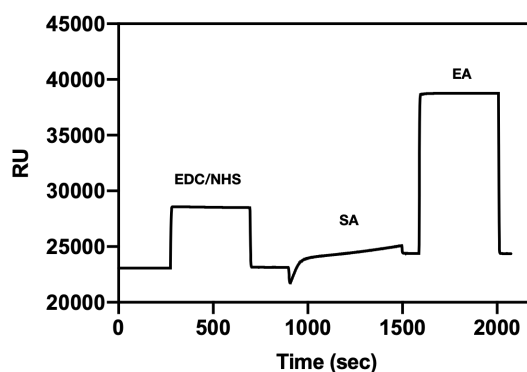


Figure 4.9. Representative SPR sensorgram showing the highly reproducible immobilization of streptavidin protein on CM3 chip surface.

4.5.4.2 SPR Measurements of Peptides

First, we performed SPR analysis of SLLAHPQGGGC and scrambled peptides. A range of concentrations (1000 – 3.9 μM) of peptide constructs were injected sequentially over the flow cell 120 s at a rate of 5 $\mu\text{L}/\text{min}$ followed by a 180 s dissociation time. Background responses of reference flow cells were subtracted from the total response of the experimental flow cell to give the final responses. Samples were measured in increasing concentration order. K_D was obtained from the steady-state fitting of equilibrium binding curves. The monovalent SLLAHPQGGGC peptide showed a very fast on

and off rates with a K_D of $60.6 \pm 2.20 \mu\text{M}$ (Figure 4.10A,B) which is consistent with the previous results¹³². Control experiments using a scrambled sequence (SALQLPHGGGC) showed no binding (Figure 4.10C), which shows the binding is specific for the HPQ motif.

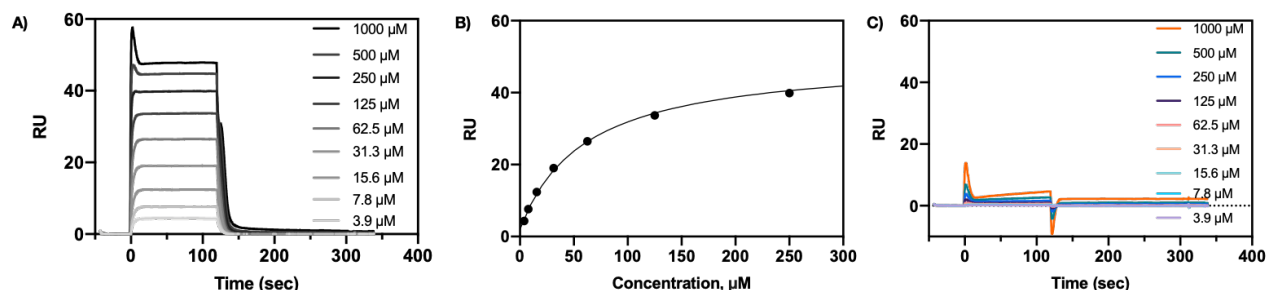


Figure 4.10. A) Biacore raw binding plot of SLLAHPQGGGC peptide only, B) The K_D value of peptide to SA is $60.6 \pm 2.20 \mu\text{M}$ and is obtained from the steady-state fitting of equilibrium curve. Experiments were carried out in triplicates. C) Biacore raw binding plot of scrambled peptide, showing no interaction to SA. Experiments were carried out in duplicates.

4.5.4.3 SPR Measurements of SLLAHPQGGGC Functionalized DNA Bivalent Scaffolds

The dissociation constants of rigid long and short, and flexible bivalent scaffolds were measured in a similar fashion. A range of concentrations (12.5 - 0.1 μM) of analytes were injected sequentially over the flow cell 1200 s at a rate of 5 $\mu\text{l}/\text{min}$ followed by a 600 s dissociation time. Background responses of reference flow cells were subtracted from the total response of the experimental flow cell to give the final responses. Samples were measured in increasing concentration order for accurate measurement of kinetic parameters (Figure 4.11).

Presenting the SLLAHPQGGGC peptide in a minimal (bivalent) multivalent manner increased the binding affinity ~ 60 times for the SA as compared to the monovalent peptide. A 1:1 binding model fit to the data gives a calculated K_D values of $1.00 \pm 0.32 \mu\text{M}$, $1.10 \pm 0.01 \mu\text{M}$, and $1.11 \mu\text{M}$ for LB, SB, and FB respectively. In the steady state, taking the plateaued response value allows the calculation of the dissociation constants, which are in good agreement with the values extracted from the 1:1 binding model and presented in Table 4.1. SPR measurements demonstrated that all bivalent scaffolds show a characteristic SPR binding trace of HPQ peptide to SA protein with a very fast association ($k_{\text{on}} \sim 10^5 \text{ M}^{-1}\text{s}^{-1}$) and very fast dissociation ($k_{\text{off}} \sim 10^{-1} \text{ s}^{-1}$) rate constants, which are very similar to values reported in the literature¹³⁶.

Table 4.1 Binding kinetic data of SLLAHPQGGGC functionalized DNA bivalent structures. Mean \pm SEM values ($n=3$).

Particle/Valency	$k_{\text{off}}, \text{s}^{-1}$	$K_D, \mu\text{M}, \text{from steady state}$	$K_D, \mu\text{M}, \text{kinetic}$
Mono Peptide	-	60.6 ± 2.20	-
Long Bivalent	$(1.11 \pm 0.05) \times 10^{-1}$	0.88 ± 0.03	1.00 ± 0.32
Short Bivalent	$(1.60 \pm 0.02) \times 10^{-1}$	1.35 ± 0.07	1.10 ± 0.01
Flexible Bivalent	$(1.77 \pm 0.04) \times 10^{-1}$	1.40 ± 0.07	1.11 ± 0.00

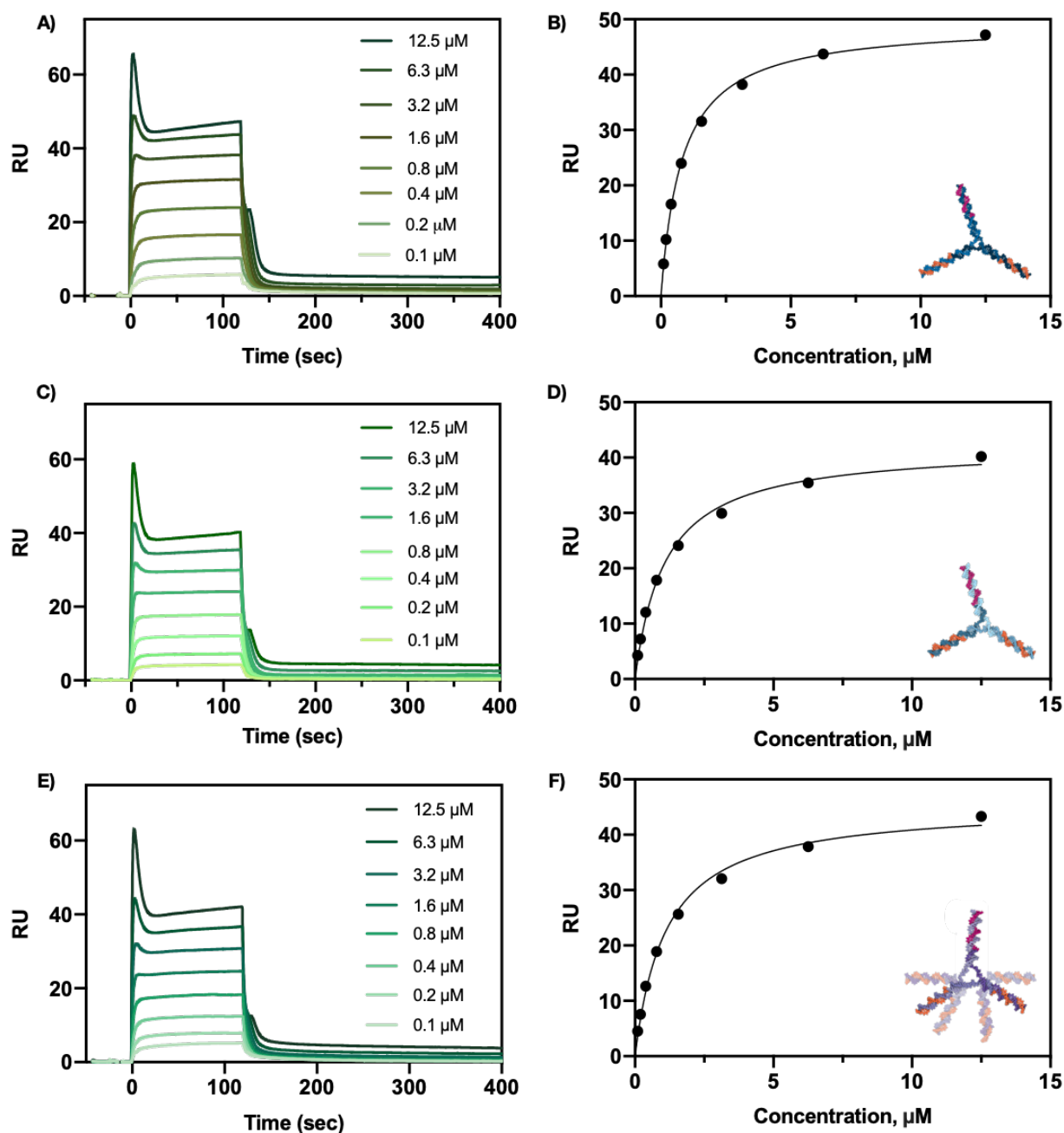


Figure 4.11. Biacore raw binding plots of SLLAHPQGGGC peptide functionalized A) long bivalent, C) short bivalent, E) flexible bivalent constructs, showing injections of serial dilutions (12.5 - 0.1 μM) of particle concentration. Steady-state binding responses (RU) at different concentrations of B) long bivalent, D) short bivalent, F) flexible bivalent for streptavidin. The line represents the fit to 1:1 binding model (right). A multi-cycle kinetic program was used. Experiments were carried out in triplicates.

4.5.4.4 SPR Measurements of Controls

In order to evaluate the nonspecific interactions, several control experiments were performed using scrambled peptide (SALQLPHGGGC) functionalized and non-functionalized (bare) constructs in the similar fashion. A range of concentrations (12.5 - 0.1 μM) of analytes were injected sequentially over the flow cell 1200 s at a rate of 5 $\mu\text{l}/\text{min}$ followed by a 600 s dissociation time. Background responses of reference flow cells were subtracted from the total response of the experimental flow cell to give the final responses. Samples were measured in increasing concentration order. As seen in Figure 4.12, control experiments showed no or negligible binding, showing the binding is specific to HPQ peptide,

which is in good agreement with the literature¹³². These experiments also confirm that there is no unspecific interaction from the DNA scaffold with the target protein.

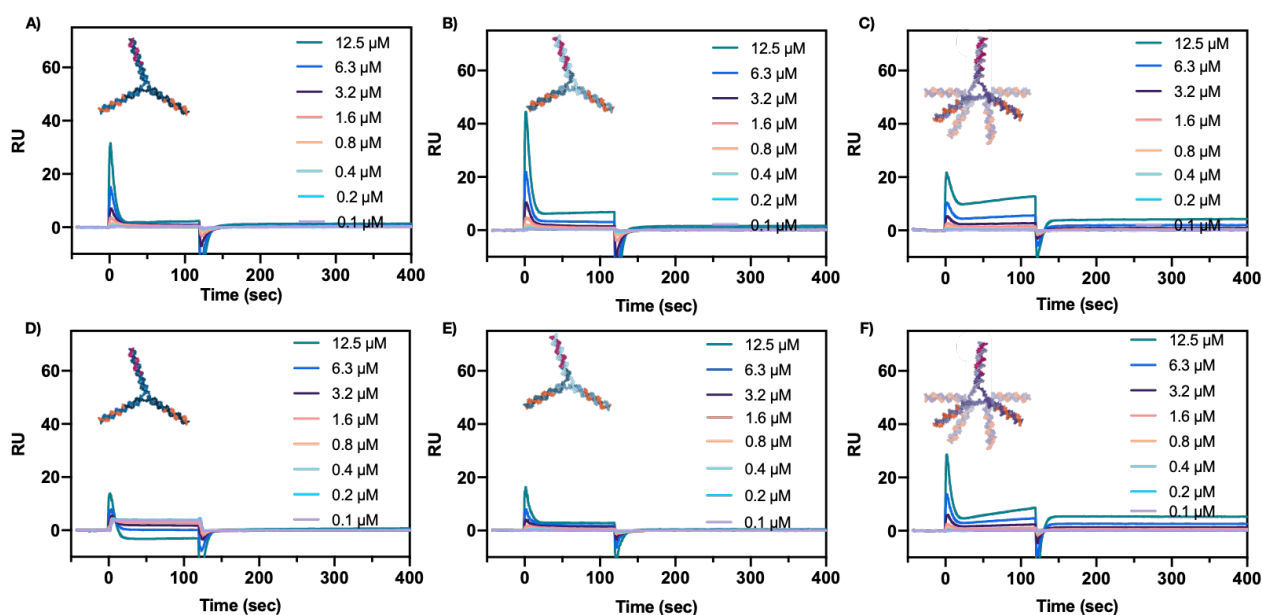


Figure 4.12. Biacore raw binding data plots of scrambled peptide functionalized A) long bivalent B) short bivalent, C) flexible bivalent constructs, and bare (no peptide) D) long bivalent, E) short bivalent, F) flexible bivalent constructs, showing injections of serial dilutions (12.5 - 0.1 μ M) of particle concentration. A multi-cycle kinetic program was used. Experiments were carried out in duplicates.

4.5.5 Binding Studies using Solid Phase Binding Assay

In terms of measuring the steady-state binding affinity between the molecules, one of the main techniques is enzyme-linked immunosorbent assay (ELISA) which is a solid-based assay designed for quantifying and detecting peptides, proteins, antibodies, and hormones¹⁴¹. In ELISA, target protein is immobilized on a microplate well and incubated with an enzyme-labeled antibody to the target protein (or a specific antigen to the target antibody). After washing, the activity of the microplate bound enzyme is measured (Figure 4.13). ELISA has been used for various applications such as screening of high affinity binding peptides¹⁴², detection of antibodies against viruses such as swine influenza virus¹⁴³, evaluation of sensitivity of DNA aptamers¹⁴⁴, identification of cancer biomarkers for early detection of cancer¹⁴⁵, detection of illicit drugs such as cocaine, opiates in urine samples¹⁴⁶.

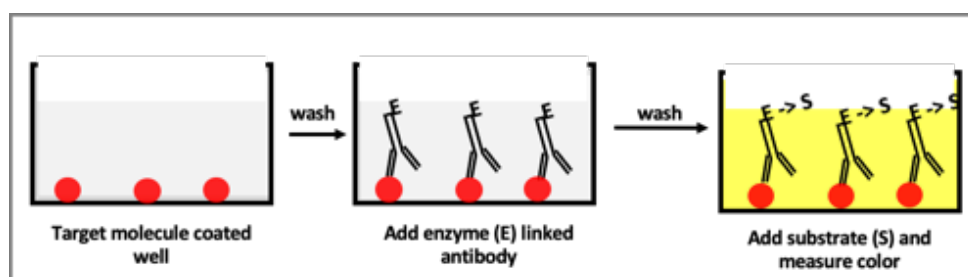


Figure 4.13. Schematic representation of basic type of ELISA.

We used a solid-phase binding assay to evaluate SLLAHPQ functionalized DNA bivalent scaffolds' binding behaviors. Streptavidin was immobilized on a polystyrene surface with different levels of densities (2-100%) as explained in chapter 3. To compare the selectivity of each DNA based bivalent particle, binding behavior for particle concentration of 35 μL of 5 μM DNA bivalent arrays (as it should be above the K_D) were incubated at RT for 2 h. 35 μL of Cy5 functionalized ssDNA as calibration curve dilutions were added in duplicates in respective wells. The unbound particles were washed 3 times with 100 μL of buffer A. Fluorescence intensity of Cy5 was monitored. It was carried out in triplicates. The raw data was treated by subtracting the background from maximum intensities of buffer control wells and scaling intensities to 50 nM Cy5 concentration of suspension wells. The data showed no binding (data not shown), which could be explained by the very fast k_{off} values obtained by SPR measurements. Presenting the SLLAHPQ peptides on a minimal valency could not decrease the dissociation rates of the peptides from the SA receptors. Hence, why we could not observe any binding can be explained by washing off all the bound particles from the surface during the washing step. We also performed qPCR experiments to measure the amount of bound particles on the surface. It also confirmed there is no bound particles on surface, revealing the same result (Figure 6.2 in appendix).

This data confirms a multivalent presentation is needed in order to achieve a stable (and measurable) ligand-receptor complex. Therefore, DNA-origami disks with hexavalent multivalent ligand array are used in order to decrease the off rates of the peptides on the surface, which will be explained in the following section.

4.5.6 SPR Measurement of SLLAHPQGGGC Functionalized DNA Hexavalent Scaffold

In the next step, we presented SLLAHPQ peptide on large hexagon disk (LH) design to decrease the dissociation rate by increasing the valency (from two ligands to six ligands) on the particle scaffold. Due to the limited DNA origami concentration (high DNA origami concentration may result in aggregation), a range of concentrations (50 – 0.4 nM) of disk were injected over the flow cell 420 s at a rate of 5 $\mu\text{L}/\text{min}$ followed by a 600 s dissociation time. Background responses of reference flow cells were subtracted the total response of the experimental flow cell to give the final responses. Figure 4.14 clearly shows that presenting the ligand hexavalently did not change the dissociation rate. It behaves exactly same as monovalent and bivalent scaffolds. Peptides dissociate from the chip surface very fast. We could not get the kinetic data since it did not saturate the chip surface at the highest concentration limit of origami disk used. To sum up, presenting SLLAHPQ peptide in neither bivalent nor hexavalent scaffolds helped to decrease the dissociation rate, therefore, we decided to change the ligand-receptor pairs, which will be explained in the following section.

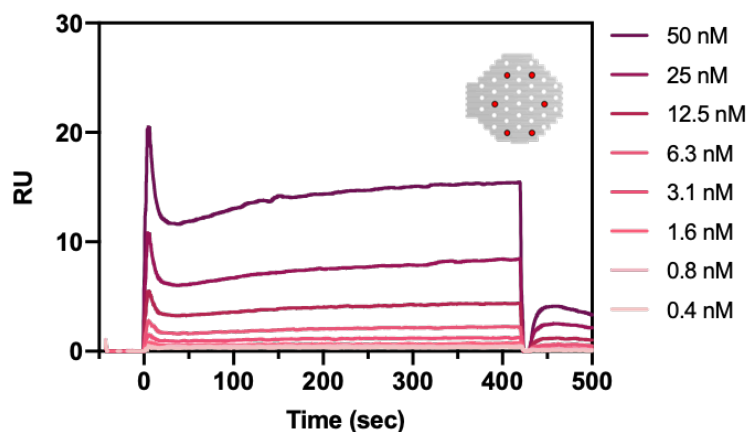


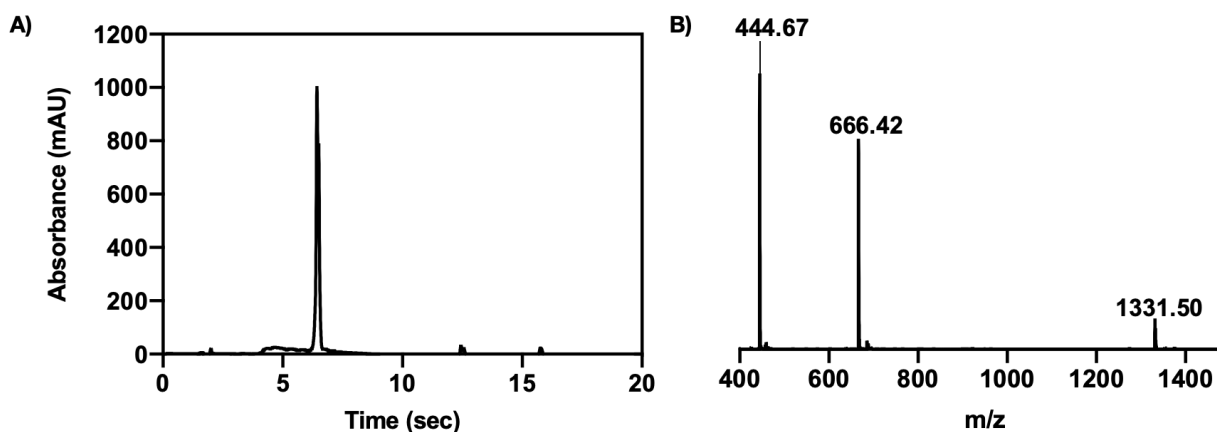
Figure 4.14. Biacore raw binding plot of SLLAHPQ functionalized large hexagon (LH) disk, showing injections of serial dilutions (50 – 0.4 nM) of disk concentration. A multi-cycle program was used.

4.6 Streptactin – Streptag II System

After evaluating the SA – SLLAHPQGGGC system, we decided to use ST protein as receptor and streptag II peptide as ligand, which show a monovalent affinity in the μM region¹⁴⁷.

4.6.1 Synthesis of StreptagII (WSHPQFEKGGGC) and DNA - Peptide Conjugate

Respectively, Fmoc-Cys (Trt)-OH, Fmoc-Gly-OH, Fmoc- Lys (Boc)-OH, Fmoc-Glu (OtBu)-OH, Fmoc-Phe-OH, Fmoc-Gln (Trt)-OH, Fmoc-Pro-OH, Fmoc-His-(Trt)-OH, Fmoc-Ser(tBu)-OH, and Fmoc-Trp (Boc)-OH were coupled. The peptide was cleaved with the cleavage cocktail and was purified by RP-HPLC with a gradient of 10-35% acetonitrile in water in 33 min. m/z Calcd.: 1330.47 Da Obsd. $[M+H]^+$: 1331.50 Obsd. $[M+2H]^{2+}$: 666.42 Da $[M+3H]^{3+}$: 444.67 (Figure 4.15).



C)

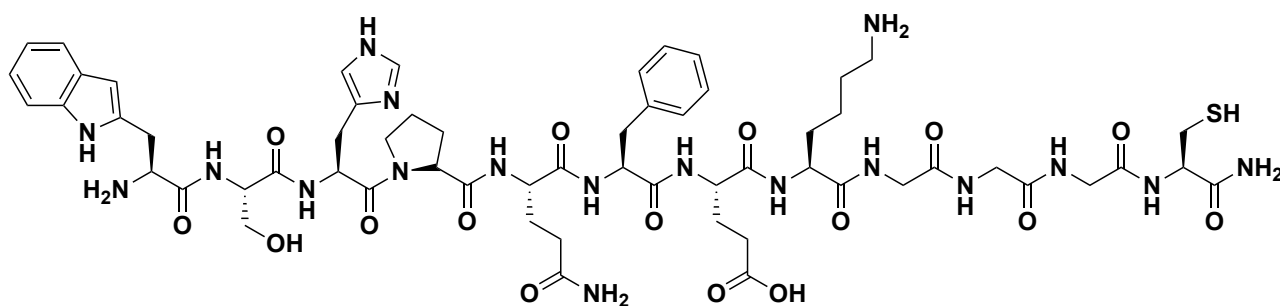


Figure 4.15. A) HPLC trace of Streptag II peptide. B) ESI/MS data of Strep tag II peptide. Calcd. $[M+H]^+$: 1330.47 Da m/z Obsd. $[M+H]^+$: 1331.50 Obsd. $[M+2H]^{2+}$: 666.42 Da $[M+3H]^{3+}$: 444.67. C) Chemical structure of Streptag II peptide.

DNA-STII conjugate was synthesized as explained in section 4.5.2 and its purity was confirmed with RP-HPLC using a gradient of 15% to 75% TEAA buffer (triethylamine and acetic acid buffer, 100 mM, pH=7): ACN gradient over 24 minutes (Figure 4.16).

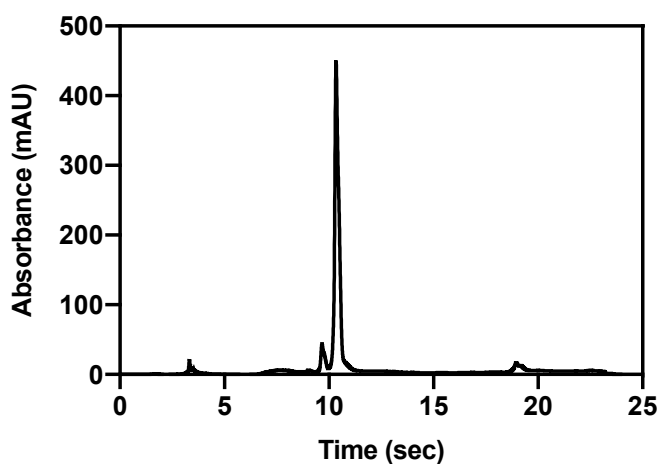


Figure 4.16. HPLC trace of DNA - Streptag II conjugate.

4.6.2 Binding Studies using SPR

SPR measurements were performed on a Biacore 8K instrument equipped with a CM3 sensor chip (Cytiva). All buffers were degassed prior to use. Buffer A was used as running buffer at a flow rate 5 μ L/min unless otherwise stated. Samples were measured in increasing concentration order. A multi-cycle kinetic program was used. All conditions were carried out in triplicates.

4.6.2.1 Immobilization of Streptactin on CM3 Chip

The immobilization of ST protein (6,10 μ g/ml, in 10 mM NaOAc, pH=5) was performed in the same way as explained in section 4.5.4.1 by free amine coupling a flow rate 5 μ L/min with 400-500 s contact time, followed by deactivation with ethanolamine following the manufacturer's protocol, which resulted in immobilization level of \sim 1500 final RU (Figure 4.17). As the density of model receptor (ST) on SPR chip may influence the binding kinetics by allowing a monovalent binding of tripods to one protein on the chip, we immobilized enough protein to facilitate the bivalent binding only.

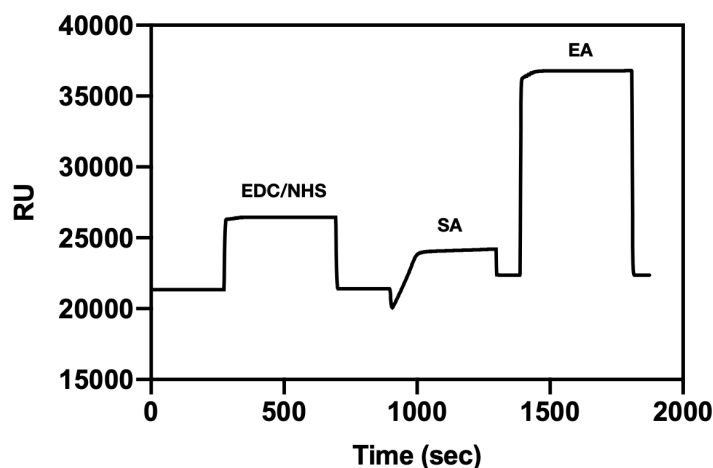


Figure 4.17. SPR sensorgram showing the immobilization of streptactin protein on CM3 chip surface.

4.6.2.2 SPR Measurements of Streptag II peptide

First, we performed SPR analysis of STII peptide only. A range of concentrations (40 – 0.3 μM) of peptide constructs were injected sequentially over the flow cell 120 s at a rate of 5 $\mu\text{l}/\text{min}$ followed by a 600 s dissociation time. Background responses of reference flow cells were subtracted from the total response of the experimental flow cell to give the final responses. Samples were measured in increasing concentration order. The monovalent Streptag II peptide showed a very fast dissociation ($k_{\text{off}} = (0.6 \pm 0.004) \cdot 10^{-1} \text{ M}^{-1} \text{ s}^{-1}$). In the steady state, taking the plateaued response value allows the calculation of the dissociation constant of $2.99 \pm 0.21 \mu\text{M}$ (Figure 4.18) which is consistent with the previous results¹⁴⁷.

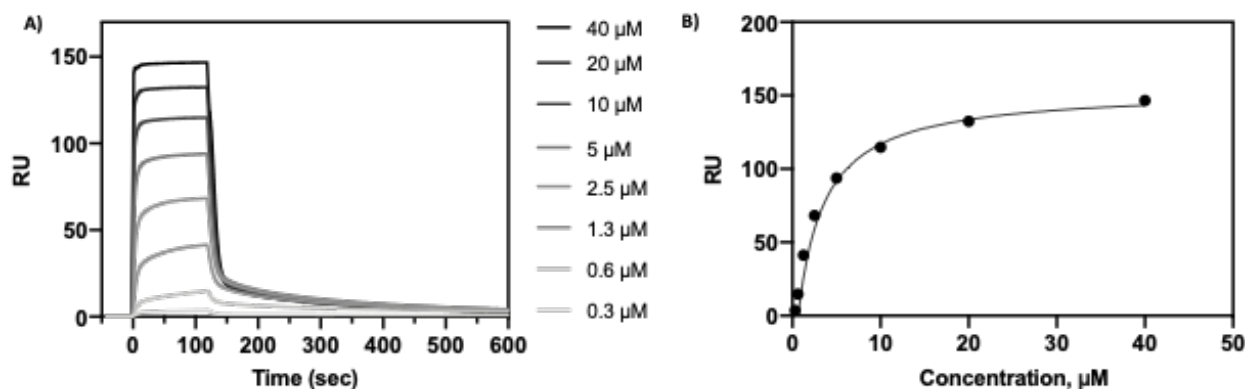


Figure 4.18. A) Biacore raw binding plot of Streptag II peptide, showing injections of serial dilutions (40 – 0.3 μM) of peptide concentration (left). B) Steady state binding response (RU) at different concentrations for streptactin gives the K_D value of peptide to SA is $2.99 \pm 0.21 \mu\text{M}$. The line represents the fit to 1:1 binding model (right). A multi-cycle program was used. Experiments were carried out in triplicates.

4.6.2.3 SPR Measurements of Streptag II Functionalized DNA Bivalent Scaffolds

The dissociation constants of DNA bivalent scaffolds were measured in a similar fashion. A range of concentrations (500 – 15 nM) of analytes were injected sequentially over the flow cell 240 s at a rate of 5 $\mu\text{l}/\text{min}$ followed by a 900 s dissociation time. Background responses of reference flow cells were subtracted from the total response of the experimental flow cell to give the final responses. Samples were measured in increasing concentration order.

Presenting the ST II peptide in a bivalent manner increased the binding affinity moderately for the ST as compared to monovalent peptide, regardless of scaffold rigidity or spacing. In the steady state, taking the plateaued response value allows the calculation of the dissociation constant of ~ 225 nM (Table 4.2, Figure 4.19). Interestingly, this matches the affinity measured for a bivalent streptavidin binding antibody (Figure 6.4 in appendix), which displays a similar geometry as our DNA tripods. This moderate increase in affinity suggests that a higher valency is needed to observe the effect of strength in numbers. Moreover, relatively slow dissociation rate constants ~ 10 s⁻¹ (Table 4.2) were detected, which confirms a multivalent presentation is required to achieve a stable and measurable ligand-receptor complex.

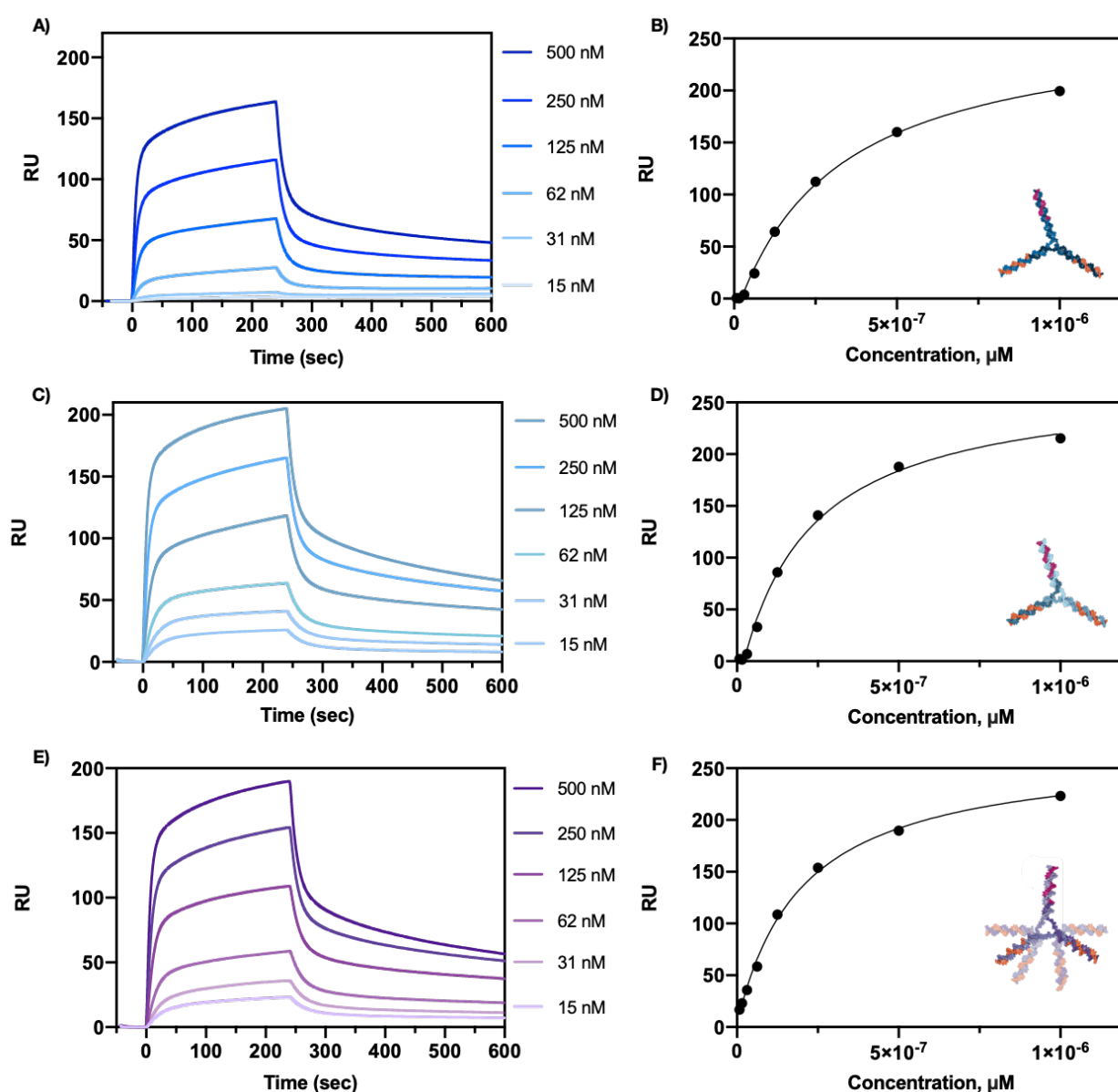


Figure 4.19. Biacore raw binding plots of Streptag II functionalized A) long bivalent, C) short bivalent, E) flexible bivalent constructs, showing injections of serial dilutions (500– 15 nM) of particle concentration. Steady-state binding responses (RU) at different concentrations for streptactin gives the K_D value of 220 ± 51 nM, 216 ± 16 nM, and 246 ± 25 nM ($n=3$) for B) long bivalent, D) short bivalent, F) flexible bivalent constructs respectively.

A multi-cycle program was used. Experiments were carried out in triplicates.

4.6.3 Binding Studies of Streptag II Bivalent Scaffolds by Solid-Phase Binding Assay

4.6.3.1 Affinity Analysis of Analytes on High Density Surfaces

Regardless of the type of architecture, the highest avidity is measured on the densest receptor surfaces, as the Langmuir isotherm of the occupied surface is at its maximum⁴⁸. Since the analytical method used can influence or bias the affinity parameters¹³², we combined solid-state technique with SPR to obtain both static and kinetic affinity data. In order to obtain static affinity data of monovalent peptide, STII peptide was conjugated to CF488A dye for fluorescence readout to perform the binding assay. StreptagII peptide was dissolved in PBS and to make 50 mM stock solution, and 10-fold molar excess of TCEP reducing gel slurry was added to reduce the disulfide bonds. The reaction mixture was mixed at room temperature for 1 h. The TCEP gel slurry was removed by Pierce™ Spin Cups - Paper Filters by centrifugation once for 1 min at 1500 g. CF488A maleimide dye (1 μ mole) was warmed to room temperature. 100 μ L DMSO was added to the vial to make a 10 mM stock solution. While stirring the peptide solution, the dye stock was added to result in a dye/peptide molar ratio of 1.2. The reaction mixture was stirred at room temperature for 2 hours. Peptide-dye conjugate concentration was quantified by Pierce quantitative peptide assay. After confirming the peptide stock concentration, a dilution range of peptide (15 – 0.05 μ M) was incubated on 100%, receptor density. 35 μ L of CF 488A dye as calibration curve dilutions were added in duplicates in respective wells. The unbound particles were washed 3 times with 100 μ L of buffer A. Fluorescence intensity of CF 488A was monitored, in quintuplicates. The raw data was treated by subtracting the background from maximum intensities of buffer control wells and scaling intensities to 50 nM CF 488A concentration of suspension wells. Readout of CF 488A fluorescence intensity yielded a binding curve that showed a K_D of 865.7 nM when fitted by nonlinear regression using specific binding with Hill slope on Prism (Figure 4.20).

Next, we studied the binding properties of STII functionalized bivalent scaffold (LB tested only) to ST-coated wells. A dilution range of the tripod (5000 – 5 nM) was incubated at RT for 2 h. 35 μ L of Cy5 functionalized ssDNA as calibration curve dilutions were added in duplicates in respective wells. The unbound particles were washed 3 times with 100 μ L of buffer A. Fluorescence intensity of Cy5 was monitored. The experiments were carried out in quintuplicate. Readout of Cy5 fluorescence intensity yielded a binding curve that showed a K_D of 194.2 nM when fitted by nonlinear regression using specific binding with Hill slope on Prism (Figure 4.20), which is in good agreement with SPR measurements. Steady-state binding curve obtained by solid-phase assay indicates that the shift from monovalent to bivalent leads to roughly an order of magnitude stronger binding. This moderate increase in affinity obtained by steady states also suggests that a higher valency is needed to observe the effect of strength in numbers.

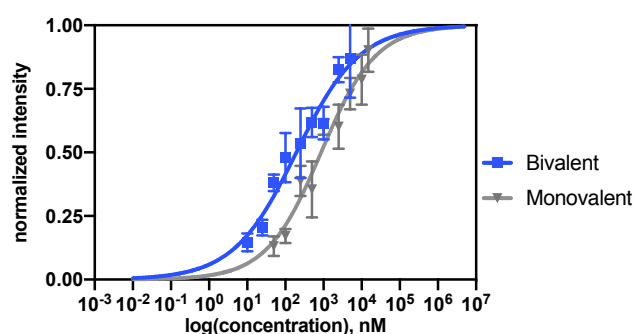


Figure 4.20. Binding data of monovalent and bivalent array on 100 % ST coated surfaces. Error bars represent \pm SD (n=5). The solid line represents the fit by nonlinear regression using specific binding with a Hill slope, K_D of 865.7 nM and 194.2 nM for monovalent and bivalent respectively.

4.6.3.2 Multivalent Pattern Recognition in the Low-Valency Regime

The affinity data on the densest surfaces provided the concentration range for spatial-tolerance experiments, as these should be above the K_D , but below the concentration where an onset of the lower valency can blur the pattern recognition effect. For the bivalent arrays, the working concentration was 1 μM , which unfortunately matches the K_D of the monovalent peptide. Hence, the effect of spatial tolerance is expected to be obscured by the monomeric contribution that interferes with the readout (Figure 4.21). We nevertheless tested the binding of all bivalent constructs with their respective spatially matching receptor surfaces using a solid-phase binding assay by incubation 1 μM bivalent scaffolds on different receptor densities (2-100%). Indeed, no discrimination in binding between the rigid long, short, and flexible arrays was observed (Figure 4.22A). Additionally, ideal receptor spacing matching rigid long and short bivalent arrays (11, 16%) are situated very close, which we hypothesized to significantly obscure the selective binding since the receptors on the surface are randomly positioned.

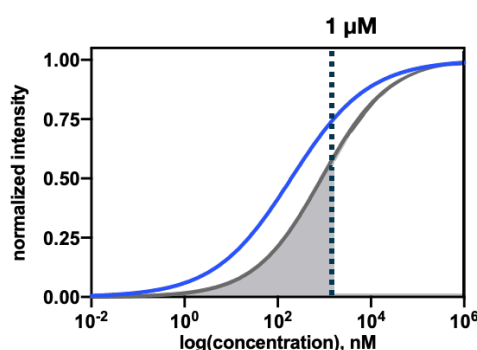


Figure 4.21. Representation of monomeric contribution highlighted as grey area to bivalent arrays. When 1 μM of bivalent particle concentration was used, the effect of monomeric contribution was also observed as highlighted in grey since it matches the K_D of monovalent peptide.

As a receptor can only bind one ligand and the interactions are independent, the data was fit using a simplified form of binding curve proposed by Frenkel *et al.*⁴⁸. According to his model, there are four parameters to control when designing a super-selective materials: valency, receptor density, ligand-receptor binding strength (f), and activity of particles in solution (k). The impact of valency and receptor density on super-selective binding is discussed in detail in chapter 1. Binding strength is individual binding strength, and it relates to the valency of the system. Activity is dimensionless parameter, and directly proportional to the concentration (density) of particles in solution and the ratio of equilibrium constants for the formation of first bond and the subsequent ligand-receptor bonds. Maximum selectivity is limited by activity, k ; lowering the activity or density of particles increases the selectivity. The system's strength of binding (f) was kept constant as we obtained similar affinities for all bivalent particles. Activity (k) was found to be very similar in all constructs, indeed confirming the marginal gain in affinity obtained through a bivalent ligand display (Table 4.3). Previously, Frenkel *et al.* introduced the selectivity parameter α as measure of the sensitivity of the binding of multivalent particles to the surface concentration of receptors⁴⁸. α is the slope of the adsorption profile in a log-log plot and is lower than 1 for monovalent binding, while for multivalent interactions, the selectivity can reach values much greater than 1. For our bivalent arrays, α barely exceeded 1, excluding true super-selective behavior for these bivalent interactions (Figure 4.22B). This behavior again corresponds with that of a bivalent IgG antibody, which shows a similar binding curve and no super-selectivity in its interaction with surfaces of increasing receptor density (Figure 6.5 in appendix).

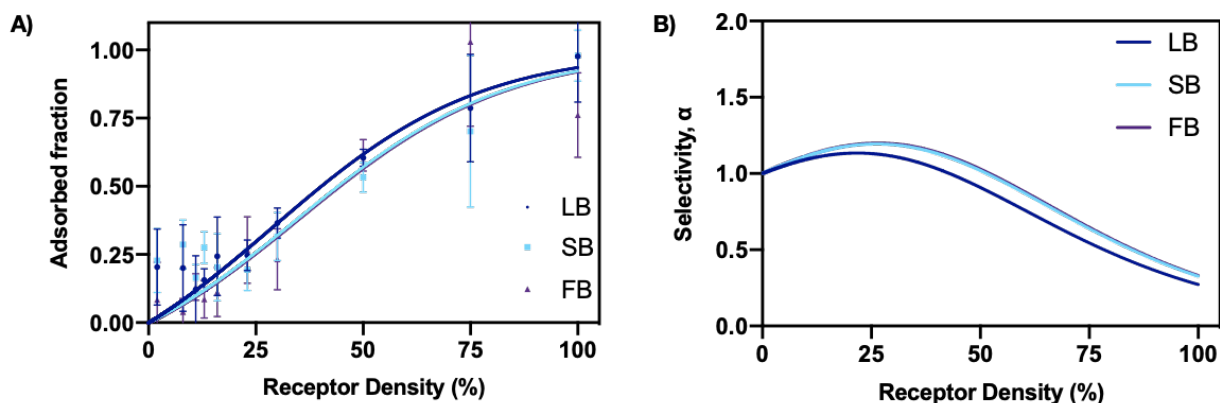


Figure 4.22. A) Super-selective binding profile of bivalent scaffolds. Error bars represent \pm SD (n=5). B) The parameter alpha, α as a function of receptor density (%). No serious super-selectivity is observed.

The moderate increase in affinity obtained by both SPR and solid-phase assay and spatial tolerance experiments confirmed the need for higher valency to observe the effect of strength in numbers.

4.6.4 Binding Studies of Streptag II Functionalized DNA Hexavalent Scaffolds using SPR

To increase ligand valency, we presented Streptag II peptide on the disk designs (rigid large hexagon, rigid small hexagon, and flexible hexagon, Figure 2.6C) to increase the shift in K_D by increasing the valency from one ligand to six ligands on the particle scaffold. As discussed in section 3.3.2, the target surfaces to match the spacings of attachment points for rigid large and small hexagons are 7 % and 56 % respectively. Hence, there is enough separation between the surface spacings of rigid designs, which would truly contribute to a potential selective pattern-based binding.

A range of concentrations (10 – 0.1 nM) of disk was injected over the flow cell 420 s at a rate of 5 μ l/min followed by a 600 s dissociation time. Surface was regenerated with the injection of buffer D. Background responses of reference flow cells were subtracted the total response of the experimental flow cell to give the final responses. SPR analysis of hexavalent scaffolds (Figure 4.23) clearly showed the effect of valency on both the overall affinity as well as binding kinetics. Presenting the peptide hexavalently enhances the binding by 3 orders of magnitude. Additionally, dissociation rates significantly slowed down, $k_{off} \sim 10^{-5} s^{-1}$, yielding a stable complex (Figure 4.24, Table 4.2).

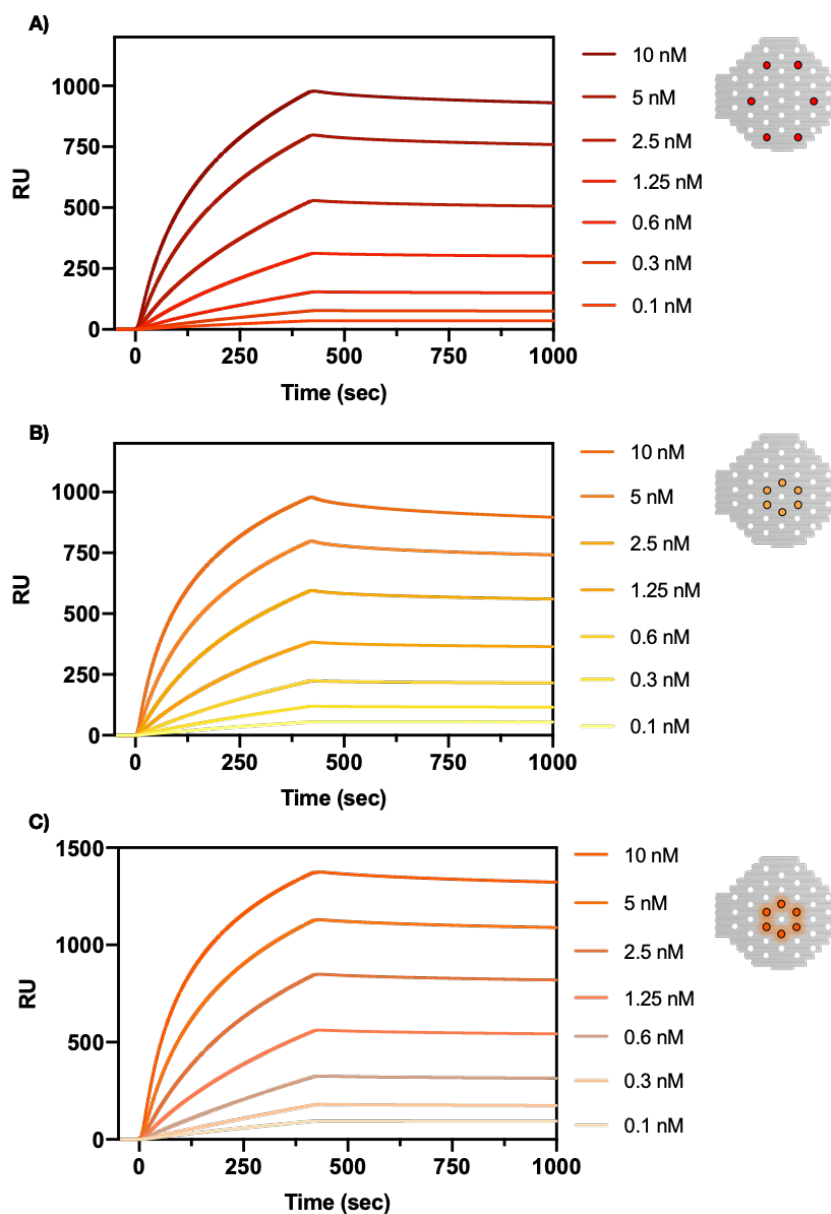


Figure 4.23. Biacore raw binding plots of Streptag II functionalized A) large hexagon, B) small hexagon, and C) flexible hexagon, showing injections of (10 – 0.1 nM) of particle concentration. A multi-cycle kinetic program was used, and the experiments were carried out in triplicates.

Table 4.2. Binding kinetic data of ST II functionalized particles, represented as Mean \pm SEM values (n=3).

Particle/Valency	k_{off}, s^{-1}	K_D, pM
Monovalent Peptide	$(0.6 \pm 0.004) * 10^{-1}$	$(2.99 \pm 0.21) * 10^6$
Long Bivalent	$(4.97 \pm 2.4) * 10^{-2}$	$(220 \pm 51) * 10^3$
Short Bivalent	$(7.99 \pm 0.79) * 10^{-2}$	$(216 \pm 16) * 10^3$
Flexible Bivalent	$(7.31 \pm 0.77) * 10^{-2}$	$(246 \pm 25) * 10^3$
Large Hexagon	$(6.57 \pm 1.43) * 10^{-5}$	(76.6 ± 9.05)
Small Hexagon	$(6.76 \pm 0.79) * 10^{-5}$	(86.9 ± 0.16)
Flexible Hexagon	$(2.84 \pm 1.01) * 10^{-5}$	(29.7 ± 10.9)

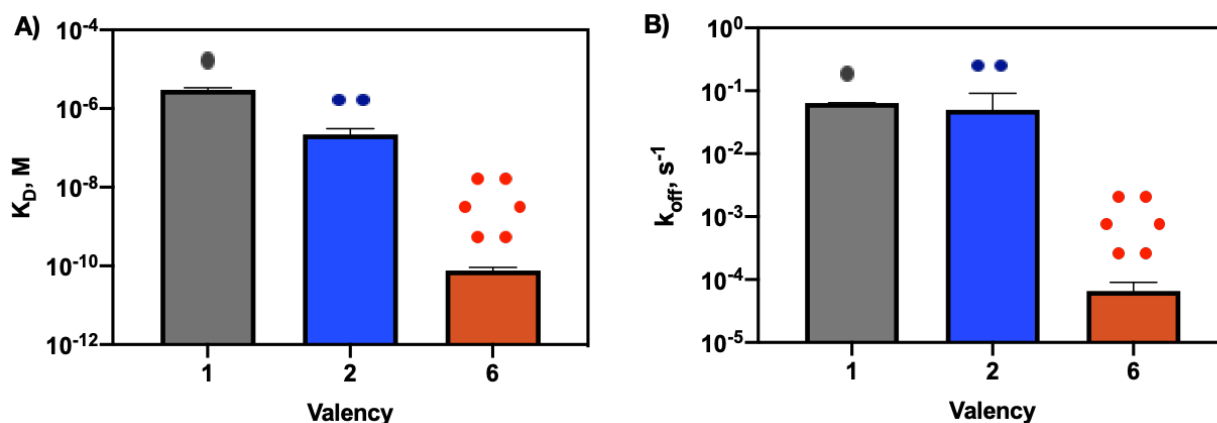


Figure 4.24. A) K_D values obtained by SPR measurements for monovalent, bivalent, and hexavalent scaffolds. B) k_{off} values obtained by SPR measurements for monovalent, bivalent, and hexavalent scaffolds. Error bars represent \pm SD (n=3).

4.6.4.1 SPR Measurements of Controls

Control experiments using bare disk (without functionalization) and one handle (monovalent) functionalized disk were performed in a similar fashion. As seen in Figure 4.25A, bare disk showed no binding, indicating binding is specific to ST II peptide. SPR analysis of monovalent control disk shows very fast on/off rates (Figure 4.25B), as monovalent peptide scaffold where binding reaches steady state very rapidly and binding curves look like square pulses, unlikely hexavalently peptide functionalized DNA-origami disks (LH, SH, and FH) where on and off rates are very slow (Figure 4.23).

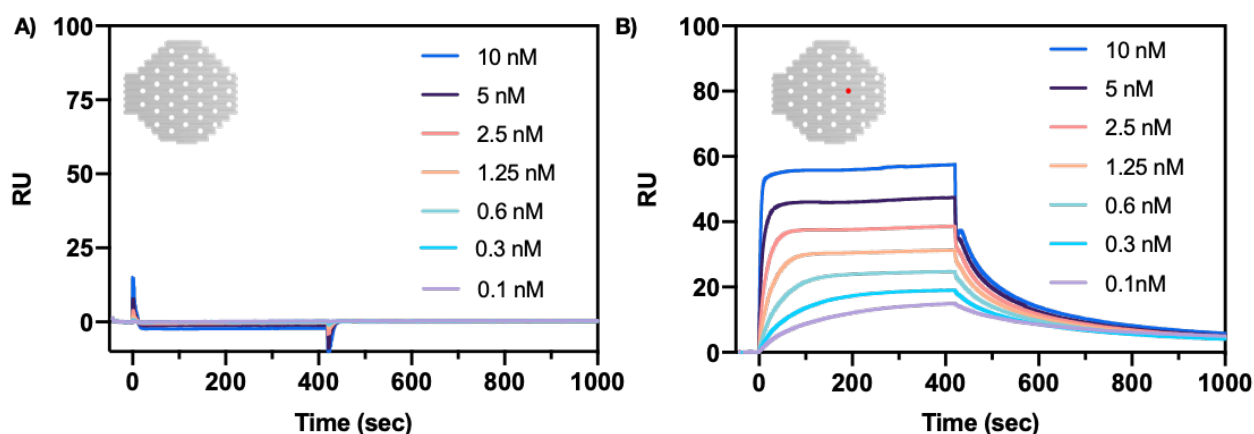


Figure 4.25. Biacore raw binding plots of A) bare disk (without peptides), and B) 1x handle disk, showing injections of serial dilutions (10 - 0.1 nM) overflow cells. It was carried out in duplicates.

4.6.5 Binding Studies of Streptag II DNA – Origami Disks using Solid Phase Binding Assay

4.6.5.1 Affinity Analysis of Analytes on High Density Surfaces

Static affinity analysis of hexavalent scaffolds was performed using solid-phase binding assay. A 96 well plate was coated with ST (100%), and a dilution range of disks (5 – 0.01 nM) was incubated at RT for 2 h. 35 μ L of Cy5 dye as calibration curve dilutions were added in duplicates in respective wells. The unbound particles were washed 5 times with 100 μ L of buffer B. Fluorescence intensity of Cy5 was monitored. Experiments were carried out in quintuplicate. The raw data

was again treated by subtracting the background from maximum intensities of buffer control wells and scaling intensities to 10 nM Cy5 concentration of suspension wells. Readout of Cy5 fluorescence intensity yielded a binding curve that showed a K_D of ~ 2 nM for all disks when fitted by nonlinear regression using specific binding with Hill slope on Prism (Figure 4.26). Presenting the STII peptide on the disk with a hexavalent array demonstrated the highest affinity, gaining ~ 3 orders of magnitude compared to monovalent peptide. For the dense surfaces, as expected, no significant differences between rigid or flexible ligand arrays were detected. The DNA backbone pre-orientes ligands to favor binding, so a conformational entropic penalty is minimal, even for the flexible constructs. The ΔG of avidity¹⁴⁸ is dominated by the intermolecular ΔG which does not significantly vary between the different constructs. The flexibility is therefore only significant for the ligand spacing, e.g. overall spatial tolerance of the system, which conveniently makes all constructs comparable with regard to their overall target affinity.

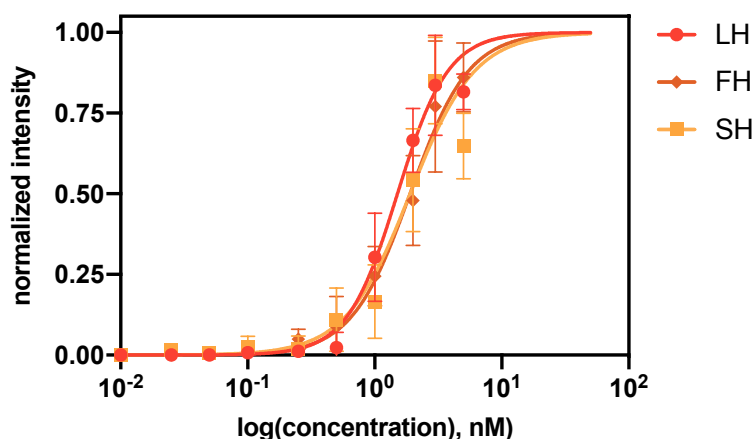


Figure 4.26. Solid phase binding assays of disks functionalized with StreptagII peptide on 100 % ST coated polystyrene surfaces. Error bars represent \pm SD (n=5). The solid line represents the fit by nonlinear regression using specific binding by a Hill slope, with a K_D of ~ 2 nM of disk concentration.

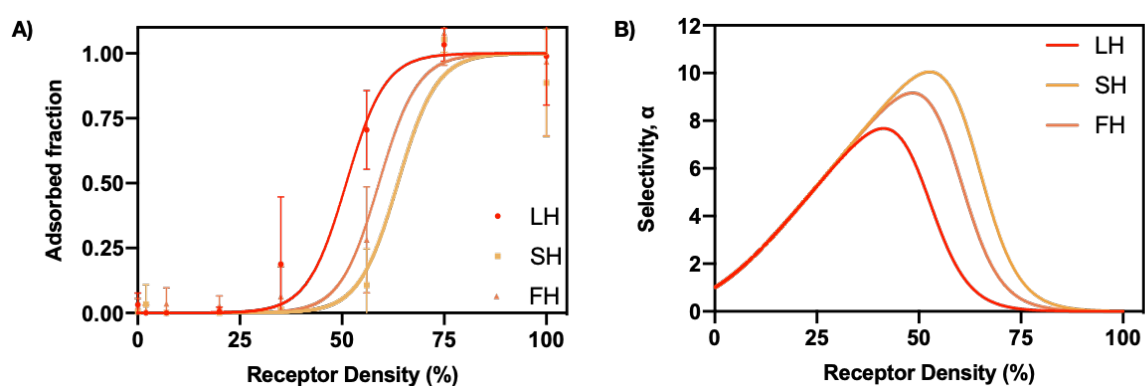
4.6.5.2 Multivalent Pattern Recognition in the Low-Valency Regime

Spatial tolerance experiments of hexavalent ligand arrays were performed in a similar fashion as explained in section 4.6.3.2. A more pronounced pattern-based multivalent binding behavior was anticipated for the hexavalent ligand array. The working concentration based on the dense surface analysis was set for 3 nM, which is 2 orders lower than the bivalent construct, thereby preventing any interference of lower valency interactions. Additionally, the ideal receptor spacing matching the large and small hexagon patterns are situated much further apart than for the bivalent construct, which we hypothesized to significantly contribute to a potential selective pattern-based binding. We prepared test surfaces matching the pattern spacing of the 3 hexavalent disks (7, 24, and 56% for large, small, and flexible designs respectively), as well as higher and lower density ranges to evaluate super-selectivity. Solid-phase binding assays convincingly showed the effect of rigidity and pattern-spacing on multivalent binding (Figure 4.27A). The rigid small hexagon required a receptor density of 56% in order to bind, corresponding to a receptor spacing of 8 nm, perfectly matching the spatial tolerance of the small rigid array. Contrary, the rigid large hexagon pattern showed a stable interaction onset at a receptor density of 35 % which is lower than the LH ligand spacing of 21 nm. We hypothesize that this discrepancy is caused by the random distribution of receptors on the test surfaces, which present a wider probability distribution function in the lower density regime (Figure 3.7). The lower occurrence of the matching spacing inevitably leads to

difficulties in detection as it approaches the limit of the measurement sensitivity, as confirmed with biotin functionalized LH control (Figure 6.6). Interestingly, the flexible small hexagon, expected to bind patterns starting from a 24% receptor density, indeed shows an onset in ligand-receptor complexation at this coverage. As FH is based on the SH pattern, but with added spatial tolerance through the flexible linkers, this structure shows a higher spatial tolerance than the rigid small hexagon and starts to bind at lower density surfaces compared to the SH.

Following the same analysis as for the bivalent binders, all hexagonal patterns were fit using a simplified binding curve proposed by Frenkel *et.al.*⁴⁸ and showed a strong super-selective binding, as the selectivity parameter α lays above 1 for all arrays (Figure 4.27B). All patterns indeed show a steep switch-like response when their target spacing is present and α peaks at 8, 9, and 10 for LH, SH and FH respectively. To the best of our knowledge, these are the highest selectivity numbers reported for low-valency spatially constrained architectures. The significant differences between bivalent and hexavalent arrays are directly linked to the systems' degeneracy, Ω . The degeneracy depends on the spatial arrangement of ligands and receptors and reflects the statistical possibilities of forming an interaction between them. For the bivalent constructs, under the spatial tolerance threshold density, Ω is 2, whereas a linear increase from 4 onward is observed at matching receptor spacing, and higher densities. Hence, we never enter a steeply increasing non-linear regime that can lead to super-selective binding. On the contrary, the hexavalent arrays can increase the number of bonds when the receptor density increases, until all 6 ligands have found a binding partner. The degeneracy develops from 6 exponentially, thereby strongly affecting the super-selective character of the overall avidity.

Taken together, our data shows that when the monovalent and multivalent affinity between a ligand-receptor couple is sufficiently distinct, spatial-constrained presentation of ligands can lead to a strong super-selective behavior which we label multivalent pattern recognition (MPR, Figure 4.27C). A certain spatial tolerance in the scaffold is required to allow for the specific ligand-receptor complex to form, however, the overall pre-orientation and pattern-based ligand presentation strongly reduces the rotational and translational entropy penalties. When the system's threshold pattern density is reached, the characteristic switch-like onset of binding for super-selectivity is apparent. Patterns with a rotational symmetry and homogeneous ligand spacing, as used in this study, gain in degeneracy of binding and thereby favor the overall apparent avidity. However, for more complex patterns, the balance of monovalent versus multivalent affinity will define the critical spatial-tolerance and receptor threshold of binding.



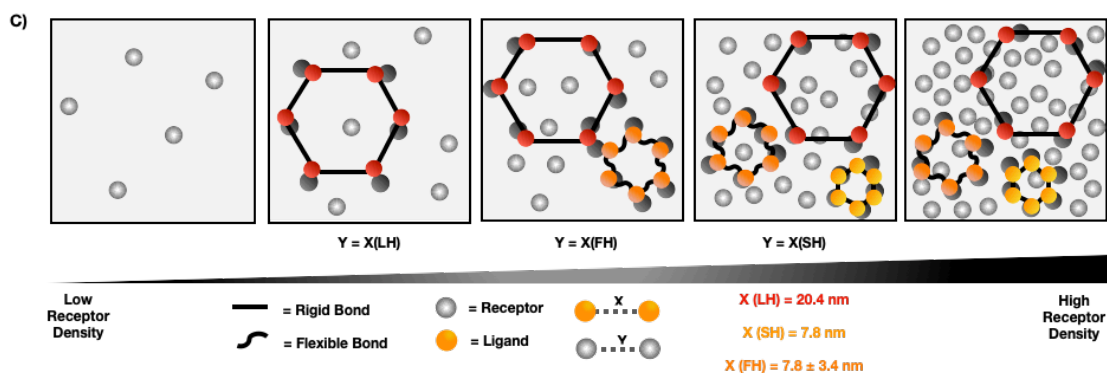


Figure 4.27. A) Super-selective binding profiles of hexavalent scaffolds. Error bars represent \pm SD ($n=5$). B) The parameter alpha, α as a function of receptor density (%). C) Schematic representation of how each hexagon pattern interacts with the receptors on different surface densities.

Table 4.3. Fitting data parameters, where k is activity, f is binding strength, b is maximum signal.

Particle	k	f	b	R^2
Long Bivalent	0.23	0.04	2352	0.88
Short Bivalent	0.19	-	1895	0.82
Flexible Bivalent	0.19	-	1715	0.75
Large Hexagon	$2.23 \cdot 10^{-5}$	0.23	2654	0.85
Small Hexagon	$1.58 \cdot 10^{-6}$	-	1536	0.92
Flexible Hexagon	$4.20 \cdot 10^{-6}$	-	2169	0.84

4.6.6 Conclusion

In this chapter, two different scaffolds (tripods and DNA-origami disks) introduced in chapter 2 were functionalized with two different ligands: SLLAHPQGGGC and Streptag II peptides. First, SLLAHPQGGGC-SA system was studied. After the successful assembly of bivalent scaffolds, their affinity analysis was performed by using SPR. It was found that binding affinity was increased ~ 60 times when the peptide was presented bivalently on the tripods. On the other hand, it was also confirmed that the dissociation rate, k_{off} , could not be slowed down despite the peptide was presented hexavalently on the disk. Due to fast dissociation rates obtained from this ligand-receptor pair, we could not obtain any binding data.

Next, we focused on the second ligand, the Streptag II peptide. Affinity analysis showed that a moderate increase in affinity was observed from monovalent to bivalent. When Streptag II peptide was presented hexavalently on the disks, ~ 3 orders of magnitude increase in affinity compared to monovalent was observed. As expected, for the dense surfaces, no difference was found between the rigid and flexible structures. Additionally, the k_{off} significantly slowed down when the peptide presented on the disks, yielding a very stable ligand-receptor complex. Finally, spatial tolerance experiments were performed with bivalent and hexavalent scaffolds and demonstrated that no super-selectivity was observed with bivalent arrays (tripods), whereas a pattern-based multivalent binding behavior was observed with hexavalent arrays (disks).

In this chapter, we explored how affinity, valency, and rigidity can control the onset of super-selective multivalent binding. It was shown that pattern-dependent onset of multivalent binding can be achieved when the spatial tolerance of the particles matches the target receptor's average spacing. For the same valency, a different receptor density sensitivity based on the ligand pattern spacing was measured, which is distinct from general super-selectivity. This pattern-based super selectivity regime is present in low-valency systems where the affinity between monovalent and multivalent presentation is distinct, and the multivalent residence time is sufficiently long (e.g. slow off rates). The demonstration of MPR additionally opens an engineering space for targeted nanomaterials where spacing of receptors is important for biological signaling. Additionally, our data shows that the presence of flexible linkers for ligand presentation can impact the targeting as their sensitivity towards receptor density shifts.

Chapter 5 Conclusion and Outlook

This thesis focuses on the use of DNA nanotechnology to engineer spatially-controlled a library of scaffolds to explore how valency, affinity, and rigidity control the super-selective multivalent binding, which is characterized by a strong density-dependent onset of ligand-receptor complexation. Previous studies on this mechanism have explored the engineering parameters that promote the strongest super-selective behavior, being dominated by high valency and flexible ligand presentation⁴⁸. In the high valency regime, any influence of spatial tolerance or pattern-recognition is irrelevant as the overall avidity is dominated by the enthalpy of the many interactions formed. In this thesis, we focused on the low-valency regime, as many signaling pathways in nature follow a moderate multivalent setting. Since local receptor densities can be temporarily changed, a super-selective binding mechanism should be present also in the low-valency regime.

To achieve pattern dependent super-selective multivalent binding, we studied two different model ligand-receptor pairs with different affinities: i) streptavidin-SLLAHPQ, and ii) streptactin-streptagII pairs. Unfortunately, we could not obtain selectivity data from the first ligand-receptor pair due to fast dissociation rates, despite the ligand was presented in a hexavalent array. Then, we focused on the second ligand-receptor pair, having relatively stronger affinity compared to first pair. Streptag II peptide was presented on DNA tripods (bivalently) and DNA-origami disks (hexavalently). When tripods were used as scaffolds, no discrimination was observed in binding between the rigid and flexible scaffolds due to monomeric contribution and close target receptor spacing. These observations confirm that a higher valency than two is required to enter a super-selective regime and/or measure a pattern effect in multivalent binding.

Additionally, it is worth noting that there are recent developments in molecular dynamics. During this thesis, recommended ions by Chetam's parameters⁸⁸ were used. However, recent insights from Aksimentiev group⁸³ suggested that old parameters would interact very strongly with phosphates, resulting in unphysical configurations. With the current insights in computational power, it would be ideal to perform new replicates with different starting configurations and increase the single simulation time at least 5 times, which may change the end-to-end distances of DNA tripods. However, these changes will not affect the binding profile of the particles and the interpretation of the data presented in this thesis, as the bivalent constructs show no super-selectivity.

A more pronounced pattern-based multivalent binding behavior was observed for the DNA-origami disks. When the ligand geometry is rigid, individual bonds either fit or they do not, which is directly dependent on the surface density. Indeed, we measured a strong receptor density effect when ligand presentation was spatially constrained. The spatial tolerance of the ligand presenting architecture defines the onset of binding, with a characteristic super-selective interaction profile occurring when receptor spacing matches ligand spacing. We therefore introduce the concept of

multivalent pattern recognition (MPR) for interactions that fall in this category. The main parameter controlling MPR is the rigidity of the ligand, which controls the overall spatial tolerance of binding. A higher rigidity results in a stronger super-selective response as well as enhances the overall affinity through a reduction in the enthalpic penalty of conformational change. While first steps were made in this thesis, a closer look on the rigidity of ligands should be taken. In this thesis, six-helix bundle cross-section DNA-origami disk was used in order to have a rigid scaffold (Figure 5.1A). In the next step, a more flexible scaffold can be designed e.g. single-layer wire frame flat sheet in order to compare the affinities with the DNA-origami disk used in this thesis. Additionally, by using this less rigid scaffold ligands can be presented in different ways: i) ligand can be conjugated to the same end protrusion of staple to constrain the ligand close to the site on the DNA-origami (Figure 5.1B), ii) ligand can be presented through hybridization of handle and anti-handle ssDNAs with all nucleotides having binding partners (Figure 5.1C), or iii) unpaired ssDNA can be introduced to have more flexibility (Figure 5.1D)

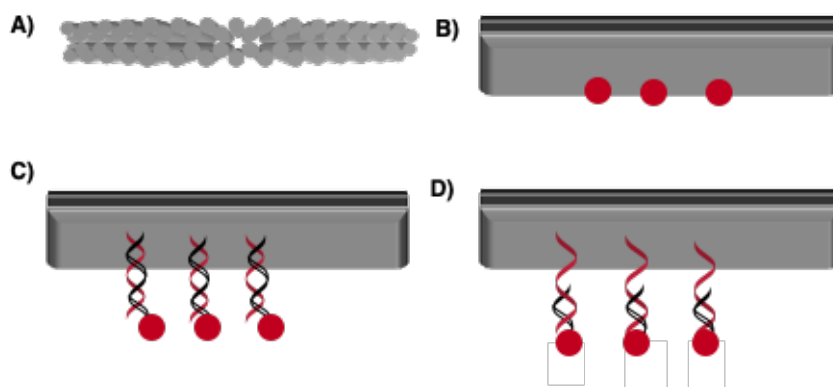


Figure 5.1. Schematic representation of six-helix bundle cross section DNA-origami disk used in this thesis. Different ligand functionalization strategies, B) when ligand is constrained to the site of DNA-origami structure. When ligand is introduced through hybridization of handle and anti-handle ssDNAs C) when all nucleotides have binding partners, and D) when non-base paired ssDNA section is introduced.

Multivalent pattern recognition in low-valency, spatially constrained materials is characterized by extreme super-selectivity. However, the balance between valency, affinity and spacing need to be carefully engineered to allow this particular phenomenon to be exploited. The significance of spatial tolerance in multivalent pattern recognition is only visible in the low-valency regime and when the difference in K_D between mono and multivalent presentation is sufficiently large. When too few or too many ligands are present, binding is either too weak or the overall avidity too strong to observe the MPR effect. Nature seems to be able to intelligently play with this concept, as seen for example in antibody arrays that can switch between 1, 2, and 5 for IgG, IgA and IgM respectively. When entering the MPR regime, materials with unique physical behavior can be designed. We believe that MPR is a fundamental phenomenon behind many natural and chemical multivalent processes, and our current findings contribute to the rational design of selective targeting with nanomaterials.

However, more experiments were required to fully explore the presence and impact of MPR in the future. In this thesis, monovalently, bivalently, and hexavalently presented ligand functionalized scaffolds were studied. However, in the next step different valencies with different patterns (Figure 5.2) on the same scaffold should be also evaluated, considering the excluded volume of the particle (disk).

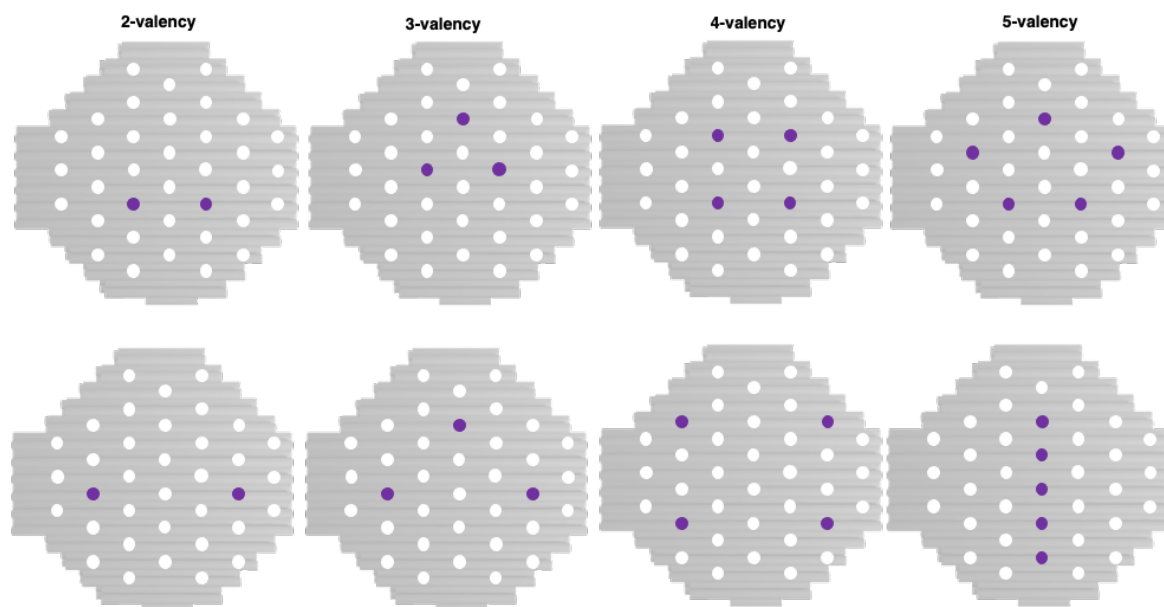


Figure 5.2. Schematic representations of DNA-origami disks with various valency and patterns.

Finally, the ideal measurements of MPR should be done on a fully controlled surface with nanometer scale precision. This would alter the multivalent binding curve to show a peak interaction at the density that perfectly matches the ligand pattern, followed by a dip in binding just afterwards, where the spacing is not matching anymore. Eventually, the global density will be sufficiently high to enter a general binding regime, but without selectivity of pattern contributions. To study the dynamic interplay between the receptors and ligands, DNA origami nanostructure (disk) can be immobilized on a SPR chip¹¹⁸ and a range of concentrations of ligand functionalized particles can be injected over the flow cell. To do so, anti-digoxigenin antibody can be immobilized on the chip, then digoxigenin modified protruded staples on oneside, and streptavidin functionalized staples on the other side of the disk can be injected. In the final step, SLLAHPQGGGC functionalized tripod can be injected over the disk immobilized surface (Figure 5.3). By using the first ligand-receptor pair used in this thesis (SA-SLLAHPQGGGC), monomeric contribution to binding affinity can be also eliminated since K_D of SLLAHPQGGG functionalized tripods is $\sim 1 \mu\text{M}$, which is ~ 60 times less than the monovalent affinity and super-specific binding behavior where the binding would only happen in a very narrow spatial window based on the tolerance of the particles can be achieved. Alternatively, an other option could be DNA origami patterning on a nanofabricated coverslip substrate patterned via electrom-beam lithography¹⁴⁹ to obtain a controlled surface with single molecule control. DNA origami nanostructure (disk) can be engineered with streptavidin and immobilized covalently on predefined locations on the substrate. All patterned substrates can be blocked by BSA prior to binding assays to reduce the nonspecific interactions and only focus on the patterned receptors. Then, these substrates can be employed as nanopatterned surface for further experiments.

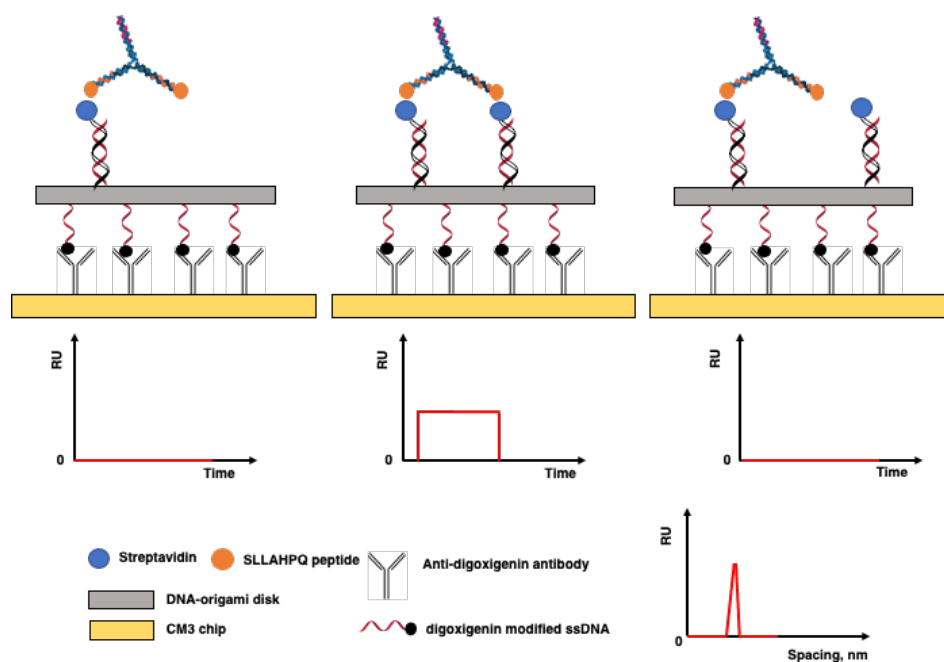


Figure 5.3. Schematic representation of ideal conditions to achieve multivalent pattern recognition (MPR), where DNA-origami structure is immobilized on SPR chip, and ligand functionalized DNA tripod is injected over the SPR chip surface.

In this thesis, it was demonstrated that multivalent pattern recognition can be achieved when target spacing falls within the spatial tolerance of the ligand presenting architectures. This concept can be adjusted to explore the potential multivalent pattern recognition in the selective targeting of cells based on the surface receptor patterns. If the molecular patterns exist in the cellular surfaces, geometrically well-defined nanomaterials can be designed with DNA nanotechnology with precise ligand presentation to study MPR. The studies in this thesis were all performed on rigid (immobile) surfaces. In the next step, selective binding behaviors of multivalent ligand presenting materials can be studied on dynamic surfaces using artificial lipid bilayers and vesicles.

Chapter 6 Appendix

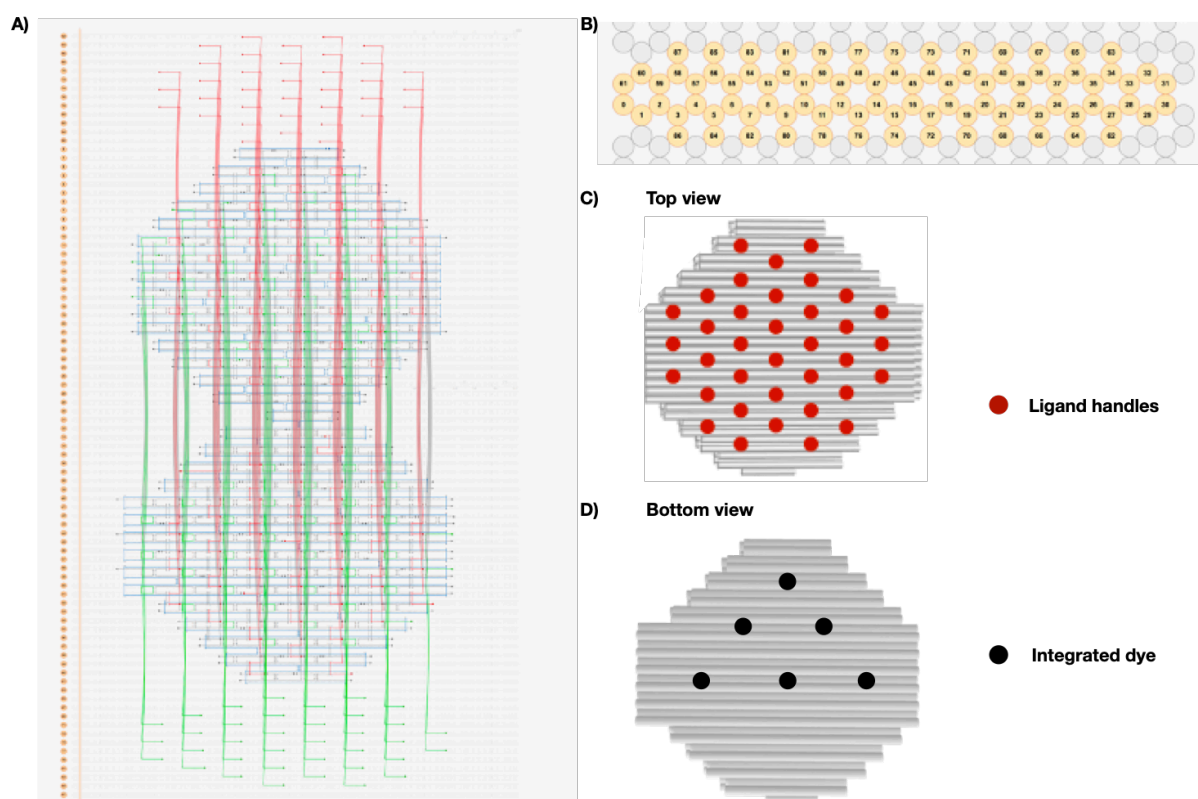


Figure 6.1. A) Cadnano file overview of DNA-origami disk with single strand extensions represented in red and green for top and bottom respectively, B) Side view of the disk, C) Top view and positions of ligand handles, D) Bottom view and positions of integrated dye.

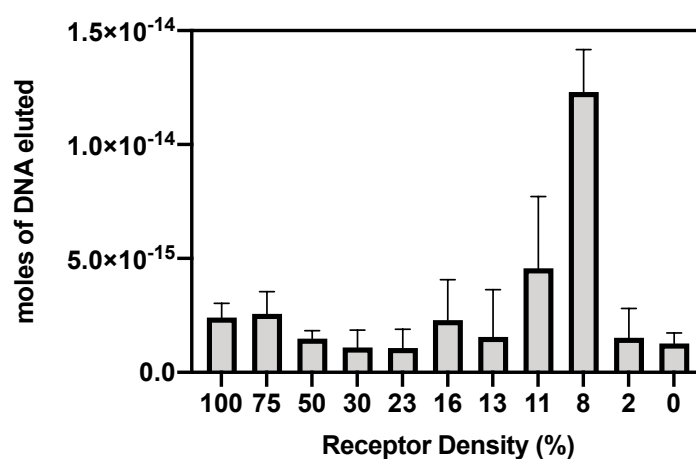


Figure 6.2. Quantification of DNA bound particles on the surfaces. Only long bivalent scaffold was tested with qPCR. Error bars represent \pm SD (n=3).

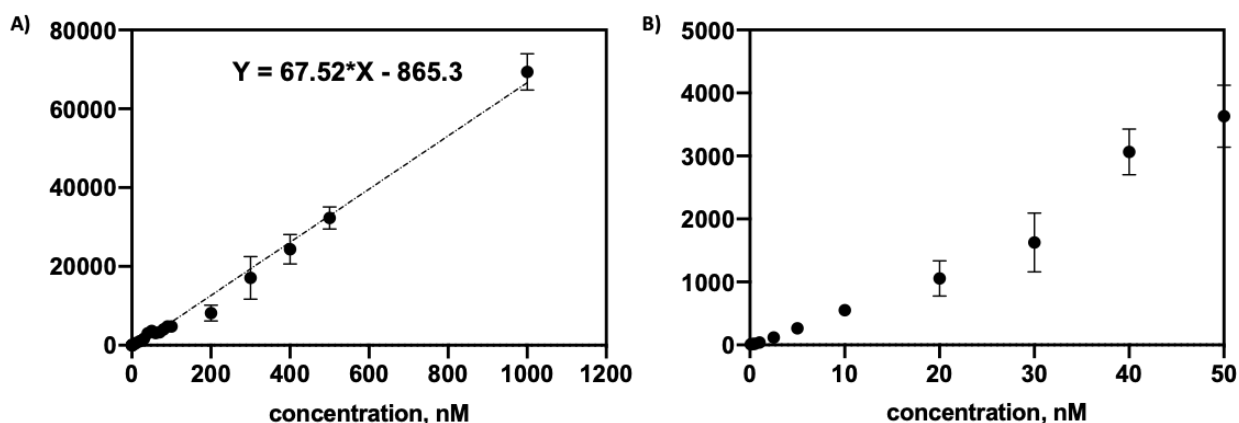


Figure 6.3. The Cy5 functionalized ssDNA sample was serially diluted to concentrations of A) 1 μ M - 100 pM and transferred to a black half area 96-wells plate to establish a calibration curve for subsequent quantification of bound particles. Fluorescence intensities of 35 μ L Cy5 conjugated ssDNA in duplicates in the respective wells on a BioTek™ Cytation 5™ Fluorescence with excitation wavelength 649/10 and emission wavelength 670/10 were measured. A calibration of Cy5 fluorescence over a concentration range of B) 50 nM - 100 pM was performed to confirm a linear relation could be assumed. Error bars represent \pm SD (n=2).

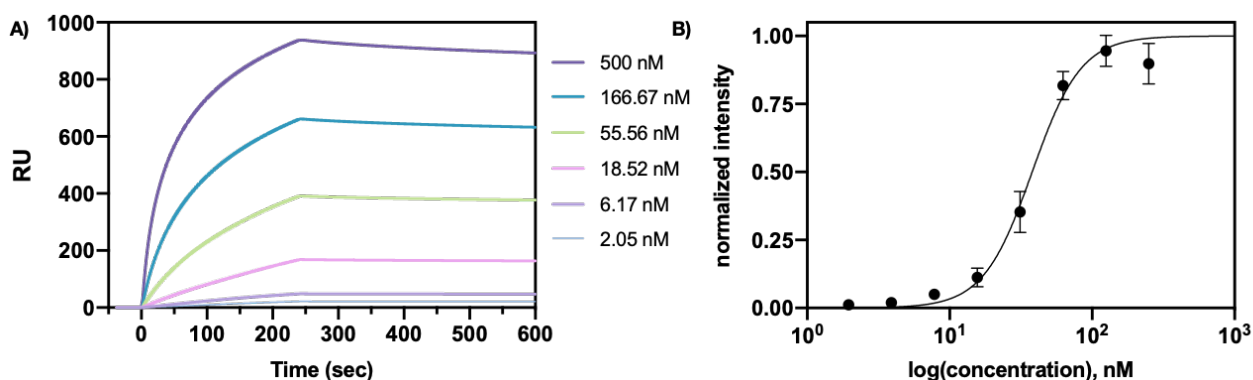


Figure 6.4. A) Biacore raw binding curve of anti-streptavidin antibody (anti-Streptavidin (DyLight488, catalog number: VC-SP-4488-MC05), showing injections of serial dilutions (500 - 2.05 nM). A multi-cycle kinetic program was used and it was carried out in triplicates. K_D value of 112 ± 3.18 nM was obtained by fitting the data to a two-site binding model. Error bars represent \pm SD (n=3).

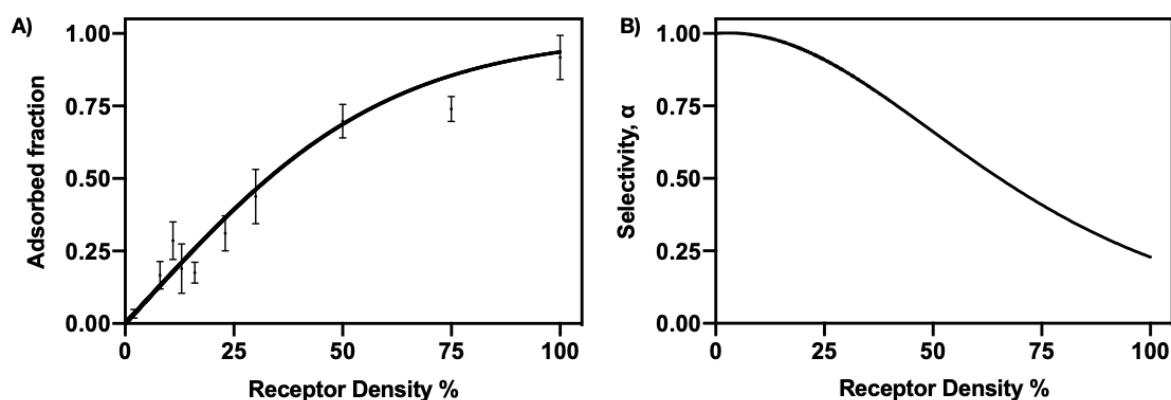


Figure 6.5. A) Solid-phase binding assay of anti-Streptavidin (DyLight488) at different surface receptor densities (in %). Data were fit using a simplified binding curve proposed by Frenkel *et al.*⁴⁸. Error bars represent \pm SD (n=5). B) The parameter α as a function of receptor density (%).

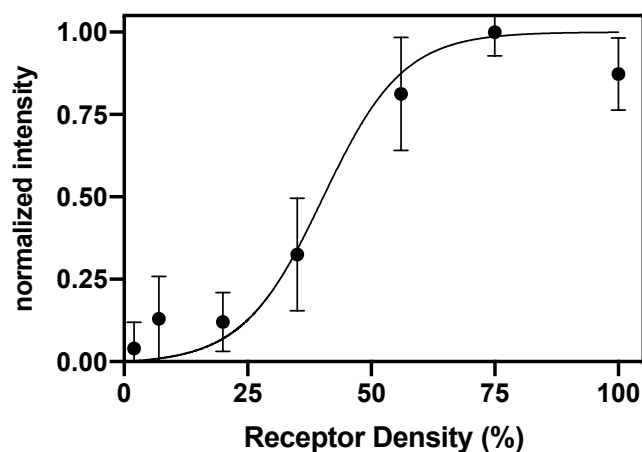


Figure 6.6. Solid-phase binding assay of biotin functionalized large hexagon design on different receptor densities (%).ST. Error bars represent \pm SD (n=5). The solid line represents the fit using a simplified binding curve proposed by Frenkel *et.al.*⁴⁸

Table 6.1. The sequences of ssDNAs used for the assembly of each bivalent construct.

<i>Name</i>	<i>Sequence</i>
Long Bivalent-1	TTCCTCTACCACCTACATCACCTAGCGTTGCTAGTGGTGTCCAAACGCTAG
Long Bivalent-2	TTCCTCTACCACCTACATCACCTAGCGTTTGGACACTCAGCCTAACGCTAG
Long Bivalent-3	CCATAGACTAGCAACTTTCACCCTAGCGTTAGGCTGACACTAGCAACGCTAG
Short Bivalent-1	TTCCTCTACCACCTACATCACCGCGCTAGCGGGGTCCACGC
Short Bivalent-2	TTCCTCTACCACCTACATCACGCGTGGACCCGCAGCCTGGC
Short Bivalent-3	CCATAGACTAGCAACTTTCACCGCCAGGCTGCCGCTAGCGCG
Flexible Bivalent-1	TTCCTCTACCACCTACATCACCGCGCTAGCGTTTTGGGTCCACGC
Flexible Bivalent-2	TTCCTCTACCACCTACATCACGCGTGGACCCTTTTGCAGCCTGGC
Flexible Bivalent-3	CCATAGACTAGCAACTTTCACCGCCAGGCTGCTTTTCGCTAGCGCG

Table 6.2. Scaffold p7560 sequence.

Sequence of scaffold p7560

AGCTTGGCACTGGCCGTCGTTTTACAACGTCGTGACTGGGAAAACCTGGCGTTACCCAACCTTAATCGCCTTGCA
GCACATCCCCCTTTTCGCCAGCTGGCGTAATAGCGAAGAGGCCCGCACCGATCGCCCTTCCCAACAGTTGCGCAG
CCTGAATGGCGAATGGCGCTTTGCTGGTTTCCGGCACCAGAAGCGGTGCCGGAAGCTGGCTGGAGTGCGATC
TTCCTGAGGCCGATACTGTCGTCGTCCCTCAAACCTGGCAGATGCACGGTTACGATGCGCCCATCTACACCAAC
GTGACCTATCCCATTACGGTCAATCCGCCGTTTGTTCACGAGAATCCGACGGGTGTTACTCGCTCACATTT
AATGTTGATGAAAGCTGGCTACAGGAAGGCCAGACGCGAATTATTTTGATGGCGTTCCTATTGGTTAAAAAAT
GAGCTGATTTAACAAAAATTTAATGCGAATTTTAAACAAATATTAACGTTTACAATTTAAATATTTGCTTATACA
ATCTTCCTGTTTTTGGGGCTTTTCTGATTATCAACCGGGGTACATATGATTGACATGCTAGTTTTACGATTACCGT
TCATCGATTCTCTTGTGTTGCTCCAGACTCTCAGGCAATGACCTGATAGCCTTTGTAGATCTCTCAAAAATAGCTA
CCCTCTCCGGCATTAAATTTATCAGCTAGAACGGTTGAATATCATATTGATGGTGATTGACTGTCTCCGGCCTTT
CTCACCTTTTGAATCTTTACCTACACATTACTCAGGCATTGCATTTAAAAATATATGAGGGTTCTAAAAATTTTAA
TCCTTGGCTTGAATAAAGGCTTCTCCCGCAAAGTATTACAGGGTCATAATGTTTTTGGTACAACCGATTAGC
TTTATGCTCGAGGCTTATTTGCTTAATTTTGCTAATTTTGCTTGCTTGCTGATGATTATTTGCTACTA
CTACTATTAGTAGAATTGATGCCACCTTTTACGCTCGCGCCCCAAATGAAAATATAGCTAAAACAGGTTATTGACC
ATTTGCGAAATGTATCTAATGGTCAAACCTAAATCTACTCGTTCGCAGAATTGGGAATCAACTGTTATATGGAAT
GAAACTTCCAGACACCGTACTTTAGTTGCATATTTAAAACATGTTGAGCTACAGCATTATATTCAGCAATTAAGC
TCTAAGCCATCCGCAAAAATGACCTCTTATCAAAAGGAGCAATTAAGGTAATCTCTAATCCTGACCTGTTGGA
GTTTGCTTCCGGTCTGGTTTCGCTTTGAAGCTCGAATTAACACGCGATATTTGAAGTCTTTCGGGCTTCCTCTAAT
CTTTTTGATGCAATCCGCTTTGCTTCTGACTATAATAGTCAGGGTAAAGACCTGATTTTTGATTTATGGTCATTCT
CGTTTTCTGAAGCTTTTAAAGCATTGAGGGGATTCAATGAATATTTATGACGATTCCGCAGTATTGGACGCTA
TCCAGTCTAAACATTTTACTATTACCCCTCTGGCAAACTCTTTTGCAAAAAGCCTCTCGCTATTTTGGTTTTTA
TCGTCGCTGGTAAACGAGGGTTATGATAGTGTGCTCTTACTATGCCTCGTAATTCCTTTTGGCGTTATGTATCT
GCATTAGTTGAATGTGGTATTCTAAATCTCAACTGATGAATCTTTCTACCTGTAATAATGTTGTTCCGTTAGTTC
GTTTTATTAACGTAGATTTTTCTTCCCAACGTCCTGACTGGTATAATGAGCCAGTTCTTAAATCGCATAAGGTA
ATTCACAATGATTAAGTTGAAATTAACCATCTCAAGCCCAATTTACTACTCGTTCTGGTGTCTCTCGTCAGGG
CAAGCCTTATTCAGTGAATGAGCAGCTTTGTTACGTTGATTGGGTAATGAATATCCGGTCTTGTCAAGATTAC
TCTTGATGAAGGTCAGCCAGCTATGCGCCTGGTCTGTACACCGTTCATCTGTCCTCTTTCAAAGTTGGTCAGT
CGGTTCCCTTATGATTGACCGTCTGCGCTCTGGTCCGGCTAAGTAACATGGAGCAGGTCGCGGATTTCGACACA
ATTTATCAGGCGATGATACAAATCTCCGTTGTACTTTGTTTCGCGCTTGGTATAATCGCTGGGGGTCAAAGATGA
GTGTTTTAGTGTATTCTTTTGCTCTTTGCTTTTAGGTTGGTGCCTTCGTAGTGGCATTACGTATTTTACCCGTTTA
ATGGAAACTTCCTCATGAAAAAGTCTTATAGTCCTCAAAGCCTCTGTAGCCGTTGCTACCCTCGTTCCGATGCTGT
CTTTCGCTGCTGAGGGTGACGATCCCGCAAAAGCGGCCTTTAACTCCCTGCAAGCCTCAGCGACCGAATATATC
GGTTATGCGTGGGCGATGGTTGTTGTCATTGTCGGCGCAACTATCGGTATCAAGCTGTTTAAAGAAATTCACCTCG
AAAGCAAGCTGATAAACCGATACAATTAAGGCTCCTTTTGGAGCCTTTTTTTTGGAGATTTTCAACGTGAAAA
AATTATTATTCGCAATTCCTTTAGTTGTTCTTTCTATTTCTACTCCGCTGAAACTGTTGAAAGTTGTTTACAAA
ATCCCATACAGAAAAATTCATTTACTAACGTCCTGGAAAGACGACAAAACTTTAGATCGTTACGCTAACTATGAGG
GCTGTCTGTGGAATGCTACAGGCGTTGTAGTTTGTACTGGTGACGAACTCAGTGTTACGGTACATGGGTTCCCTA
TTGGGCTTGCTATCCCTGAAAATGAGGGTGGTGGCTCTGAGGGTGGCGGTTCTGAGGGTGGCGGTTCTGAGGGT
GGCGGTACTAAACCTCCTGAGTACGGTGATACACCTATTCCGGGCTATACTTATATCAACCTCTCGACGGCACT
TATCCGCTGGTACTGAGCAAAAACCCGCTAATCCTAATCCTTCTCTTGAGGAGTCTCAGCCTCTTAATACTTTC
ATGTTTCAGAATAATAGGTTCCGAAATAGGCAGGGGGCATTAACTGTTTATACGGGCACTGTTACTCAAGGCAC
TGACCCCGTTAAACCTTATTACAGTACACTCCTGTATCATCAAAGCCATGTATGACGCTTACTGGAACGGTA
AATTCAGAGACTGCGCTTTCCATTCTGGCTTTAATGAGGATTTATTTGTTTGTGAATATCAAGGCCAATCGTCTG
ACCTGCCTCAACCTCCTGTCAATGCTGGCGGCGGCTCTGGTGGTGGTCTGGTGGCGGCTCTGAGGGTGGTGGCT
CTGAGGGTGGCGGTTCTGAGGGTGGCGGCTCTGAGGGAGGCGGTTCCGGTGGTGGCTCTGGTTCGGGTGATTTT
GATTATGAAAAGATGGCAAACGCTAATAAGGGGGCTATGACCGAAAATGCCGATGAAAACGCGCTACAGTCTG
ACGCTAAAGGCAAACCTTGATTCTGTCGCTACTGATTACGGTGTCTGCTATCGATGGTTTCATTGGTGACGTTTCCG
GCCTTGCTAATGGTAATGGTGCTACTGGTGATTTTGTGGCTCTAATCCCAAATGGCTCAAGTCGGTGACGGTG
ATAATTCACCTTTAATGAATAATTTCCGTCAATATTTACCTTCCCTCAATCGGTTGAATGTGCCCTTTTGT
CTTTGGCGCTGGTAAACCATATGAATTTCTATTGATTGTGACAAAATAAACTTATTCGTGGTGTCTTTGCGTTT
CTTTTATATGTTGCCACCTTTATGTATGTATTTCTACGTTTGCTAACATACTGCGTAATAAGGAGTCTTAATCAT
GCCAGTTCCTTTGGGTATTCCGTTATTATTGCGTTTCCCTCGGTTTCCCTCTGGTAACCTTTGTTCCGGCTATCTGCTTA
CTTTCTTAAAAAGGGCTTCGGTAAGATAGCTATTGCTATTTCATTGTTCTTGTCTTATTATTGGGCTTAACCTC
AATCTTGTGGGTTATCTCTCTGATATTAGCGCTCAATTACCCTCTGACTTTGTTTCAGGGTGTTCAGTTAATCTC
CCGTCTAATGCGCTTCCCTGTTTTTATGTTATTCTCTCTGTAAAGGCTGCTATTTTCATTTTTGACGTTAAACAAA
AAATCGTTTCTTATTGGATTGGGATAAATAATAGGCTGTTATTTTGTAACTGGCAAATAGGCTCTGGAAG
ACGCTCGTTAGCGTTGGTAAGATTACAGATAAAATTTGATGGTGCAAAATAGCAACTAATCTTGATTTAAG
GCTTCAAAACCTCCCGCAAGTCGGGAGGTTCTGCTAAAACGCTCGCGTTCTTAGAATACCGGATAAGCCTTCTA
TATCTGATTTGCTTGCTATTGGGCGCGGTAATGATTCTACGATGAAAATAAAAACGGCTTGCTTGTCTCGATG

Table 6.3. Core staples sequences.

<i>Number</i>	<i>Name</i>	<i>Sequence</i>
1	13[140]46[140]	ACAATGTCTTCTAAATTACGCGCGACCT
2	17[56]14[66]	CCCGAACGTTATCATTGAGGAATATCAAGCAA
3	53[44]8[41]	AAAATCAGTAGCCCATCACGCAAAAAA
4	48[118]15[118]	GAAACGCAAAAGAACGACTTAAAGGAAT
5	15[161]44[161]	GGGTTTTCTCTTCGTGAAAGAAGAGTAA
6	15[88]48[77]	GTCCGGTCAGAAAATACAATAGAACCCTTCTTCGGAACCTACAAT
7	36[107]23[118]	ATTATTAAGAATAAATCAAATAATATCCCGCTAATCGTATCAATA
8	5[130]56[119]	TGTCGCTGGCAAGTGTAATAGCCCCCTCAGAG
9	11[182]49[196]	CCCCGGGGTGACTCCCAACCTAAAACAAA
10	36[118]27[118]	GCCAACAACGCTCAGTCTGAGGCTAAAT
11	18[107]14[108]	CACGATCGCACACTAACCAGTTGAAGAG
12	44[76]49[66]	CACCCAATCCAATAGCGCATAATAATACAAAGTTAAATTCAGCG
13	28[151]22[150]	AAATATAATACTAAGCCTTCCTCATAGTAAAGATAATGCCGAGA
14	60[114]1[119]	GATGATACAGGTGCCTTGAGTAACACCCAAATCCAACGT
15	17[140]42[140]	GGTGCCGCGTGGGATATGCGAAAAGATTC
16	18[128]44[119]	ATTCCGGCACGTTCTAAAATATCTGGCGCAGACGTAAC
17	1[120]58[119]	CAAAGGCTATTAATCTGAAAGGGTTTT
18	9[119]5[129]	TTGCTGGTAATAACCCCGCTTGGGCGCCAGCAAGATCC
19	11[67]6[51]	GGGTTTGACGTTCTTTGGTAAAAGCGCCAGAAAAGGGATTTTAGACAAAA
20	23[77]36[55]	TTCATTTAACCTTGAGAAGCCAGTAATAAGAGAATATAAAGTACCGAAA
21	48[170]53[186]	AAACCACTACTCTTAAAAGCCTTTCCAGACTAACGATCTAAAGTTTAAA
22	48[160]52[150]	CTAACGTAGAAAATAAACGGGTAGTTGCCAAAAAATTC
23	27[140]33[154]	GACCCTGGTAGTAGTTGATTCCCAATAAA
24	15[30]44[22]	AAAAATCTAAAGAAACAATTACAGAGCGTCAAAAATGAAAATAAAA
25	52[97]55[87]	AATAGCAAGGCCGGGACTGTAACCGCCTAGCC
26	39[130]21[139]	AAGACCAAAAACGCGAGGCGTTCAATCAAAATATAAGC
27	3[119]1[140]	GGCGCTAGGGCGAGGAGTCCAGCGAAAAACCGTAAA
28	29[72]28[72]	AAAGCGAGAAAACTTTTCAAGCAAGACAAAGAACAAA
29	39[44]22[41]	AAATGTTGAGCTGATGAAACAAACAAA
30	46[97]17[97]	GATAACCCACCCTGAGATTAGATCGGCC
31	21[140]38[140]	AAATATTGGAGCAAGAGGGGAAATGCT
32	25[140]34[140]	TTAGAACTATTTTATAATTGCCTTAGAG
33	46[139]17[139]	GCTCCATATCATAAGGGGGATCGCTTCT

34	5[98]2[105]	TAACGTGCTTTCGCCGCTGCGAAGCGAAGGAGGGA
35	21[56]38[44]	GAATACCAGAAGATAATGCAGACGACAATAAACAACAAAA
36	46[128]50[129]	CTTGATTAAGGGCAACATTTTCATGCAAC
37	43[46]46[45]	GTTTGTTTAAAGAATAATGAA
38	42[65]19[76]	ACACATATTATTTATCCTGCATCTCATATTC
39	55[54]54[54]	AAAAGCCACGAACCAAAA
40	40[160]23[160]	AACCCTCTAAAATGATTGCCTGGAGAGG
41	42[197]43[197]	AAAATCTACAAAAAAAAA
42	23[161]37[175]	GTAGCTATGAGTAAGAACCAGACCGGAAA
43	6[172]55[175]	AAAGCTGATTGCTACCGTAACACTAAA
44	9[140]50[140]	CACAACAAAATTGTAAATCTCGCCGACA
45	11[77]8[84]	GGCCAACAGAGAATCGCTCATCACTTGCTGTAATC
46	46[44]13[55]	ATAAAAAGTAGCCAAAGGGAAGGTAAATAACGTGGCACATGCGCG
47	55[88]5[97]	GCCTCAGACGTCATTAAAGCCACCACCACACGCACGTA
48	0[140]60[115]	AAACTATCATACGTGAACCATCAGTGCCCGAACCTATTTT
49	14[65]11[66]	CAGAGCCCTAAAGCGTAAAAA
50	16[45]12[45]	TTACCATCACCCAGCAGGTCTTTAAGAC
51	40[55]43[45]	AGAACGGGTATTAACCGTTTTCTTACCAGCCA
52	30[137]27[129]	AAAATAACCTGTAAAGGTGATCCAATACCA
53	34[165]38[150]	AAATCATTTTTGCGGATGGTCCTTTTAGGATTATCGAGCTCCCC
54	49[109]52[108]	TTGCGATATATAAAGGACGGA
55	9[98]50[98]	GAAGAACTGCAACAGAACAACCTTCGGTC
56	38[139]25[139]	TTAAACATATCGCGGGGTGAGAAAATT
57	58[128]61[144]	GCGCATGAAATATTTCCGTATAAACAGTTAATGAAA
58	18[86]15[87]	ATCCGACAGTAGCCGTCTCTG
59	17[182]42[178]	CGCAACTATCAACATGGGAAGGTTAATAAAAAC
60	40[118]45[108]	AGATCCTAATTTACGGCTTATGTTTTGAGGTTAACTATTCTCAG
61	10[193]51[196]	AAACCGAGCTCGTCGGTTTATCAGAAA
62	19[172]14[171]	GCCTGAGCGACGCCATTTGCGGGCCCCAGTCTTTC
63	36[139]39[129]	CCAATCGCCATATTCTTCAAAGTTCAGAAAAG
64	46[196]17[181]	AAAGTACAACGGAGATTGTATTGAACGGCGATCGGCAGGCTG
65	25[77]34[65]	AAAACATTTGGGTTTATGCGTACTAGAAAAAGCCTGTAAA
66	56[165]7[160]	AAACGCCACCCTACCCATGCCTTCACAGTGAGA
67	54[139]58[129]	TAGCCATCTTTTCAATTTTACGCCACCGGAATAGATTA
68	21[98]38[98]	TGATAATGCATGTCACAAGAAAAAATC
69	50[97]13[97]	GCTGAGGGCAACGGTTCACATCGAACGA
70	38[86]44[87]	CTGTAGATAACAATCAAGCAAGCAATTAGTTGTAGTAAGCCC

71	24[172]19[171]	AAACCTTTTTGAAAGGCTATTGTTAATTTTTATCTG
72	52[118]11[118]	GTTTCAGATTGCGATTACCGCCTGGTT
73	10[149]3[151]	GTGTACGAGCTTAATTGTTTCACCCGCTGGGAAATCGTTATAAATGAAA
74	15[77]44[77]	ATCAATAAATAGATGAGAATTCGAGAAA
75	23[41]24[51]	AAAATCAAGAAAACAAAATTAACGCTATTAAAAA
76	46[118]49[108]	ACTGAGCGCTAATAAATACCCAAAGACAGGCT
77	43[151]47[151]	AAGAAGAACCGAACTGAGAAATCCAGTAT
78	50[196]13[181]	AAACTTGCTTTCGAGGTGAATTGAAGGCATATGATAATTTACG
79	8[107]54[98]	CGTGGGAGAGTTCTCGTTAGAATCCCACCACGAGCCAC
80	38[186]42[171]	AAACTGCGGAATCGTCATATGGATAGAGCAACATAATGCACTAA
81	50[128]9[139]	CATTTTTTCAACAACTTTATTAGCGTTTGCCTCACTGAATTCCA
82	1[83]0[104]	AAATAAAGCACTAAATCGGAACCCTAAACTCAAGTTT
83	11[161]48[161]	ACCTCGATGCGGCCCGTAATGCACTCAT
84	36[175]35[165]	AAAAAGCAAACCTCCAACAGGTCGATAAGAGGAAA
85	10[58]52[44]	ATCGAATTAGGGGATCGTCTTGACGGAAATTCTTGAGCTAAAA
86	15[151]10[150]	GGTGGATGTTCCCGCCACTGTAAGACGTGGTCTGT
87	2[151]59[154]	AAATTCCAGTTTGAGGCTGAGACTAAA
88	47[152]15[160]	GTTAGCATTCCAGGGTAACGCCA
89	33[76]29[104]	AAAAAATAAGAATAAACACCTGCAAAATTAAATATATTTTAGT
90	44[118]19[118]	AAAGCTGTTTCAACATGGGATCCTGATT
91	27[98]32[76]	CCTCAGAGAATTAGCAACTAAACCGACCGTGTGATAAATAAGGCGTTAAA
92	42[55]21[55]	CCTGAATTATTTTACCTTTTTTGCTTT
93	5[140]54[140]	TGTTTCCCCTGAGCAAGCCCACGCCTG
94	8[183]9[183]	AAAAGTGCCCTGGGAAAA
95	25[98]34[98]	TTAAGACCTTTTTACCAGTATTTTTAAA
96	23[98]18[108]	AATGGAAACAGTCCAAAACACAGAAAAATAAAGAATATAATAGGT
97	11[119]48[119]	GGTGTAATATAGGGAAGACTTTATAAAA
98	19[182]41[196]	AGCCAGCGTTAAATAACGCCAAAAGGAAA
99	44[160]19[160]	TCTTGACAACCTGGCCCCGTCGAAAAATA
100	42[170]48[171]	CGGACCAGTCTTCATCAGGACAGACATCGCCAGCGATTACTA
101	44[86]51[87]	TGAAACTGAACACAAGAGAGGAAATATTTTGGAGGGTACTTGCAGCACC
102	22[183]23[183]	AAAACACAGAGATAAAA
103	32[154]31[137]	AAATCTGCGAACGAGTAGATTTCAAAA
104	27[119]32[111]	CGGTTGTAAATCATAAGTTTCCATTAGATATGGTT
105	3[72]56[77]	AAACGGCGAACGGCTTAATTAATCCATTGGCC
106	56[76]7[76]	TTGATATGCCACCAGCCGATTATCCTGA
107	46[55]17[55]	GAAACAACATAAAAGTATTAGTCCTTTG

108	7[77]5[87]	GAAGTGTTTTTAAAGAGCTAATTGA
109	27[62]24[87]	AAAGTAAATGCTGATGCAAATCCAATCGCGCTTAGGAGCGATAAGTG
110	42[177]21[193]	GAAGATACATCAGCTCAAATTCGCATTAAATTTAAA
111	38[97]25[97]	AGGTCTTATTGCATATATGTGGCTTAGA
112	52[107]7[118]	GTGGCATTTTGAACCACAGAGCCGCCGCACCGCTGGTGCGGTTT
113	19[30]40[22]	AAAGGAACAAAGGAGAAACAAGCAAGACCAAGTACCGCACTCAAAA
114	5[88]2[72]	CGACCGCCGCTGGCGAGGCTTGACGGGGAAAGCAAA
115	21[30]16[46]	AAATAACGGATTTCGCTGAACATCGGAAACCACAACATTATATTAAAACT
116	20[66]42[56]	ACAGTTATCATGCTAATTTTAAAGAAACAGCATTTTAT
117	14[107]46[98]	ATAAAACAGAATAACGGTCAGAGA
118	8[83]52[77]	AGTGAGGAGCGTCAAAACGTC
119	19[161]40[161]	ATTCGCGACCAATAATTCAACCTATCAT
120	58[107]3[118]	GGCCATACATGGCTTATAGAACGTAGGAGCG
121	19[77]40[77]	CTGATTATAACGTCCCCAATATAATCGG
122	29[105]26[108]	TAATTTTAGGCAAAGCATAAAAGAC
123	7[119]52[119]	GCGTATTTCCAGTCAGCCCCCTTCAACA
124	21[77]18[87]	CGCAGAGGCGAATATCAGGTTTCAGATGGCGC
125	15[182]45[196]	TGTAAAAGGAAGGGTGTACAGACCAGAAA
126	17[98]42[98]	TCAGGAAGTTGGTGTGAGATAGCCTTA
127	27[130]34[119]	AAAGATCAAAATCATAGACAGTAGATAATGC
128	52[149]57[165]	TGTAGACAGCAACTACAAATAGGACAGAACCTCAGGAGGTTTAGTACAAA
129	52[76]11[76]	ACCAATGAAAATCACCTACATACATTCT
130	7[161]52[161]	CGGGCAATGAGCTAGTTAGCGGTTAGTA
131	15[119]12[129]	TGAGGAAGGTTAGCTGAATTCTTGTCAGCAC
132	58[97]60[86]	TGGAATGGAAAGCGATTTACCTAAAA
133	54[97]9[97]	CACCGGAGCGCGTTGCATTAAGTACGTA
134	40[196]39[186]	AAAAATTACGAGGCATAGTAAGCGTCCAATAAAA
135	4[162]5[162]	AAAAATCCCGCAAAAAA
136	38[149]43[150]	CTCGTAATAGGTTTACCTTTAGGAAGGTAGATTTT
137	58[154]5[139]	AAACCTCAAGAGAAGGATTAGGGTGTATCAATAGCCTTGATGG
138	29[120]33[129]	AGCTGATTAGCTAATTTGCAAATGGTAGTTTGAATTC
139	13[98]8[108]	ACCACCAGCAGATGATCGGCTCTGACCTCAGCCATTCAAACCTCTGT
140	5[62]6[81]	AAAGGCGCGTACTATGGTTGCTACA
141	57[65]4[62]	AAAACAAACAAAGCGCCGCTACAGAAA
142	56[118]58[108]	CCCAGCATTGACAGGGGTTGAACCA
143	19[119]40[119]	GTTTGGACACGTAATCTAAGATAGCGAG
144	14[170]7[172]	TCACTAATCTCCGACAGTAAAGACAATCATGGTAAAGCTAATGAGCAAAA

145	34[118]29[119]	TGTAGCTTGTCTGGACAGGCAGGGGCGCG
146	25[51]20[67]	AAATTAATTTTCCCTTAGAAAATCGTTTACATTGAGCAAAAAGTTACTAT
147	34[97]38[87]	TAGGAATCATAATTTATACAATTCGAGCAAAGCGGTACC
148	13[182]47[196]	CTCGCCCGGCCAGTGC GCGAAACAAAAA
149	2[104]58[98]	GCCCCCGTAAGCGTGGATAAG
150	9[41]10[59]	AAATTAACCGTTGTAGCAATACCTCA
151	32[110]36[108]	TGAAATAGTACGGCAACATGAAAGCCATGTA
152	34[139]29[151]	CTTAATTATAACAGCATTAAACGCATCAATTCTACTAAAAA
153	38[76]42[66]	TATCTGTCCAGACGAACGCGCTCCTTATGAATCATAGCT
154	25[119]22[129]	ATAGTGAATTTATAAAAGGCCCAACCGTGAAT
155	13[56]46[56]	AACTGATTGCCACGAGCCGAAAGAGCAA
156	42[97]21[97]	AATCAAGAATCAGATAGATTTCCCGGT
157	61[86]0[83]	AAAAGTTTTAACGTCGAGGTGCCGAAA
158	19[140]15[150]	AATGGAAGGGTTTCGATTCTCGAAACCAGCCAGCTGTTG
159	49[67]56[65]	AAACTTTTGAGCCAGCAAACCATTCAGTTACCTCACCTCAGATCAAA
160	26[162]27[162]	AAAAGGGAGTTTGCAAAA
161	0[103]60[100]	TTTGGGGGGGTGAGAGTG
162	23[119]36[119]	TGATATTGGAGACACGAAAGATAACAAC
163	40[76]23[76]	CTGTCTTCTGTTTAATTACCTTAACAAT
164	48[76]15[76]	CAATAGAACCAGAAACCGCCTACCCTCA
165	31[100]30[100]	AAACTGACCTAAATTTAACTATTTTCATTCTCTTAAA
166	35[65]26[62]	AAATTAGTATCAATATAACTATATAAA
167	50[139]13[139]	ATGACAAAGGAAGTTCGGTGGCCTTATG
168	22[128]18[129]	CGAAAGATTGTTATTTGTTATACTGCGG
169	42[139]46[129]	ATTTAGCGAACCTCATTGTGACAAATCAACGGTCAGTTA
170	52[160]11[160]	AATGAATAAGGCTCCTGTTTCGCTTGTT
171	11[30]48[22]	AAAGGCAGATTCATTTTTGGAGGGAGACAAAAGGGCGACATTA AAA
172	59[75]58[75]	AAAATCTGACAGTCAAAA

Table 6.4. Staple sequences without handle extensions.

<i>Number</i>	<i>Name</i>	<i>Sequence</i>
1	17[30]71[46]	AAAGACAACCTCGTCATTTTCTAATTTACGCTAA
2	13[30]75[46]	AAATGGCTATTACAAATGATTTTAAGGCAATAG
3	9[77]79[87]	ATAACATGGAAATACCAAGTAGGGAGTTA
4	15[140]73[150]	CGATTAAGGCGAAAGGGAACCGGATATT
5	17[77]71[87]	GGGACGAGTAACCGAGAACGAGCTATTT

6	13[119]75[130]	TGCTGAAATGCGCACTGGCATAGCCGGA
7	12[44]79[46]	AATACCAGTCATGGATTATTTACATCACCGAATTCATT
8	48[196]77[193]	AAAGAAAAGAGGCAAA
9	54[175]83[172]	AAAGAGTTTCGTCAC
10	12[128]79[130]	GAATGAGTAATCTCCAGAACAATAATAAACGCCAC
11	7[98]81[109]	ACGCGCGGCCAGCTTTCATCGAGAATAG
12	22[149]69[150]	GTCTAAATTGCAAGAACCTACCATGTTGAGAAGACGAC
13	11[140]77[150]	TTAAGCTCAACTCGTTCATTACATACA
14	3[98]85[109]	GGGAAGACGTAACCGTCGAGAGAGGTTG
15	11[98]77[109]	CCGAACCTGACGCATCTACAGACCACGGA
16	3[140]85[151]	TGAGTGTTCAAAGACCGTACGCCACCC
17	5[119]83[130]	GGCGAAACGGTCCACACCCTCTAATCAA
18	15[98]73[109]	AAATCAAACTAATAACAAAGAGTGAAT
19	15[56]73[66]	ACCTCAATTTAGAAACAGGGAAAGAAAC
20	44[196]73[193]	AAAGCGCATAGGCTG
21	17[161]71[171]	CGCCATTGTAACAATCATTATAACAACA
22	13[77]75[87]	GCCATTATATTAACGGAACCATGAGT
23	26[107]65[109]	TACGCTGAGACAACATAAATCAATCAAAAAGTAGGCAG
24	23[140]65[151]	GATAAATTTCAAAATTTAATGAGAGTA
25	6[80]83[87]	GGAGCCCTCAGCCCTCAG
26	17[119]71[130]	CAGCTTTGACCGTATTTAATCCCGACTT
27	19[56]69[66]	AGCGGAATAACAGTATCGTAGCATTCCA
28	13[161]75[171]	CCCGCTTGGAGAAGGACCCCTGATAAA
29	9[161]79[171]	ATAAAGTGTCATAGCAAAAGGCAGCTTG
30	21[119]67[130]	AAACAGGTGAACGGTTTTGCAAAACGAG
31	24[86]67[87]	AATGAATTACTGTTATTCATTCATCAACAACTATTA
32	21[161]67[171]	TAATATTTAGGTCTTTAGACAATATTC
33	11[56]77[67]	CAGTAATAGAATACCCTCAGCTATGGTT
34	7[51]81[68]	AAAGGAACGGTAAGTCTGTGACAGAACGATAGC
35	7[140]81[150]	TTTTTCTCGTTGCGATTCCACATGGGAT
36	19[98]69[109]	TTCATCAAATTGCGTATAGAAGAGCATG
37	42[160]68[149]	TTATTACATACCACGGAACGCTAAACGT
38	46[76]72[65]	TAAGCCCTAGACGGAATACATGTTTGAG
39	52[186]78[171]	AAATGTCGTCTTAATTGTAAATTCGTGGAGGAT
40	50[160]76[149]	ATACCGATAAAATACTGCCATAAATAAC
41	60[99]86[87]	TACTGGTAAGTTCCAGATTTAGAAAAGGAA
42	54[160]80[149]	CAGTACACCTCATAACTCACACGGAAGC

43	44[97]70[87]	AAGGCTTATTGGGCTAGATGGATGGCAA
44	50[118]76[108]	GCATAACAGGACTAGCCTTGATCCTTAG
45	51[88]78[87]	ATTACCATAGGGAAAAACATTTCT
46	56[97]82[87]	AGGCAGGACCAGAAAAGACGGTTCGGCCA
47	33[130]62[129]	CATGCTGAATGGCTTAATTGAGTTACGCAAGACATTAT
48	45[109]72[108]	AGGGTAATGATTAGGAGCTCCAGC
49	38[118]64[108]	AATGACCGGAAGCCGTCAAATAGAGTCA
50	54[118]80[107]	AATCACCCGGTCATGGGAAACATCGGCC
51	52[55]78[44]	AGCACCGCATTTGGGTCTGAAACACGAC
52	48[97]74[87]	ATAAGTTCGCAATAGGTGAGGAGTTGGC
53	52[139]78[128]	TTTGCTAACGTTGATATCCGCACAGGGC
54	44[181]70[171]	GCTGACCAGGACGTTTAAATGTTCTGT
55	60[144]86[127]	AAACCCCTGCCGTATTAAGGAACAAATAGGGT
56	36[97]62[87]	AGGCATTATTCTTAACCTCCGAATAAAG
57	38[160]64[150]	ATTGAATTCAAAGCTGTGTAGTATTTTA
58	44[55]70[44]	GATTTTTACAAAATTTTGAGTCAGAAGG
59	54[76]80[65]	AGCCGCCTGCCTTTCCACCGAATTAGTA
60	48[139]74[128]	TAAAGGTACTCCTTGTGGTTGTGCAAGG
61	46[160]72[149]	TTGTGTCCCACTTCTATTACGGCAAAG
62	58[118]84[107]	GCTCAGTTATAAGTGCGGTCACCCAGCA
63	48[55]74[44]	TACCAGCAGCAGATCTGAGAGTTGCTGA
64	42[76]68[65]	TGCACCCTACCGCGAGATGAAAAAATCG
65	37[55]64[65]	AAAACAAAAGGTAAAGTAATGTCTTCTGTATCCTTG
66	44[139]70[129]	CATTACCATTACCTACAAACGTCTGAAT
67	40[139]66[129]	GATAAAATTTTGCCAACAAGATCTAGCT
68	56[139]82[128]	TCAGAACGGGATAGAGAGTTGAGGGTGG
69	40[97]66[87]	TAGAAACGTCCTGAAATCATACTTTTTT
70	50[76]76[65]	AAGGCCGGACAGCAGACCTGAAAACATC
71	42[118]68[107]	GCGGGAGCCGGTATAACAGAAGCCCCAA
72	48[181]74[171]	AGAATACATACCAAGCCAAGCACGACGT
73	42[160]68[149]	TTATTACATACCACGGAACGCTAAACGT
74	46[76]72[65]	TAAGCCCTAGACGGAATACATGTTTGAG
75	52[186]78[171]	AAATGTCGTCTTAATTGTAAATTCGTGGAGGAT
76	50[160]76[149]	ATACCGATAAAATACTGCCATAAATAAC
77	60[99]86[87]	TACTGGTAAGTTCCAGATTTAGAAAAGGAA
78	54[160]80[149]	CAGTACACCTCATAACTCACACGGAAGC
79	44[97]70[87]	AAGGCTTATTGGGCTAGATGGATGGCAA

80	50[118]76[108]	GCATAACAGGACTAGCCTTGATCCTTAG
81	51[88]78[87]	ATTACCATAGGGAAAAACATTCT
82	56[97]82[87]	AGGCAGGACCAGAAAGAGCGGTGCGCCA
83	33[130]62[129]	CATGCTGAATGGCTTAATTGAGTTACGCAAGACATTAT
84	45[109]72[108]	AGGGTAATGATTAGGAGCTCCAGC
85	38[118]64[108]	AATGACCGGAAGCCGTCAAATAGAGTCA
86	54[118]80[107]	AATCACCCGGTCATGGGAAACATCGGCC
87	52[55]78[44]	AGCACCGCATTTGGGTCTGAAACACGAC
88	48[97]74[87]	ATAAGTTCGCAATAGGTGAGGAGTTGGC
89	52[139]78[128]	TTTGCTAACGTTGATATCCGCACAGGGC
90	44[181]70[171]	GCTGACCAGGACGTTTAAATGTTCTGT
91	60[144]86[127]	AAACCCCTGCCGTATTAAGGAACAAATAGGGT
92	36[97]62[87]	AGGCATTATTCTTAACCTCCGAATAAAG
93	38[160]64[150]	ATTGAATTCAAAGCTGTGTAGTATTTTA
94	44[55]70[44]	GATTTTACAAAATTTTGAGTCAGAAGG
95	54[76]80[65]	AGCCGCCTGCCTTTCCACCGAATTAGTA
96	48[139]74[128]	TAAAGGTACTCCTTGTGGTTGTGCAAGG
97	46[160]72[149]	TTGTGTCCCACTTCTATTACGGCAAAG
98	58[118]84[107]	GCTCAGTTATAAGTGCGGTCACCCAGCA
99	48[55]74[44]	TACCAGCAGCAGATCTGAGAGTTGCTGA
100	42[76]68[65]	TGCACCTACC GCGAGATGAAAAAATCG
101	37[55]64[65]	AAAACAAAAGGTAAAGTAATGTCTTCTGTATCCTTG
102	44[139]70[129]	CATTACCATTACCTACAAACGTCTGAAT
103	40[139]66[129]	GATAAAATTTTGCCAACAAGATCTAGCT
104	56[139]82[128]	TCAGAACGGGATAGAGAGTTGAGGGTGG
105	40[97]66[87]	TAGAAACGTCTGAAATCATACTTTTTT
106	50[76]76[65]	AAGGCCGGACAGCAGACCTGAAAACATC
107	42[118]68[107]	GCGGGAGCCGGTATAACAGAAGCCCCAA
108	48[181]74[171]	AGAATACATACCAAGCCAAGCACGACGT

Table 6.5. Staples sequences for integrated dye. The sequences were ordered with Cy5 modification. The corresponding sequences in Table 6.4 were substituted during folding with the sequences below.

<i>Number</i>	<i>Name</i>	<i>Sequence</i>
5	Cy5_17[77]71[87]	GGGACGAGTAACCGAGAACGAGCTATTT
13	Cy5_11[140]77[150]	TTAAGCTCAACTCGTTCCATTACATACA
15	Cy5_11[98]77[109]	CCGAAGTACGCATCTACAGACCACGGA

17	Cy5_5[119]83[130]	GGCGAAACGGTCCACACCCTCTAATCAA
21	Cy5_17[161]71[171]	CGCCATTGTAACAATCATTATAACAACA
26	Cy5_17[119]71[130]	CAGCTTTGACCGTATTTAATCCCGACTT

Table 6.6. Staples sequences for large hexagon design. The corresponding sequences in Table 6.4 were substituted during folding with the sequences below.

<i>Number</i>	<i>Name</i>	<i>Sequence</i>
74	46[76]72[65]	TAAGCCCTAGACGGAATACATGTTTGAGTTCCTCTACCACCTACATCAC
82	56[97]82[87]	AGGCAGGACCAGAAAGAGCGGTCGGCCATTCTCTACCACCTACATCAC
83	33[130]62[129]	CATGCTGAATGGCTTAATTGAGTTACGCAAGACATTATTTCTCTACCACCTACATCAC
92	36[97]62[87]	AGGCATTATTCTTAACCTCCGAATAAAGTTCCTCTACCACCTACATCAC
97	46[160]72[149]	TTGTGTCCCAACTTCTATTACGGCAAAGTTCCTCTACCACCTACATCAC
104	56[139]82[128]	TCAGAACGGGATAGAGAGTTGAGGGTGGTTCCTCTACCACCTACATCAC

Table 6.7. Staples sequences for small hexagon design. The corresponding sequences in Table 6.4 were substituted during folding with the sequences below.

<i>Number</i>	<i>Name</i>	<i>Sequence</i>
79	44[97]70[87]	AAGGCTTATTGGGCTAGATGGATGGCAATTCCTCTACCACCTACATCAC
80	50[118]76[108]	GCATAACAGGACTAGCCTTGATCCTTAGTTCCTCTACCACCTACATCAC
88	48[97]74[87]	ATAAGTTCGCAATAGGTGAGGAGTTGGCTTCCTCTACCACCTACATCAC
96	48[139]74[128]	TAAAGGTACTCCTTGTTGTGCAAGGTCCTCTACCACCTACATCAC
102	44[139]70[129]	CATTACCATTACCTACAAACGTCTGAATTTCTCTACCACCTACATCAC
107	42[118]68[107]	GCGGGAGCCGGTATAACAGAAGCCCCAATTCCTCTACCACCTACATCAC

Table 6.8. Single strand extension sequence for flexible design.

TTCCTCTACCACCTACATCACTTTTCATGTCAGGAGATTTT

Table 6.9. Staple sequences for 1x (1 handle) design. The corresponding sequences in Table 6.4 were substituted during folding with the sequences below.

<i>Number</i>	<i>Name</i>	<i>Sequence</i>
96	48[139]74[128]	TAAAGGTACTCCTTGTTGTGCAAGGTCCTCTACCACCTACATCAC

Table 6.10. Reporter strand sequence for qPCR measurements.

TTCCTCTACCACCTACATCACTTTTACAACGTCGTGACTGGGAAAACCGGTGAAAGTTGCTAGTCTATGG
--

Chapter 7 References

1. Carlo Fasting, Christoph A. Schalley, Marcus Weber, Oliver Seitz, Stefan Hecht, Beate Koksche, Jens Darnedde, Christina Graf, Ernst-Walter Knapp, A. & Haag, R. Multivalency as a chemical organization and action principle. *Angew. Rev.* **51**, 19472–10498 (2012).
2. Velcro Brands. Textile Hook & Loop Fasteners. (2022). Available at: <https://www.velcro.com/business/products/textile-hook-and-loop/>.
3. Kiessling, L. L., Gestwicki, J. E. & Strong, L. E. Synthetic multivalent ligands as probes of signal transduction. *Angew. Chemie - Int. Ed.* **45**, 2348–2368 (2006).
4. Ammar Arsiwala, Ana Castro, Steven Frey, Mark Stathos, and R. S. K. Designing multivalent ligands to control biological interactions: From vaccines and cellular effectors to targeted drug delivery. *Chem. An Asian J.* **14**, 244–255 (2019).
5. Mathai Mammen, Seok-Ki Choi, and G. M. W. ChemInform Abstract: Polyvalent Interactions in Biological Systems: Implications for Design and Use of Multivalent Ligands and Inhibitors. *Angew. Chemie - Int. Ed.* **37**, 2754–2794 (1998).
6. Jun Lan, Jiwan Ge, Jinfang Yu, Sisi Shan, Huan Zhou, Shilong Fan, Qi Zhang, Xuanling Shi, Qisheng Wang, L. Z. & X. W. Structure of the SARS-CoV-2 spike receptor-binding domain bound to the ACE2 receptor. *Nature* **581**, 215–220 (2020).
7. Sebastian Fiedler. What are neutralizing antibodies – the immune system’s superheroes. (2020). Available at: <https://www.fluidic.com/resources/What-are-neutralizing-antibodies/>. (Accessed: 4th August 2021)
8. Feng, Y. & Mrksich, M. The synergy peptide PHSRN and the adhesion peptide RGD mediate cell adhesion through a common mechanism. *Biochemistry* **43**, 15811–15821 (2004).
9. Motshwene, P. G. *et al.* An Oligomeric Signaling Platform formed by the toll-like receptor signal transducers MyD88 and IRAK-4. *J. Biol. Chem.* **284**, 25404–25411 (2009).
10. Ohto, U., Ishida, H., Shimizu, T. RCSB. *Crystal structure of horse TLR9 in complex with two DNAs (CpG DNA and TCGCAC DNA)* (2017). doi:DOI: 10.2210/pdb5Y3J/pdb
11. Alice Comberlato, Marianna M. Koga, Simone Nüssing, Ian A. Parish & Bastings, M. M. C. Spatially Controlled Activation of Toll-Like Receptor 9 with DNA-Based Nanomaterials. *Nano Lett.*
12. R. Houston Thompson, M.D., James P. Allison, Ph.D., and Eugene D. Kwon, M. . Anti-cytotoxic T lymphocyte antigen-4 (CTLA-4) immunotherapy for the treatment of prostate cancer. *Urol. Oncol.* **24**, 442–447 (2006).

13. Alegre, M. L., Frauwirth, K. A. & Thompson, C. B. T-cell regulation by CD28 and CTLA-4. *Nat. Rev. Immunol.* **1**, 220–228 (2001).
14. Samir, P. & Kanneganti, T. D. Hidden Aspects of Valency in Immune System Regulation. *Trends Immunol.* **40**, 1082–1094 (2019).
15. Michele W L Teng, Edward P Bowman, Joshua J McElwee, Mark J Smyth, Jean-Laurent Casanova, A. M. C. D. J. C. IL-12 and IL-23 cytokines: from discovery to targeted therapies for immune-mediated inflammatory diseases. *Nat. Med.* **21**, 719–729 (2015).
16. Wilson, A. & Stanfield, R. L. Antibody-antigen interactions. 113–118 (1993).
17. Reynolds, M. & Pérez, S. Thermodynamics and chemical characterization of protein-carbohydrate interactions: The multivalency issue. *Comptes Rendus Chim.* **14**, 74–95 (2011).
18. Erlendsson, S. & Teilum, K. Binding Revisited—Avidity in Cellular Function and Signaling. *Front. Mol. Biosci.* **7**, 1–13 (2021).
19. Gideon Schreiber & Alan R. Fersht. Rapid, electrostatically assisted association of proteins. *Nat. Struct. Mol. Biol.* **3**, 427–431 (1996).
20. Jakob Dogan, Stefano Gianni, P. J. The binding mechanisms of intrinsically disordered proteins. *Phys. Chem. Chem. Phys.* **16**, 6323–6331 (2014).
21. Pollard, T. D. MBOC technical perspective: A guide to simple and informative binding assays. *Mol. Biol. Cell* **21**, 4061–4067 (2010).
22. Gill, S. J. *Thermodynamics of ligand binding to proteins. Pure and Applied Chemistry* **61**, (1989).
23. Mulder, A., Huskens, J. & Reinhoudt, D. N. Multivalency in supramolecular chemistry and nanofabrication. *Org. Biomol. Chem.* **2**, 3409–3424 (2004).
24. Martinez-Veracoechea, F. J. & Leunissen, M. E. The entropic impact of tethering, multivalency and dynamic recruitment in systems with specific binding groups. *Soft Matter* **9**, 3213–3219 (2013).
25. Nangreave, J., Yan, H. & Liu, Y. DNA nanostructures as models for evaluating the role of enthalpy and entropy in polyvalent binding. *J. Am. Chem. Soc.* **133**, 4490–4497 (2011).
26. Kiran, P. *et al.* Exploring Rigid and Flexible Core Trivalent Sialosides for Influenza Virus Inhibition. *Chem. - A Eur. J.* **24**, 19373–19385 (2018).
27. Aghebat Rafat, A., Sagredo, S., Thalhammer, M. & Simmel, F. C. Barcoded DNA origami structures for multiplexed optimization and enrichment of DNA-based protein-binding cavities. *Nat. Chem.* **12**, 852–859 (2020).

-
28. Chittasupho, C. Multivalent ligand: Design principle for targeted therapeutic delivery approach. *Ther. Deliv.* **3**, 1171–1187 (2012).
 29. Dower SK, Titus JA, Delisi C, S. D. Mechanism of binding of multivalent immune complexes to Fc receptors. 2. Kinetics of binding. *Biochemistry* **20**, 6335–6340 (1981).
 30. Edward A. Sykes, Juan Chen, Gang Zheng, and W. C. W. C. Investigating the Impact of Nanoparticle Size on Active and Passive Tumor Targeting Efficiency. *ACS Nano* **8**, 5696–5706 (2014).
 31. Silvia Muro, Carmen Garnacho, Julie A Champion, John Leferovich, Christine Gajewski, Edward H Schuchman, Samir Mitragotri, V. R. M. Control of Endothelial Targeting and Intracellular Delivery of Therapeutic Enzymes by Modulating the Size and Shape of ICAM-1-targeted Carriers. *Mol. Ther.* **16**, 1450–1458 (2008).
 32. Davis, M. E., Chen, Z. & Shin, D. M. Nanoparticle therapeutics: An emerging treatment modality for cancer. *Nat. Rev. Drug Discov.* **7**, 771–782 (2008).
 33. Cuesta AM, Sainz-Pastor N, Bonet J, O. & B, A.-V. L. Multivalent antibodies. when design surpasses evolution. *Trends Biotechnol.* **28**, 355–362 (2010).
 34. Yariv Mazor, Kris F. Sachsenmeier, Chunying Yang, Anna Hansen, Jessica Filderman, Kathy Mulgrew, H. W. & W. F. D. Enhanced tumor-targeting selectivity by modulating bispecific antibody binding affinity and format valence. *Sci. Rep.* **7**, (2017).
 35. K.G. Reuter, J.L. Perry, D. Kim, J.C. Luft, R. Liu, J. M. D. Targeted PRINT Hydrogels: The Role of Nanoparticle Size and Ligand Density on Cell Association, Biodistribution, and Tumor Accumulation. *Nano Lett.* **15**, 6371–6378 (2015).
 36. Kathrin Abstiens, Manuel Gregoritz, and A. M. G. Ligand Density and Linker Length are Critical Factors for Multivalent Nanoparticle–Receptor Interactions. *Appl. Mater. Interfaces* **11**, 1311–1320 (2019).
 37. Tomonori Shiokawa, Yoshiyuki Hattori, Kumi Kawano, Yukino Ohguchi, Hiroko Kawakami, Kazunori Toma, Y. M. Effect of polyethylene glycol linker chain length of folate-linked microemulsions loading aclacinomycin A on targeting ability and antitumor effect in vitro and in vivo. *Clin. Cancer Res.* **11**, 2018–2025 (2005).
 38. Leo Y. T. Chou, K. M. and W. C. W. C. Strategies for the intracellular delivery of nanoparticles. *Chem. Rev.* **40**, 233–245 (2011).
 39. B. Pelaz, C. Alexiou, R.A. Alvarez-Puebla, F. Alves, A.M. Andrews, S. Ashraf, L. P. *et al.* Diverse Applications of Nanomedicine. *ACS Nano* **11**, 2313–2381 (2017).

40. Dai, Q. *et al.* Particle Targeting in Complex Biological Media. *Adv. Healthc. Mater.* **7**, (2018).
41. Jun WooKim, J. R. C. Targeting ligand–receptor interactions for development of cancer therapeutics. *Curr. Opin. Chem. Biol.* **38**, 62–69 (2017).
42. Jonathan Wang, Jacqueline J. Masehi-Lano, E. J. C. Peptide and antibody ligands for renal targeting: nanomedicine strategies for kidney disease. *Biomaterials* **5**, 1450–1459 (2017).
43. T. Dvir, M. Bauer, A. Schroeder, J.H. Tsui, D.G. Anderson, R. Langer, R. Liao, D. S. & Kohane. Nanoparticles Targeting the Infarcted Heart. *Nano Lett.* **11**, 4411–4414 (2011).
44. Woythe, L., Tito, N. B. & Albertazzi, L. A quantitative view on multivalent nanomedicine targeting. *Adv. Drug Deliv. Rev.* **169**, 1–21 (2021).
45. Z. Cheng, A. Al Zaki, J.Z. Hui, V.R. Muzykantov, A. T. Multifunctional Nanoparticles: Cost Versus Benefit of Adding Targeting and Imaging Capabilities. *Science (80-.).* **338**, (2012).
46. Levine, P. M., Carberry, T. P., Holub, J. M. & Kirshenbaum, K. Crafting precise multivalent architectures. *Medchemcomm* **4**, 493–509 (2013).
47. Zhe Zhou, Pablo Cironi, Alison J. Lin, Yangqing Xu, Siniša Hrvatin, David E. Golan, Pamela A. Silver, Christopher T. Walsh†, and J. Y. Selective Tumor Cell Targeting Using ARTICLE Low-Affinity, Multivalent Interactions. *Am. J. Chem. Biol.* **2**, 337–346 (2007).
48. Martinez-Veracoechea, F. J. & Frenkel, D. Designing super selectivity in multivalent nano-particle binding. *Proc. Natl. Acad. Sci. U. S. A.* **108**, 10963–10968 (2011).
49. Dubacheva, G. V. *et al.* Superselective targeting using multivalent polymers. *J. Am. Chem. Soc.* **136**, 1722–1725 (2014).
50. Dubacheva, G. V., Curk, T., Auzély-Velty, R., Frenkel, D. & Richter, R. P. Designing multivalent probes for tunable superselective targeting. *Proc. Natl. Acad. Sci. U. S. A.* **112**, 5579–5584 (2015).
51. Nathan W. Schmidt, Fan Jin, Roberto Lande, Tine Curk, Wujing Xian, Calvin Lee, Loredana Frasca, Daan Frenkel, Jure Dobnikar, M. G. and G. C. L. W. liquid-crystalline ordering of antimicrobial peptide dna complexes coltrolls TLR9 activation. *Nat. Mater.* **14**, 696–100 (2015).
52. Wang, J., Min, J., Egtesadi, S. A., Kane, R. S. & Chilkoti, A. Quantitative Study of the Interaction of Multivalent Ligand-Modified Nanoparticles with Breast Cancer Cells with Tunable Receptor Density. *ACS Nano* **14**, 372–383 (2020).
53. Scheepers, M. R. W., IJzendoorn, L. J. va. & Prins, M. W. J. Multivalent weak interactions enhance selectivity of interparticle binding. *Proc. Natl. Acad. Sci. U. S. A.* **117**, 22690–22697 (2020).

-
54. Overeem, N. J. *Multivalent and dynamic interactions at lipid membrane interfaces of the influenza virus*.
 55. Liu, M. *et al.* Combinatorial entropy behaviour leads to range selective binding in ligand-receptor interactions. *Nat. Commun.* **11**, (2020).
 56. Deci, M. B., Liu, M., Dinh, Q. T. & Nguyen, J. Precision engineering of targeted nanocarriers. *Wiley Interdiscip. Rev. Nanomedicine Nanobiotechnology* **10**, 1–18 (2018).
 57. Zhang, F., Nangreave, J., Liu, Y. & Yan, H. Structural DNA nanotechnology: State of the art and future perspective. *J. Am. Chem. Soc.* **136**, 11198–11211 (2014).
 58. J.D. Watson, F. H. C. C. No Title. *The Structure of DNA* (1953).
 59. Cathal J. Kearney ,* Christopher R. Lucas , Fergal J. O'Brien, and C. E. C. DNA Origami: Folded DNA-Nanodevices That Can Direct and Interpret Cell Behavior. *Adv. Mater.* **28**, 5509–5524 (2016).
 60. Seeman, N. C. Nucleic acid junctions and lattices. *J. Theor. Biol.* **99**, 237–247 (1982).
 61. Chen, Y. J., Groves, B., Muscat, R. A. & Seelig, G. DNA nanotechnology from the test tube to the cell. *Nat. Nanotechnol.* **10**, 748–760 (2015).
 62. Goodman, R. P. *et al.* Rapid Chiral Assembly of Rigid DNA Building Blocks for Molecular Nanofabrication. *Science (80-.)*. **310**, 1661 LP – 1665 (2005).
 63. Shih, W. M., Quispe, J. D. & Joyce, G. F. A 1.7-kilobase single-stranded DNA that folds into a nanoscale octahedron. *Nature* **427**, 618–621 (2004).
 64. He, Y. *et al.* Hierarchical self-assembly of DNA into symmetric supramolecular polyhedra. *Nature* **452**, 198–201 (2008).
 65. Rothemund, P. W. K. Folding DNA to create nanoscale shapes and patterns. *Nature* **440**, 297–302 (2006).
 66. Douglas, S. M. *et al.* Self-assembly of DNA into nanoscale three-dimensional shapes. *Nature* **459**, 414–418 (2009).
 67. Andersen, E. S. *et al.* Self-assembly of a nanoscale DNA box with a controllable lid. *Nature* **459**, 73–76 (2009).
 68. Seeman, N. C. DNA nanotechnology. *Mater. Today* **6**, 24–29 (2003).
 69. Winfree, E., Liu, F., Wenzler, L. A. & Seeman, N. C. Design and self-assembly of two-dimensional DNA crystals. *Nature* **394**, 539–544 (1998).
 70. Chenxiang Lin, Yan Liu Dr., Sherri Rinker, H. Y. P. D. DNA Tile Based Self-Assembly: Building Complex Nanoarchitectures. *Chem Phys Chem* **7**, 1641–1647 (2006).
 71. Wang, Y., Baars, I., Fördös, F. & Högberg, B. Clustering of Death Receptor for Apoptosis Using Nanoscale

- Patterns of Peptides. *ACS Nano* **15**, 9614–9626 (2021).
72. Qinqin Hu, Hua Li, Lihua Wang, Hongzhou Gu, and C. F. DNA Nanotechnology-Enabled Drug Delivery Systems. *Chem. Rev.* **119**, 6459–6506 (2019).
 73. Henry, S. J. W. & Stephanopoulos, N. Functionalizing DNA nanostructures for therapeutic applications. *Wiley Interdiscip. Rev. Nanomedicine Nanobiotechnology* 1–21 (2021). doi:10.1002/wnan.1729
 74. Tian, T. *et al.* Targeted Imaging of Brain Tumors with a Framework Nucleic Acid Probe. *ACS Appl. Mater. Interfaces* **10**, 3414–3420 (2018).
 75. Cremers, G. A. O. *et al.* Determinants of Ligand-Functionalized DNA Nanostructure–Cell Interactions. (2021).
 76. Ma, W. *et al.* An Intelligent DNA Nanorobot with in vitro enhanced protein lysosomal degradation of HER2. *Nano Lett.* **19**, 4505–4517 (2019).
 77. Dietz, H., Douglas, S. M. & Shih, W. M. Folding DNA into twisted and curved nanoscale shapes. *Science (80-. J.)* **325**, 725–730 (2009).
 78. Liese, S. & Netz, R. R. Influence of length and flexibility of spacers on the binding affinity of divalent ligands. *Beilstein J. Org. Chem.* **11**, 804–816 (2015).
 79. Mohri, K. *et al.* Design and development of nanosized DNA assemblies in polypod-like structures as efficient vehicles for immunostimulatory cpg motifs to immune cells. *ACS Nano* **6**, 5931–5940 (2012).
 80. Nishikawa, M. *et al.* Biodegradable CpG DNA hydrogels for sustained delivery of doxorubicin and immunostimulatory signals in tumor-bearing mice. *Biomaterials* **32**, 488–494 (2011).
 81. Yang, M. & Millar, D. P. Conformational flexibility of three-way DNA junctions containing unpaired nucleotides. *Biochemistry* **35**, 7959–7967 (1996).
 82. Molecular Dynamics Studio. (2019). Available at: <https://sourceforge.net/projects/moleculardynami/>.
 83. The Aksimentiev Group. Theoretical and Computational Research at the Interface of Physics, Biology, and Nanotechnolog. Available at: <http://bionano.physics.illinois.edu/nanoengineer2pdb>.
 84. Thomas J. Macke, W.A. Svrcek-Seiler, Russell A. Brown, and D. A. C. Nucleic Acid Builder. *The Scripps Research Institute, La Jolla, CA* (1996). doi:<https://citeseerx.ist.psu.edu/viewdoc/download?doi=10.1.1.460.7407&rep=rep1&type=pdf>
 85. Spoel, V. GROMACS 2019. (2022).
 86. Maier, J. A., Martinez, C., Kasavajhala, K., Wickstrom, L., Hauser, K., Simmerling, C. ff14SB: Improving the accuracy of protein side chain and backbone parameters from ff99SB. *J. Chem. Theory Comput.* **11**, 3696–

- 3713 (2015).
87. Ivani, I. *et al.* Parmbsc1: A refined force field for DNA simulations. *Nat. Methods* **13**, 55–58 (2015).
 88. Joung, I. S. & Cheatham, T. E. Determination of alkali and halide monovalent ion parameters for use in explicitly solvated biomolecular simulations. *J. Phys. Chem. B* **112**, 9020–9041 (2008).
 89. Berendsen, H. J. C., Grigera, J. R. & Straatsma, T. P. The missing term in effective pair potentials. *J. Phys. Chem.* **91**, 6269–6271 (1987).
 90. Beveridge, D. L. *et al.* Molecular dynamics simulations of the 136 unique tetranucleotide sequences of DNA oligonucleotides. I. Research design and results on d(CpG) steps. *Biophys. J.* **87**, 3799–3813 (2004).
 91. Dixit, S. B. *et al.* Molecular dynamics simulations of the 136 unique tetranucleotide sequences of DNA oligonucleotides. II: Sequence context effects on the dynamical structures of the 10 unique dinucleotide steps. *Biophys. J.* **89**, 3721–3740 (2005).
 92. Lavery, R. *et al.* A systematic molecular dynamics study of nearest-neighbor effects on base pair and base pair step conformations and fluctuations in B-DNA. *Nucleic Acids Res.* **38**, 299–313 (2009).
 93. Bussi, G., Donadio, D. & Parrinello, M. Canonical sampling through velocity rescaling. *J. Chem. Phys.* **126**, (2007).
 94. Shūichi Nosé. A molecular dynamics method for simulations in the canonical ensemble. *Mol. Phys.* 225–268 (1983). doi:/doi.org/10.1080/00268978400101201
 95. Berendsen, H. J. C., Postma, J. P. M., Van Gunsteren, W. F., Dinola, A. & Haak, J. R. Molecular dynamics with coupling to an external bath. *J. Chem. Phys.* **81**, 3684–3690 (1984).
 96. Hess, B., Bekker, H., Berendsen, H. J. C. & Fraaije, J. G. E. M. LINCS: A Linear Constraint Solver for molecular simulations. *J. Comput. Chem.* **18**, 1463–1472 (1997).
 97. Eklund, A. S., Comberlato, A., Parish, I. A., Jungmann, R. & Bastings, M. M. C. Quantification of Strand Accessibility in Biostable DNA Origami with Single-Staple Resolution. *ACS Nano* (2021). doi:10.1021/acsnano.1c05540
 98. Mihai Andrei. The hexagon shape and why it shows up so much in nature. (2021). Available at: <https://www.zmescience.com/other/feature-post/hexagon-shape-nature-physics-13092021/>.
 99. Wagenbauer, K. F. *et al.* How We Make DNA Origami. *ChemBioChem* **18**, 1873–1885 (2017).
 100. Green, N. M. Avidin and streptavidin. *Methods Enzymol.* **184**, 51–67 (1990).
 101. Valimaa, L. *Streptavidin - A Versatile Binding Protein for Solid-Phase Immunoassays.* (2008).
 102. Voss, S. & Skerra, A. Mutagenesis of a flexible loop in streptavidin leads to higher affinity for the Strep-tag

- II peptide and improved performance in recombinant protein purification. *Protein Eng.* **10**, 975–982 (1997).
103. Schmidt, T. G. M., Koepke, J., Frank, R. & Skerra, A. Molecular interaction between the strep-lag affinity peptide and its cognate target, streptavidin. *J. Mol. Biol.* **255**, 753–766 (1996).
104. Korndoerfer, I.P., Skerra, A. an engineered streptavidin with improved affinity for the strep-tag II peptide : SAm1-StrepI. (2001). doi:10.2210/pdb1kl3/pdb
105. Schmidt, T. G. M. & Skerra, A. The Strep-tag system for one-step purification and high-affinity detection or capturing of proteins. *Nat. Protoc.* **2**, 1528–1535 (2007).
106. Nampally, M., Moerschbacher, B. M. & Kolkenbrock, S. Fusion of a novel genetically engineered chitosan affinity protein and green fluorescent protein for specific detection of chitosan In Vitro and In Situ. *Appl. Environ. Microbiol.* **78**, 3114–3119 (2012).
107. Freitag, S., Le Trong, I., Klumb, L., Stayton, P.S., Stenkamp, R. E. APO-CORE-STREPTAVIDIN IN COMPLEX WITH BIOTIN AT PH 4.5. (1997). doi:10.2210/pdb1swe/pdb
108. Akhtar, M. J., Ahamed, M., Alhadlaq, H. A., Alrokayan, S. A. & Kumar, S. Targeted anticancer therapy: Overexpressed receptors and nanotechnology. *Clin. Chim. Acta* **436**, 78–92 (2014).
109. Dustin, M. L. The immunological synapse. *Cancer Immunol. Res.* **2**, 1023–1033 (2014).
110. Morzy, D. K. & Bastings, M. Significance of Receptor Mobility in Multivalent Binding on Lipid Membranes. *Angew. Chemie Int. Ed.* (2022). doi:10.1002/anie.202114167
111. Alonso, M., Satoh, M. & Miyanami, K. Void-size distribution in two-dimensional random packings of equal-sized disks. *Can. J. Chem. Eng.* **70**, 28–32 (1992).
112. Välimaa, L., Pettersson, K., Rosenberg, J., Karp, M. & Lövgren, T. Quantification of streptavidin adsorption in microtitration wells. *Anal. Biochem.* **331**, 376–384 (2004).
113. Alonso, M., Satoh, M., Miyanami, K. Void size distribution in two-dimensional random packings of equal-sized disks. *Can. J. Chem. Eng.* **70**, (1992).
114. Huskens, J. *et al.* A model for describing the thermodynamics of multivalent host-guest interactions at interfaces. *J. Am. Chem. Soc.* **126**, 6784–6797 (2004).
115. Krishnamurthy, V. M., Semetey, V., Bracher, P. J., Shen, N. & Whitesides, G. M. Dependence of effective molarity on linker length for an intramolecular protein-ligand system. *J. Am. Chem. Soc.* **129**, 1312–1320 (2007).
116. Huskens, J. Multivalent interactions at interfaces. *Curr. Opin. Chem. Biol.* **10**, 537–543 (2006).

-
117. Kiessling, L. L., Gestwicki, J. E. & Strong, L. E. Synthetic multivalent ligands in the exploration of cell-surface interactions. *Curr. Opin. Chem. Biol.* **4**, 696–703 (2000).
 118. Shaw, A. *et al.* Binding to nanopatterned antigens is dominated by the spatial tolerance of antibodies. *Nat. Nanotechnol.* **14**, 184–190 (2019).
 119. Jendroszek, A. & Kjaergaard, M. Nanoscale spatial dependence of avidity in an IgG1 antibody. *Sci. Rep.* **11**, 1–10 (2021).
 120. Zhang, P. *et al.* Capturing transient antibody conformations with DNA origami epitopes. *Nat. Commun.* **11**, 1–9 (2020).
 121. Deliz-Aguirre, R. *et al.* MyD88 oligomer size functions as a physical threshold to trigger IL1R myddosome signaling. *J. Cell Biol.* **220**, (2021).
 122. Amarante-Mendes, G. P. *et al.* Pattern recognition receptors and the host cell death molecular machinery. *Front. Immunol.* **9**, 1–19 (2018).
 123. Burton, D. R. Phage display. *Immunotechnology* **1**, 87–94 (1995).
 124. Boder, E. T. & Wittrup, K. D. Combinatorial Polypeptide Libraries. *Nat. Biotechnol.* **15**, 553–557 (1997).
 125. Cull, M. G., Miller, J. F. & Schatz, P. J. Screening for receptor ligands using large libraries of peptides linked to the C terminus of the lac repressor. *Proc. Natl. Acad. Sci. U. S. A.* **89**, 1865–1869 (1992).
 126. Hanes, J. & Plückthun, A. In vitro selection and evolution of functional proteins by using ribosome display. *Proc. Natl. Acad. Sci. U. S. A.* **94**, 4937–4942 (1997).
 127. Weber, P. C., Pantoliano, M. W. & Thompson, L. D. Crystal Structure and Ligand-Binding Studies of a Screened Peptide Complexed with Streptavidin. *Biochemistry* **31**, 9350–9354 (1992).
 128. Giebel, L. B. *et al.* Screening of Cyclic Peptide Phage Libraries Identifies Ligands That Bind Streptavidin with High Affinities. *Biochemistry* **34**, 15430–15435 (1995).
 129. Lamla, T. & Erdmann, V. A. The Nano-tag, a streptavidin-binding peptide for the purification and detection of recombinant proteins. *Protein Expr. Purif.* **33**, 39–47 (2004).
 130. Lamla, T. & Erdmann, V. A. Searching sequence space for high-affinity binding peptides using ribosome display. *J. Mol. Biol.* **329**, 381–388 (2003).
 131. Schmidt, T. G. M. & Skerra, A. The random peptide library-assisted engineering of a c-terminal affinity peptide, useful for the detection and purification of a functional ig Fv fragment. *Protein Eng. Des. Sel.* **6**, 109–122 (1993).
 132. Bastings, M. M. C. *et al.* From phage display to dendrimer display: Insights into multivalent binding. *J. Am.*

- Chem. Soc.* **133**, 6636–6641 (2011).
133. Keefe, A. D., Wilson, D. S., Seelig, B. & Szostak, J. W. One-step purification of recombinant proteins using a nanomolar-affinity streptavidin-binding peptide, the SBP-tag. *Protein Expr. Purif.* **23**, 440–446 (2001).
134. Roberts, D., Guegler, K. & Winter, J. Antibody as a surrogate receptor in the screening of a phage display library. *Gene* **128**, 67–69 (1993).
135. Caparon, M. H., De Ciechi, P. A., Devine, C. S., Olins, P. O. & Lee, S. C. Analysis of novel streptavidin-binding peptides, identified using a phage display library, shows that amino acids external to a perfectly conserved consensus sequence and to the presented peptides contribute to binding. *Mol. Divers.* **1**, 241–246 (1996).
136. Lyamichev, V. I. *et al.* Stepwise Evolution Improves Identification of Diverse Peptides Binding to a Protein Target. *Sci. Rep.* **7**, 12116 (2017).
137. Yi-PinChangYen-HoChu. Using surface plasmon resonance to directly determine binding affinities of combinatorially selected cyclopeptides and their linear analogs to a streptavidin chip. *Anal. Biochem.* **340**, 74–79 (2005).
138. Oesterlin, C. Solid Phase Peptide Synthesis . I . Tetrapeptide1. (1963).
139. Guo, X. Surface plasmon resonance based biosensor technique: A review. *J. Biophotonics* **5**, 483–501 (2012).
140. Ritzefeld, M. & Sewald, N. Real-Time Analysis of Specific Protein-DNA Interactions with Surface Plasmon Resonance. *J. Amino Acids* **2012**, 1–19 (2012).
141. Farhana, M. A. A. Enzyme Linked Immunosorbent Assay. (2021).
142. Yun, S., Lee, S., Park, J. P., Choo, J. & Lee, E. K. Modification of phage display technique for improved screening of high-affinity binding peptides. *J. Biotechnol.* **289**, 88–92 (2019).
143. Du, T., Zhu, G., Wu, X., Fang, J. & Zhou, E. M. Biotinylated single-domain antibody-based blocking ELISA for detection of antibodies against swine influenza virus. *Int. J. Nanomedicine* **14**, 9337–9349 (2019).
144. Kimoto, M., Sherman Lim, Y. W. & Hirao, I. Molecular affinity rulers: systematic evaluation of DNA aptamers for their applicabilities in ELISA. *Nucleic Acids Res.* **47**, 8362–8374 (2019).
145. Chloe Barnett. ELISA Applications. (2019). Available at: <https://www.news-medical.net/life-sciences/ELISA-Applications.aspx>. (Accessed: 5th August 2021)
146. Agius, R. & Nadulski, T. Utility of ELISA screening for the monitoring of abstinence from illegal and legal drugs in hair and urine. *Drug Test. Anal.* **6**, 101–109 (2014).
147. IBA Lifesciences GmbH. Strep-Tactin® and Strep-Tactin®XT purification cycle. (2021). Available at: <https://www.iba-lifesciences.com/strep-tag/protein-purification/>.

148. Kitov, P. I. & Bundle, D. R. On the Nature of the Multivalency Effect: A Thermodynamic Model. *J. Am. Chem. Soc.* **125**, 16271–16284 (2003).
149. Da Huang, M. F. & M. P. DNA-Mediated Patterning of Single Quantum Dot Nanoarrays: A Reusable Platform for Single- Molecule Control. *Sci. Rep.* (2017). doi:10.1038/srep45591

Curriculum Vitae

Hale Bila

Chemin des Jonchets 10, 1030 Bussigny, Switzerland

Tel: +41 78 724 85 39

halebila89@gmail.com

Education

- PhD in Materials Science and Engineering, Ecole Polytechnique Fédérale de Lausanne, Lausanne, Switzerland (01/2017-03/2022)
- MSc in Chemistry, Bilkent University, Ankara, Turkey (02/2013-08/2015)
- MSc & BSc in Chemistry Education, Middle East Technical University, Ankara, Turkey (09/2007- 02/2013)

Research Experience

- PhD Thesis : Designed and developed fully programmable DNA-based super-selective multivalent nanoparticles platform that can interact with spatially well-defined targets.
Supervisor : Prof. Maartje M. C. Bastings
- Research Intern : Synthesized and investigated the thermo-mechanical properties of oligopeptide modified polymers (Collaboration with The Michelin Group)
Supervisor : Prof. Holger Frauenrath
- Master Thesis : A homogeneous system for photogeneration of hydrogen initiated by BODIPY based photoinduced electron transfer
Supervisor : Prof. Engin U. Akkaya

Teaching Experience

- Doctoral Assistant : Oversaw 6 master students on the modelling and application of DNA-based multivalent nanoparticles
- Teaching Assistant : Biomaterials class (Fall 2017 and Spring 2018)
- Teaching Assistant : Scientific literature in bioengineering self enrolment (2017-2018)
- Teaching Assistant : General chemistry (2013-2015)
-

Conferences and Presentations

- Materials Research Society, MRS, Spring Meeting, (04/2019), Phoenix, AZ, USA. Oral Presentation

- Golden Research Conference, GRC, Self-Assembly and Supramolecular Chemistry, (05/2019), Les Diablerets, Switzerland. Poster Presentation
- Shaping the Future of Bioengineering, SFBE, (09/2017), Davos, Switzerland. Poster Presentation
- 1st International Caparica Conference on Chromogenic and Emissive Materials, IC3EM, (09/2014), Caparica, Portugal. Poster Presentation

○

Honor Awards

- Full Scholarship for Master Studies (2013-2015), Bilkent University
- Ranking first at the Department of Chemistry Education, 2013
- Gold Medal in Taekwondo Tournament, Middle East Technical University

○

Extracurricular Activities

- METU Taekwondo Team, Ankara, Turkey, *Team Leader*, (01/2008-06/2015)
- Hard Rock Cafe, Washington D.C., USA, *Retail Sales Associate*, (06/2011-09/2011)
- 1907 UNIFEB-METU, Ankara, Turkey, *Product Manager*, (09/2008-06/2009)

○

Certificates

- KOSGEB, Entrepreneurship Training (05/2015)
- Project Management, Udemy (06/2020)
- 1st Dan World Taekwondo Federation

○

Publications

- **Bila, H.**, Kurisinkal E., E., Bastings, M. Engineering a stable future for DNA-origami as a biomaterial. *Biomater. Sci.*, 2019, 7, 532-541.
- **Bila, H.**, Paloja, K., Caroprese, V., Kononenko, A., Bastings, M. Multivalent Pattern Recognition Through Engineering Spatial Tolerance in DNA-Based Nanomaterials. *Manuscript in Preparation*.

○

Instrument Knowledge

HPLC, MS, NMR, SPR, TGA, UV-VIS, FT-IR, Plate Reader, DLS

Software Knowledge

Mestrenova, OriginLab, GraphPad Prism, ChemDraw, PyMol, MS Office Applications

Languages

Turkish (native), English (fluent), German (intermediate), French (basic)

Interests

Traveling, reading, taekwondo, zumba, fitness, painting